Electrochemical studies of MBE-grown CaF_2/BaF_2 heterolayers

Von der Fakultät Chemie der Universität Stuttgart
zur Erlangung der Würde eines
Doktors der Naturwissenschaften (Dr. rer. nat.)
genehmigte Abhandlung

Vorgelegt von

Ion Matei

aus Domneşti/Rumänien

Hauptberichter:	**Prof. Dr. J. Maier**
Mitberichter:	**Prof. Dr. F. Aldinger**
Tag der Einreichung:	**16.05.2007**
Tag der mündlichen Prüfung:	**25.07.2007**

Max-Planck-Institut für Festköperforschung

Stuttgart

2007

Contents

Zusammenfassung

Ionenleiter, d.h. Materialien, in denen spezifische Ionen eine möglichst hohe Beweglichkeit aufweisen, sind wichtig für elektrochemische Messungen sowie für Bauteile wie Hochtemperaturbatterien und -Brennstoffzellen, chemische Filter und Sensoren. Die ionische Leitfähigkeit in Festelektrolyten kann durch das Einbringen geeigneter Verunreinigungen in die Struktur, aber auch durch Grenzflächen, die zu einer Umverteilung der Ionen in Raumladungszonen führen, verbesssert werden.

Den Schwerpunkt dieser Untersuchung bildet die Dynamik von mittels Molekularstrahlepitaxie hergestellten ionenleitenden Übergittern, in denen die Grenzflächen künstlich verändert sind. Das Ziel ist die Schaffung verbesserter Ionenleiter durch Kontrolle dieser Grenzflächen. In kristallinen Ionenleitern wandern die Ionen über Gitterplätze oder Zwischengitterplätze. Daher kann die Ionendynamik auch von der Kristallstruktur beeinflußt werden. Da die Übergitter es zu einem gewissen Grad auch erlauben, die Kristallstruktur zu modifizieren, wird auch die Abhängigkeit der Ionenleitfähigkeit von strukturellen Parametern in dieser Arbeit untersucht. Es ist zu erwarten, dass die Grenzflächen Gitterspannungen aufgrund von Gitter-Fehlpassung verusachen, und/oder die Ladungsverteilung in der Raumladungszone verändern, wenn Übergitter aus Ionenleitern mit einer Periodizität von einigen hundert Nanometern hergestellt werden. Da die beweglichen Ionen unter Brechung der Bindungen zu den Gitterionen wandern, wird die Ionendynamik durch Änderungen in der Raumladungsverteilung an den Grenzflächen sowie durch ionische Effekte ernsthaft beeinflußt.

"Heterojunctions" in zweiphasigen Systemen können für die Verbessung der Ionenleitfähigkeit besonders effizient sein. Ein qualitativ verändertes Leitfähigkeitsverhalten ist zu erwarten, wenn der Grenzflächen-Abstand vergleichbar oder kleiner als die Ausdehnung der Raumladungszone in vergleichbar großen Kristallen ist [1987Ma1],[2000Ma]. Vor kurzem wurde eine erhöhte Ionenleitfähigkeit parallel zu den Grenzflächen in ebenen CaF_2/BaF_2-Heterostrukturen entdeckt, die auftritt, wenn die individuelle Schichtdicke unter 50 nm liegt. Bei diesen Dicken verlieren die Einzelschichten ihre Individualität und ein künstliches ionenleitendes Material mit anomalen Transporteingenschaften wird erzeugt. Diese Ergebnisse demonstrieren mesoskopische Ionenleitungseffekte in Nanosystemen (extrem dünne Filme, nanokristalline Materialien) [2000Sata].

Die Morphologie und Defektstruktur von CaF_2/BaF_2-Multischichten wurden systematisch mit verschiedenen elektronenmikroskopischen Techniken einschließlich AFM und QHRTEM untersucht [2002Sata]. Die Schichtstruktur und die Bildung ausgedehnter Kristalldefekte haben einen starken Einfluß auf die Dichte und Beweglichkeit der Ladungsträger in den Mehrfachschichten, der zu den rein chemischen Effekten hinzukommt.

Für ein tiefergehendes grundlegendes Verständnis der Leitfähigkeitseffekte müssen einige Punkte noch geklärt werden und werden in diese Arbeit behandelt: (1) ein detailliertes Verständnis der defektchemischen Situation und der Leitfähigkeitseffekte parallel und senkrecht zu den Grenzflächen, (2) Effekte der thermischen Behandlung, (3) theoretische Beschreibung und numerische Auswertung im Bereich der mesoskopischen Regimes (dünner als 50 nm). Um diese Effekte tiefgreifend zu verstehen, werden elektrische Messungen in paralleler (entlang der Grenzflächen) und senkrechter (relativ zu den Grenzflächen) Konfiguration der Heterostrukturen durchgeführt sowie thermodynamische Modellierungen angestellt.

Außerdem wurde die ionische Leitfähigkeit von CaF_2 und BaF_2 (beide mit Fluorit-Typ) bestimmt und aus der Anpassung der effektive Gehalt von Verunreinigungen berechnet.

Für die strukturelle Untersuchung der Grenzflächen und der Morphologie der einzelnen Schichten wurden Doppleschichten mit verschiedener Dicke von CaF_2 auf einer BaF_2-Schicht konstanter Dicke durch Molekularstrahlepitaxie hergestellt. Die Untersuchung der Gesamtleitfähigkeit als Funktion der Dicke erlaubt die Auftrennung in Volumenleitfähigkeit von CaF_2 und Grenzflächeneffekte zwischen CaF_2 und BaF_2.

CaF_2/BaF_2 Multischichten wurden mit Molekularstrahlepitaxie (MBE) auf unterschiedlichen Substraten (Al_2O_3, Si, Nb-dotiertes $SrTiO_3$) mit genau definierter Geometrie, Periodizität, Grenzflächenabstand und Schichtreihenfolge hergestellt.

Die Orientierung und die Oberflächenmorphologie der Proben wurden mit XRD und AFM untersucht. Die Filme auf verschiedenen Substraten weisen die selbe Gesamtdicke von etwa 400 nm auf, und die individuelle nominelle Schichtdicke wurde in einem weiten Bereich von 6.5÷200 nm durch computergestreuerte Verschlüsse der Effusionszellen variiert. Die Gesamtleitfähigkeit wurde mit Impedanzspektroskopie im Temperaturbereich von 610-650°C und Frequenzbereich von 10^{-1} bis 10^{7} Hz gemessen. Ein typisches Impedanzspektrum einer CaF_2/BaF_2-Heterostruktur auf (1102) Al_2O_3 zeigt einen wohldefinierten Halbkreis, was auf rein ionische Leitfähigkeit hinweist.

XRD-Messungen zeigen gut definierte epitaktische Heteroschichten mit [111]-Orientierung. Diese Orientierung hängt von der ersten auf dem Substrat abgeschiedenen Schicht ab: die erste Schicht auf (1102)-orientiertem Al_2O_3 war immer BaF_2. Typische AFM-Bilder der Oberfläche von CaF_2 auf (111)-orientierten CaF_2/BaF_2 Heterostrukturen auf einem (1102)-Al_2O_3-Substrat weisen in zwei Dimensionen eine dreieckige Oberflächentopographie auf, die mit der in Polfigurmessungen beobachteten Verzwilligung zusammenhängen können. Alle Bilder zeigen einen dichten Film und sehr glatte Oberflächen mit einer Rauigkeit um 4 nm.

Die gemessene effektive parallele Leitfähigkeit (d.h. aus einer Messung der parallelen Leitfähigkeit und der Gesamtdicke von ~ 400 nm berechnet) steigt erheblich mit der Grenzflächendichte an. Zwei Gründe dafür erscheinen plausibel:

— thermodynamische Umverteilung von F^--Ionen von einer Phase in die andere, entsprechend den verschiedenen Energieniveaus in den beiden Phasen. Das führt zu einem Anstieg der Fluorid-Leerstellenkonzentration im einen und einer Zunahme der Fluorid-Zwischengitterteilchen im anderen Ionenleiter.

— ein- oder beidseitiger Transfer von F^- zu oder vom Kern der Grenzfläche, um dessen Freie Energie anzusenken.

Das Ziel der Experimente zur thermischen Behandlung ist, den anomalen Anstieg des Probenwiderstands (bzw. Abfall der parallelen Leitfähigkeit) zu bestimmen, der mit steigender Temperatur auftritt. Die Verschlechterung der Leitfähigkeit findet beim ersten Aufheizen zwischen 300°C und 500°C statt. Die Leitfähigkeit wird als Funktion von Temperatur und Grenzflächenabstand untersucht, und konnte als Ionenleitfähigkeit (wie im Volumen) identifiziert werden.

Die experimentellen Daten zeigen folgende Effekte des Temperns bei niedrigen Temperaturen:

— erhöhte parallele Leitfähigkeit (um mehr als eine Größenordnung)

— verringerte Aktivierungsenergie, Ea (abgesenkt auf 0.5 eV)

— wohl definierte Veränderung mit der Grenzflächen-Dichte

Das kann mit der Existenz von instabilen Versetzungen, nicht nur an der Grenzfläche, sondern auch innerhalb der Schichten, in Verbindung gebracht werden, die durch Temperaturbehandlung ausgeheilt werden können. Daraus ergibt sich ein klares Bild: in ausgelagerten Proben werden Fluorid-Ionen F^- von einer Phase in die andere umverteilt. Das führt zu einer erhöhten Fluorid-Leerstellenkonzentration in der einen und einer erhöhten Zwischengitterteilchenkonzentration in der anderen Phase. In nicht ausgelagerten Proben oder Tempern bei niedrigen Temperaturen wird dies durch eine Aufladung von Versetzungen überlagert, die Leerstellen in der Umgebung zurücklassen.

Heterostrukturen auf leitfähigen Substraten (Si, Nb-dotiertes $SrTiO_3$) wurden ebenfalls mit definierter Orientierung als glatte und dichte Filme präpariert. CaF_2/BaF_2 Heteroschichten wurden epitaktisch auf leitfähigen einkristallinen STO:Nb Substraten hergestellt, was Leitfähigkeitsmessungen senkrecht zu den Grenzflächen erlaubt. Mesoskopische Größeneffekte sagen eine Verringerung des Unterschieds zwischen paralleler und senkrechter Leitfähigkeit mit zunehmender Zahl der Grenzflächen voraus. Die senkrechte Leitfähigkeit frisch hergestellter Proben ist um Größenordnugnen höher als der aus Einkristalldaten erwartete Wert.

Interessanterweise beschreiben die selben Konzentrationsprofile, die die parallelen Leitfähigkeiten erklären, auch die Effekte in der senkrechten Leitfähigkeit. Das ist nicht selbstverständlich, da die parallele Leitfähigkeit durch die hochleitfähigen Bereiche bestimmt wird, während die senkrechte Leitfähigkeit die schlechtleitenden Bereiche widerspiegelt.

In dieser Untersuchung wird die Dickenabhängigkeit der Schichtleitfähigkeit numerisch sowohl nach dem Gouy-Chapman- als auch nach dem Mott-Schottky-Modell berechnet. Im direkten Vergleich zu den Meßdaten zeigt sich, daß nur das Mott-Schottky-Modell alle Befunde der Messungen wiedergeben kann, wie vor allem das anomale Verhalten im mesoskopischen Regime (effektive Leifähigkeit vs. inverse Dicke). Die berechneten Konzentrationsprofile sind jedoch nur dann konsistent mit der Ladungsdichte im Mott-Schottky-Modell, wenn das eingefrorene Profil der Verunreinigungen an den Grenzflächen leicht erhöht wird.

Eine solche Verteilung wird realistischerweise erwartet wenn man die Probenpräparation wie auch die Vorbehandlung vor den Messungen (Auslagern bei erhöhter Temperatur) in Betracht zieht.

Zusammengefaßt kann man sagen:

1. CaF_2/BaF_2-Heteroschichten wurden mit Molekularstrahlepitaxie (MBE) auf verschiedenen Substraten (Al_2O_3, Nb-dotiertes $SrTiO_3$) mit genau definierter Geometrie, Periodizität, Grenzflächenabstand und Schichtreihenfolge hergestellt.
2. XRD- und AFM-Messungen zeigen, daß definierte, hochgradig oriertierte CaF_2/BaF_2-Heterostrukturen auf verschiedenen Substraten hergestellt werden können.
3. Die Leitfähigkeitseffekte können als ionische Raumladungseffekte in Folge der thermodynamisch bestimmten F^--Umverteilung im Gleichgewicht verstanden werden.

4. Der Einfluß der thermischen Auslagerung auf der Widerstand der Probe wurde untersucht. Instabile Versetzungen scheinen durch F^--Adsorption elektrisch aufgeladen zu sein.

5. In dieser Untersuchung wird die Dickenabhängigkeit der Schicht-Leitfähigkeit numerisch nach dem Gouy-Chapman- und dem Mott-Schottky-Modell berechnet. Im direkten Vergleich mit den Meßdaten kann das modifizierte Mott-Schottky-Modell (Verunreinigungsprofil mit einem Ansteig nahe der Grenzfläche) die Befunde der Messungen sogar im mesoskopischen Regime wiedergeben.

Abstract

Ionic conductors, materials in which specific ions can migrate preferentially with high mobility, are of prime importance for electrochemical measurements, and for devices such as high-temperature batteries and fuel cells, chemical filters and sensors. Ionic conductivity in solid electrolytes can be improved by dissolving appropriate impurities into the structure but also by introducing interfaces that cause the redistribution of ions in the space-charge regions.

This research study is focused on the dynamics of ion-conducting superlattices synthesized by molecular beam epitaxy (MBE) in which the interfaces are artificially tuned, with the aim of designing superior ionic conductors by controlling their interfaces. In the crystalline ionic conductors, the ions migrate around lattice sites/interstitial sites in the crystals. Consequently, the ion dynamics can be affected by the crystal structure as well. Since the superlattice structure enables to tune the crystal structure to some extent, the ionic conductivity dependence on the structural parameters will also be investigated in this study. The interface is also expected to introduce lattice strain due to lattice mismatches and/or to change space charge distribution at the interfaces when superlattices of different ionic conductors are fabricated with a period of a few to a few hundred nanometres. Mobile ions migrate by breaking the bonds with the lattice ions, and therefore, the ion dynamics are seriously affected by the change in the space charge distribution at the interfaces as well as by ionic effects.

Heterojunctions in two-phase systems can be particularly efficient at improving ionic conduction. A qualitatively different conductivity behaviour is expected when the interface spacing is comparable to or smaller than the width of the space charge regions in comparatively large crystals [1987Ma1],[2000Ma]. Recently, increases in ionic conductivity parallel to the interfaces of CaF_2/BaF_2 planar heterostructures have been discovered when the individual layer thickness is less than 50nm. At such thickness, single layers lose their individuality and an artificial ionically conducting material with anomalous transport properties is generated. These results demonstrate mesoscopic ion conductivity effect in nanosystems (extremely thin films, nanocrystalline materials) [2000Sata].

The morphology and the defect structures of CaF_2/BaF_2 multilayers have been studied systematically with various electron microscopy techniques, including AFM and QHRTEM [2002Sata]. The

layer structure and the formation of extended crystal defects have strong influences on the density and the mobility of charge carriers in the multilayers that add to the purely chemical effects.

In order to obtain more fundamental insight into the conductivity effects, some points still need to be clarified and are addressed in this study: (1) the detailed understanding of the defect chemical situation and the conductivity effects in parallel and in perpendicular direction to the interfaces; (2) the annealing effects; (3) theoretical model and numerical evaluation in periods of the mesoscopic situation (thinner than 50nm). To understand these effects in depth, electrical measurements on parallel (along the interfaces) and perpendicular (to the interfaces) configuration of the heterostructures as well as thermodynamic modelling are performed.

Also, the ionic conductivity of fluorite-type crystals CaF_2 and BaF_2 was determined and from fitting the effective level of impurities has been calculated.

For the structural investigation of the interfacial and individual layer morphologies, bilayer samples with various thicknesses of CaF_2 on top of constant layer of BaF_2, were prepared by molecular beam epitaxy technique. The investigation of the overall conductance as a function of the thickness permits the deconvolution of bulk conductivity of CaF_2 and interface effects between CaF_2 and BaF_2.

Multilayers of CaF_2/BaF_2 have been prepared by molecular beam epitaxy (MBE) on different substrates (Al_2O_3, Si, Nb-doped $SrTiO_3$), with highly defined geometry, periodicity, interfacial spacings and layer sequence.

The orientation and the surface morphology of the samples have been investigated by XRD and AFM. The films grown on different substrates exhibit the same total thickness of about 400 nm, and the individual nominal layer thickness was varied in a wide range of 6.5-200nm by computer-controlled effusion cell shutters. The overall conductivity was measured by a.c. impedance spectroscopy in the temperature range of 610–50°C, with frequencies ranging from 10^{-1} to 10^{7} Hz. A typical impedance spectrum for the CaF_2/BaF_2 heterostructure grown on Al_2O_3 (1102) shows a well defined semicircle, indicating that the conduction is only ionically.

XRD measurements show well defined epitaxial heterolayers with [111] orientations. This orientation depends on the first layer deposited on the substrate: the first layer on top of (1102) oriented Al_2O_3 was always BaF_2. Typical AFM images for the surfaces of CaF_2 on the top of (111) oriented CaF_2/BaF_2 heterostructures on an Al_2O_3 (1102) substrate show a triangular surface topography in two

directions, which may refer to a twinning as observed by pole figure measurements. All images show a dense film and very smooth surfaces with roughness around 4nm.

The measured effective parallel conductivity (*i.e.* derived from the measurement of parallel conductance via the total thickness ~400nm) progressively increases with interfacial density. Two reasons for the conductivity effects appear plausible:

- Thermodynamically redistribution of F^--ions from one phase to the other according to the different energy levels in the two phases. This leads to an increase of the fluoride vacancy concentration in one conductor and of the fluoride interstitial in the other conductor.
- Unilateral or bilateral F^- transfer to or from the interface core layer in order to lower the interfacial core free energy.

The purpose of the annealing experiment is to determine the anomalous increase in the resistance of the sample (or decrease of the parallel conductivity of the sample) as the annealing temperature increases. Conductivity degradation occurs between 300°C and 500°C during the first heating. The conductivity is studied as a function of temperature and interfacial spacing and has been verified to be ionic (as in the bulk).

The experimental data shows that the low temperature treatment leads to:

- Higher parallel conductivity (more than one order of magnitude);
- Lower activation energy, E_a (down to 0.5 eV);
- Well-behaved interfacial density dependence.

This can be associated with the existence of unstable dislocations not only at the interface, but also inside the layers that can be annealed out by thermal treatment. This results in a clear picture: in annealed samples there is a fluorite (F^--ions) transfer from one phase to the other. This leads to an increase of fluoride vacancy concentration in one phase and of the fluoride interstitial in the other. In a non-annealed samples this is superimposed by charging of dislocations leaving vacancies in the vicinity.

The heterostructures on conductive substrates (Si, Nb-doped $SrTiO_3$) were also prepared with well defined orientation, smooth and dense film. CaF_2/BaF_2 heterolayers have been epitaxially grown on the conductive single-crystal STO:Nb substrates, which enables us to carry out the conductivity measurement in the perpendicular direction to the interfaces. Mesoscopic size effects predict a decrease in the difference between parallel and perpendicular conductivity with the increase in the number of interfaces. As-prepared specimens exhibit

perpendicular conductivities higher by orders of magnitude than the expected value from single crystal.

Interesting the same profiles that explain the parallel conductivities are also able to explain the perpendicular effects. This is very satisfactory as a parallel conductivity pronounces the highly conductive regions, while the perpendicular one emphasizes the less conductive regions.

In this study, the thickness dependence of the layer conductivities is numerically calculated using both the Gouy-Chapman and the Mott-Schottky modes. In direct comparison to the experimental data, we find that only the Mott-Schottky model can reproduce all the features of the experiments, like the anomalous behaviour (effective conductivity versus inverse thickness) in the mesoscopic range. However, the calculated concentration profile turns only out to be consistent with the charge density of the Mott-Schottky model if the frozen-in impurity profile is assumed to be moderately increased.

Such a distribution is realistically expected in view of the sample preparation as well as of the conditioning prior to the measurements (annealing at elevated temperatures).

In summary:

1. Heterolayers of CaF_2/BaF_2 have been prepared by molecular beam epitaxy (MBE) on different substrates (Al_2O_3, Nb-doped $SrTiO_3$), with highly defined geometry, periodicity, interfacial spacings and layer sequence.
2. X-ray and AFM measurements demonstrate that defined highly oriented heterostructures of CaF_2/BaF_2... can be prepared on different substrates.
3. The conductivity effects can be understood in terms of ionic space charge effects occurring as a consequence of a thermodynamic F^- redistribution at equilibrium.
4. The influence of annealing effects on the resistance of the sample has been studied and analysed. Unstable dislocations appear to be charged by F^- adsorption.
5. In this study, the thickness dependence of the layer conductivities is numerically calculated using both the Gouy-Chapman, and the Mott-Schottky models. In direct comparison to the experimental data, the modified Mott-Schottky mode (impurity profile with a gradient close to the interface) can reproduce the features of the experiments even in the mesoscopic range.

Introduction and Motivation

Thin film structures and self-assembled nano-particles supported on various substrates became in recent years of fundamental importance in so far as these have dimensions low enough to reveal unusual physical properties with respect to those of the bulk. Electronic devices, solid-states batteries, gas sensors, heterogeneous catalysis and other numerous technologies are strongly dependent on the quality of thin films, many of them of nano-sized thickness.

Electrical properties of interfaces in materials with mobile ionic or charge carriers (defects) differ from the bulk properties. In equilibrium, the mobile charge carriers therefore distribute themselves between the bulk and the interface region, such that the total free energy is minimized. The extent of redistribution depends on the chemical driving force to absorb charge carriers in the interface, while the thickness of the space charge region depends on the density of mobile charge carriers in the material and may extend from one atomic spacing up to the several mm and more.

Electrical properties of the interface are, in general, highly anisotropic. For this reason we describe the properties of the interfaces separately in a direction parallel and perpendicular to the interface. Considering the materials, in which one type of charge carriers already contributes decisively to overall conductance, there exist space charge regions with an accumulation or depletion of majority charge carriers. In case of the accumulation, the enhanced conductivity is particularly perceptible parallel to the interface, while in the depletion case the increased resistivity is measurable perpendicular to the interface. Both parallel and perpendicular interfacial effects have been investigated, mainly in the field of semiconductors [1981Sze].

The properties of interfaces in solid ionic conductor are, in contrast to interfaces in semiconductors and liquid electrolytes, still poorly characterized. The studies of the interfaces in material science community were inspired by the potential use of solid ionic conductors as electrolytes in batteries with a high energy density. Due to the high density of interfaces, space charge effects are especially pronounced in ceramic and composite materials, or in the epitaxially grown films with were well defined interfaces and geometry.

The purpose of this work was to obtain more fundamental insight into ionic processes in CaF_2/BaF_2 heterolayers:

1. the understanding of the mesoscopic situation (i.e. for film thicknesses thinner than 50 nm, both in parallel and in perpendicular direction to the interfaces);
2. the structural investigation of the interfacial and individual layer morphologies;
3. to understand annealing effects, in particular, the anomalous increase in the resistance of the sample (or decrease of the parallel conductivity of the sample) as the annealing temperature increase.
4. to find a theoretical model which can explain the behaviour of the total conductivity of the heterolayers.

The thesis is structured as follows:

In Chapter 1 is presented the literature background of the experiments carried out for the single crystals CaF_2 and BaF_2, for the heterostructures CaF_2/BaF_2 and for the deposition of CaF_2 on the Si conductive substrate.

Chapter 2 comprises the general defect chemical theory of space charge region involving interfaces, and, in particular, application of the theory for CaF_2/BaF_2 interfaces.

In Chapter 3 the physical and electrical properties of CaF_2 and BaF_2 are summarized, and the basic defect structures in the intrinsic and extrinsic regions shortly outlined.

In Chapter 4 the basics of growth processes (thermodynamic and kinetic aspects), as well as experimental setups (MBE machine and electrical setup for parallel and perpendicular measurements) are described. The experimental devices consist in the technique used for preparation of the heterostructures, the physical measurement description, and the electrical measurement setup.

Chapter 5 presents the experimental results obtained for:

1. single crystal measurements of CaF_2 and BaF_2;
2. thickness and temperature dependence of the conductivity of the samples with various thicknesses of CaF_2 on top of a constant layer of BaF_2: calculation of the contribution of the interface between CaF_2/BaF_2 and of the bulk conductivity of the CaF_2;
3. annealing effects: the anomalous increase in the resistance of the sample as the annealing temperature increase;
4. perpendicular measurements on the samples grown on Si or Nb-doped substrates as complementary results to the study of lateral effects.

Chapter 6 deals with the thickness dependence of the layer conductivities numerically calculated using both the Gouy-Chapman, and the Mott-Schottky modes. As well a new model is proposed to explain the anomalous steep increase of conductivity, and the abrupt transition between semi-infinite space charge to mesoscopic situation.

The thesis ends with a summary in which the most important results are compiled.

Chapter 1

Literature Survey (Background) on CaF_2 and BaF_2 Ion Conductors

By the time, a large number of experimental and theoretical studies of the defect properties of crystals with the fluorite-related structure have been carried out. The major characteristic of most fluorides is a large energy gap, hence a low electronic conductivity with high activation energy, and hence an empty conduction band, due to the strong electronegativity of fluorine. Since the 1950s research on fluorine ion conductors has developed to a great extent, partially because of industrial application, but also as a result of the existence of many fluorite-type materials that are electronic insulators.

In the earlier investigations of the CaF_2 crystals, from electrical measurements the conductivity was found to be ionic, with the major disorder being of anti-Frenkel type, i.e. characterized by F^- vacancies ($V_F^{\bullet}$) and interstitials ($F_i^{'}$) [1957Ure],[1973Boll1]. Similarly results have been found also for BaF_2 crystals [1968Bars1,[1968Bars2,[1973Boll2]. These authors calculated the number of anti-Frenkel defects in the pure crystal, the mobilities of the interstitials and vacancies. The electronic conductivity was also studied by a number of researchers. Using a polarization technique developed by Wagner [1956Wag],[1957Wag] and measurements of the total electrical conductivity as a function of the partial pressure of fluorine [1973Hin] they have concluded that CaF_2 exhibits negligible electronic conductivity [1978Del]. The measurements of electronic conductivity of single crystal BaF_2 were done by polarization method, and showed that the electronic conductivity is at least two orders of magnitude lower that the ionic conductivity for temperature lower that 800°C [1979Red].

In recent years, nanometer-scale ion conductors have attracted increasing interest [1995Ma1],[2000Tuller]. Ionic conductivity properties may be tuned by introducing interfaces into ionically conducting system, which leads to an altered defect chemistry in the space-charge regions [1995Ma1],[1984Ma],[1987Ma1],[1995Saito],[1987Ma2],[1985Ma],[2002Sata],[1999Jam]. The importance of space charge regions and charged non-stoichiometries in ionic conductors which interact with neighbouring phases has been analyzed in three types of heterogeneous systems: (i) an ionic conductor/surface active insulator system [1985Ma2], (ii) a two ionic conductor system [1985Ma1], (iii) a polycrystalline, ionically conducting materials system [1986Ma]. In all these cases the ions are redistributed at boundary regions such that the electrochemical potential gradient of the defects vanishes.

In Ref. [1996Wil] theoretical simulations of the superionic conductor CaF_2 have been undertaken, with a model for the interionic interactions derived directly from electronic structure calculations. The model includes such many-body effects as polarization and the adaptation of the size of the anion to its instantaneous environment (compression). Physical properties of CaF_2 that are accurately reproduced include phonon frequencies, and solid-state diffusion. Analysis shows that the compression effect is much less important for fluorides than oxides. Polarization effects, particularly of the *cations*, play a crucial role in allowing for anion diffusion, and the importance of a short-range contribution to the cation polarization is highlighted. In Ref [1993Lin] similar simulation studies have been carried out. The results reproduce the observed mobility data and the heat capacity anomaly associated with the onset of ionic conduction. By examining the ionic configurations in detail, it has been shown that the ionic conduction involved the formation of Frenkel pairs on the anion sub-lattice and the migration of the interstitial ion.

Recently, artificial ion conductors have been prepared for the first time by growing epitaxial heterolayers consisting of BaF_2–CaF_2 using molecular beam epitaxy (MBE), and have shown a significant dependence of the conductivity (effective ionic conductivity parallel to the interface) on the layer thickness [2000Sata]. The proposed defect inducing mechanism is a transfer of F^- from BaF_2 to CaF_2 leading to an increased vacancy concentration in BaF_2 dominating the low temperature conductance and to an increased interstitial concentration in CaF_2 probably dominating the conductance at high temperatures. Progressively enhanced ionic conductivities and anomalous transport properties were observed as the periods of heterolayers varied from 430 to 16.2 nm. Semi-infinite space charge calculations, assuming a redistribution of fluoride ions at the interfaces, can quantitatively explain the results for comparatively large spacings (>50 nm).

The investigations of pure BaF_2 single-layer films grown on sapphire substrates were also carried out in order not only to investigate the defect chemical and interfacial properties of BaF_2 films but also to understand the space charge contribution of substrate interface in the heterostructures. Space charge effects in CaF_2 and PbF_2 due to the contact to oxide phases (e.g. SiO_2) have been observed in two-phase mixtures and attributed to the adsorption of F^- to the surface of the oxide [2004Guo1]. It was found that the semi-infinite space-charge regions seem to be responsible for the increased conductivity of the films induced by interaction with the substrate. Debye lengths have been estimated from the analysis of defect chemistry of the bulk contribution and found to be consistent with semi-infinite conditions assumed here, and also with previous measurements on heterostructures from Ref. [2000Sata]. At low temperatures, an additional conductance increase is observed and ascribed to strain effects.

In order to obtain more fundamental insight into ionic contact processes, in Ref [2004Guo2] the contribution of electronic carriers has been investigated, as well as the effects of substrate and orientation on the conductivity of heterostructure. For this reason, heterostructures have been prepared with various substrates and different orientations. It was found the ionic conductivity is at least one order of magnitude larger than the electronic contribution which is not a surprising result in view of the redox stability of the ionic compound and the redox potential of the ambient (Ar atmosphere). These results are in a good agreement with previous investigations which have shown that the ionic conductivity is about one order of magnitude larger than the electronic conductivity in this temperature range even for very reducing conditions [1973Hin],[1978Del]. It was shown that, however, the difference in conductivity for the heterostructures with different orientation is very small. This means that the conductivity of a $CaF_2(111)/BaF_2(111)$ interface approximately equals to that of a $CaF_2(200)/BaF_2(200)$ interface. In another word, the conductivity is not substantially influenced by the interfacial structure. If the F^--ions were accumulated in the interfacial core of the CaF_2/BaF_2 interfaces the conductivity should be sensitive to its structure. Therefore, the results support the conclusion that F^--ions are transferred from one fluoride to the other in the heterostructures as pointed out earlier in Ref. [2000Sata].

Also, the morphology and interface structures of BaF_2/CaF_2 multilayers with various layer thicknesses have been investigated by conventional transmission electron microscopy (CTEM), high-resolution transmission electron microscopy (HRTEM) [2004NYJ]. In the paper, the dependence of the layer structure on the layer thickness has been analyzed. For large thicknesses, the structure is close to ideal 2D multilayers, and most interface dislocations are lying on the interfaces; in the medium range of thicknesses, wavy interfaces associated with a special configuration of interface dislocations are observed; in case of small thicknesses column-like structures form, and elements Ca and Ba tend to separate in different columns. The layer structure and the formation of extended crystal defects may have strong influences on the density and the mobility of charge carriers in the multilayers that add to the purely chemical effects.

Due to the insulating properties of CaF_2 and BaF_2 epitaxial grown layers on Si have a number of potential applications in the semiconductor industry: semiconductor-on-insulator structures, three dimensional or high-density integrated circuits, improved gate insulators, optoelectronic applications (wave guides). So far, until now all the measurement were made in order to prove a good insulating properties and there are no publications which deal with the ionic conduction perpendicular to the interface.

The first reported high-quality epitaxiy of CaF_2 on Si was made by Ishiwara et al. [1982Ishi]. Some of the earliest results were obtained by Asano et al. [1982Asa], who have successfully grown epitaxial CaF_2 on the (111), (100) and (110) surfaces of Si by evaporation of CaF_2 from Ta boat. Later work with CaF_2 epitaxy on Si using MBE-technique has confirmed previous results [1985Scho]. In fair agreement with the results of Asano et al. they found optimum growth temperatures to be >525°C for the (111) orientation, 500-650°C for the (100) orientation and >775°C for the (110) orientation. The best-quality growth was obtained for (111)-oriented substrates. The CaF_2 has been found to be under a large tensile strain (because of much larger thermal-coefficient of CaF_2 than Si) in the plane parallel to the interface for very thin epitaxial layers. The tensile planar stress appears as the film is cooled down due to misfit dislocations introduced at growth temperature to reduce the strain at that temperature. The mechanism by which strain is relieved with increasing film thickness can be understood if it is assumed that the defects responsible for strain at the growth temperature are "frozen in" [1986Scho]. Also in Ref. [1986Scho] it was reported cracking in all layers grown by MBE using a pyrolytic boron nitride (PBN) crucible to evaporate CaF_2. This was attributed to contamination of the CaF_2 layers with boron.

The atomic structure of CaF_2/Si interface has been studied by a number of analytical tools. These include high-resolution transmission electron microscopy (HRTEM) [1986Pon], and various spectroscopies. It was shown that on both of the (100) and (111) CaF_2/Si interfaces the bonding is due to the Ca-Si bond at the interface. Also, in Ref. [1986Rieg] has been determined the Ca-Si bonding at the interface using high-resolution core level and Auger-electron spectroscopy, angle-resolved photoemission and polarization-dependent near-edge X-ray absorption.

As detailed previously, materials characterization of epitaxial CaF_2 grown on Si has been relatively extensive. However, electrical characterization, which is crucial for most of the potential applications, has been less complete. Electrical characterization of epitaxial CaF_2 on Si has been carried out using current-voltage (I-V), capacitance–voltage (C-V) and conductance-voltage (G-V) measurements on MIS capacitors. Therefore, until now there are no measurements to determine the ionic conductivity of the system in the perpendicular mode.

Chapter 2

Defect Chemical Theory of Space Charge Regions Involving Interfaces

2.1. General Considerations

The introduction of interfaces into substances has been proven to be a powerful tool to tune the properties of the materials. The influence of interfaces on the point defect concentration in immediate neighbourhood can be described by the concept of space charge. This concept provides a natural bridge between bulk properties and those of the neighbouring phase and possesses general importance and is able to explain many aspects of conductivity in heterogeneous systems [2004Maier]. The major purposes were to elucidate the general significance of the defect chemistry in space charge regions and its relevance, especially for transport properties. In the next we follow the Ref. [2004Maier].

In case of the contact of two substances, the boundary effects frequently exceed the volume effects in their importance: p-n junctions, transistors, photo-elements, varistors, Schottky diodes or electrode/liquid electrolyte junctions or colloid chemistry. To exemplify this let take a few examples:

1. The first example involves dipping a solid into aqueous salt solutions, thus, creating a solid-liquid interface. In this case, either cations or anions will be preferentially adsorbed on the surface, and as result an excess of surface charge will appear. The countercharge is distributed in the zone of the solution in the vicinity of the interface, and the width of this region is determined by the Debye length (which is inverse proportional to the square root of the charge carrier concentration in the bulk solution) (Figure 2.1a). For a concentrated solution a rigid double-layer is formed, and for diluted solution a extended diffuse layer appear. Such electrostatic effects are responsible for the kinetic stability of dispersed systems in colloid chemistry.

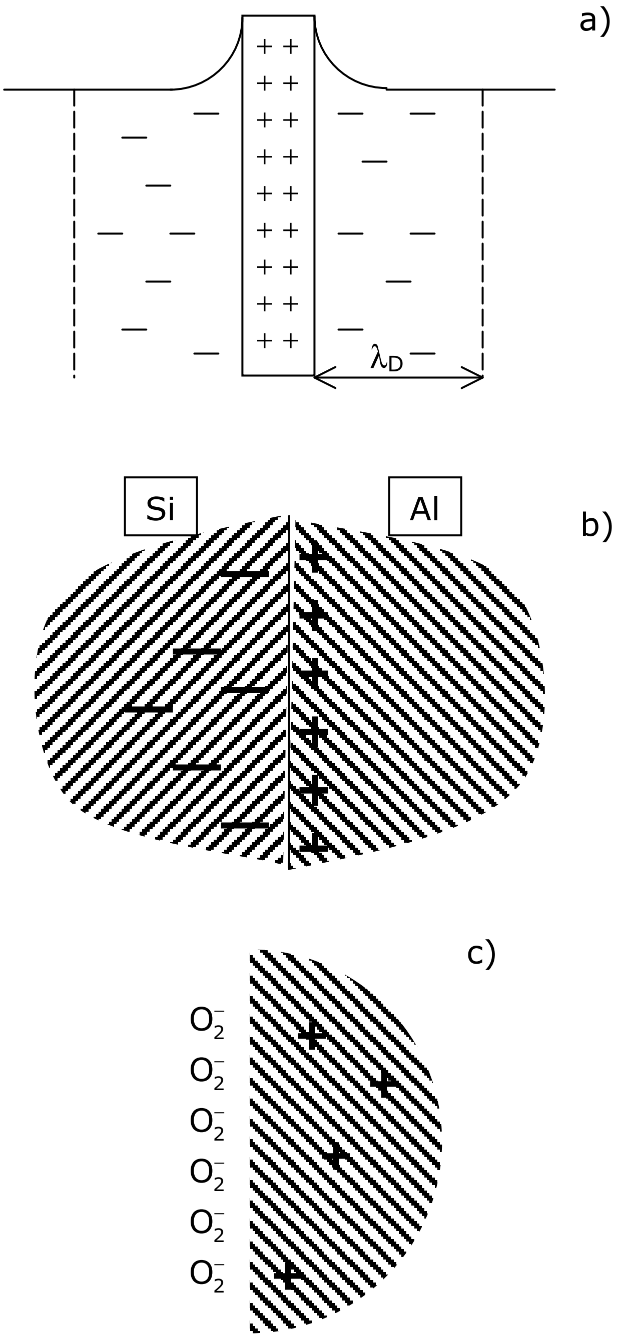

Figure 2.1. Formation of electrical potential difference of interfaces and space charge region with Debye length width.

2. The second example shows the contact between the metal Al and the semiconductor Si. Because of the difference in the electronegativity the electron pass from the Al to the Si and an electric field is produced on account of the charge which by screening limits the extension of the space charge region. Due to the high electron concentration in metallic Al the charge is confined at the surface, while the charged zone in Si is extended to a width which depends on the purity. (Figure 2.1b) Depending on the type of conduction in Si (*n* or *p*), enrichment, depletion or inversion layers can be formed. These boundary layers in semiconductor play an important role in electronic devices, such as diodes, transistors, solar cells.

3. Another example is the solid-gas contact as shown in Figure 2.1c (let us consider the contact between the semiconductor SnO_2 and O_2 gas). At low temperatures the adsorbed oxygen cannot penetrate and remain on the surface. It traps electrons from the boundary layer and makes this positively charged, producing a depletion layer of increased resistance.

The creation of an interface means a break of symmetry of the homogeneous initial situation. If the charge carriers have a sufficient mobility then a charging of the interface can occur.

The final aim is to show how to calculate the defect concentrations in boundary layers as a function of the control parameters: temperature, activity and doping content, the materials parameters of both bulk and interface core. The simplest assumption is that of an abrupt structural transition.

Different applications can be expected in case of contact between two ionic conductors. The most important ones are:

1. Close to the interface the materials parameters may change more smoothly due to a structural adjustment or to gradient energy effects. This includes also elastic effects.
2. Higher dimensional defects such as dislocations may be formed to compensate the interfacial misfit or simply due to non-equilibrium conditions.
3. Thin layers of a third phase may appear, with restricted width (*h*) due to thermodynamic or kinetic reasons.

All these cases can have an influence on the conductivity in the adjacent boundary zone (by affecting the point defect concentration) or can provide a new kinetic path themselves. The region of adjustment is the space charge layer, which consist of a region of redistribution of ionic and/or electronic defects. The space charge concept is of general nature and represents the extension of volume-defect thermodynamics based on the principle of local neutrality.

In the following chapter it is shown how to calculate quantitatively profile of defect concentrations, the partial conductivity and the effective (measured) specific conductivity from local thermodynamic and electrostatic relations. These relations reflect the dependence on geometric parameters, on temperature and on interfacial activity.

2.2. Defect Chemistry

In a Frenkel disordered conductors (M^+X^-) disorder means that some of the cations have left their regular positions (M_M), have occupied interstitial positions (vacant interstitial V_i, occupied interstitial positions $M_i^\bullet$) and have left behind vacancies (V_M'):

$$M_M + V_i \rightleftharpoons M_i^\bullet + V_M' \tag{2.1}$$

In contrast to the regular particles, $M_i^\bullet$ and V_M', are typical mobile ion centres. When the concentration of electronic defects and of impurity ions is negligible, the bulk concentrations of ionic defects must be equal and fixed by the mass action constant (K_F-Frenkel constant) due to the necessity for local electrical neutrality:

$$\left[M_i^\bullet\right] = \left[V_M'\right] = \sqrt{K_F\left(T\right)} = \exp - \frac{\Delta_F G^0}{2RT} \tag{2.2}$$

Where $\Delta_F G^0$ is the standard free enthalpy of the reaction, and $\left[M_i^\bullet\right]$ and $\left[V_M'\right]$ refer to the concentrations of the interstitials and vacancies.

(In contrast, in an anti-Frenkel disordered conductors (e.g. CaF_2 or BaF_2) disorder means that some of the anions move from their regular positions (F_F), occupy interstitial positions (free vacant interstitial V_i, occupied interstitial positions F_i') and have left behind vacancies ($V_F^\bullet$):

$$F_F + V_i \rightleftharpoons F_i' + V_F^\bullet \tag{2.3}$$

And also a mass action law can be written in same way.)

At the interface between the two ion conductors, ion redistribution in the space charge region is required from the thermodynamic point of view. In the case of local equilibrium it is sufficient to transport one defect type from the bulk of each phase to the common interface. This can be described by an electrochemical reaction of the form A(x)=B(x’) and the spatial equilibrium is represented by the equality of the electrochemical potential:

$$\widetilde{\mu}_A(x) = \widetilde{\mu}_B(x') \tag{2.4}$$

If we assume dilute states (electrochemical potential is then linear in the logarithm of the mole fraction of the defects), then the result is:

$$\mu_A^0 + RT\ln c_A(x) + z_A F\phi(x) = \mu_B^0 + RT\ln c_B(x') + z_A F\phi(x') \tag{2.5}$$

or

$$\frac{c_B(x')}{c_A(x)} = \exp - \frac{\mu_B^0 - \mu_A^0}{RT} \exp - \frac{z_A F\left[\phi(x') - \phi(x)\right]}{RT} \tag{2.6}$$

where μ_j^0 is standard chemical potential, ϕ is electrical potential.

We assume that the structure of the material remains intact up to the interface (μ_j^0 is independent of the distance from the interface) and the same mobility of defects in the space charge layers and in the bulk. Also we assume that we know the bulk concentration of the mobile carrier *j* ($c_{j,\infty}$) as a function of temperature, component activity and doping content.

The concentration enhancement is the concentration of the mobile carrier *j* ($c_j(x)$) relative to the bulk ($x = \infty$), which can be given as:

$$\zeta_j^{1/z_j}(x) = \left[\frac{c_j(x)}{c_{j,\infty}}\right]^{1/z_j} = \exp\left\{-\frac{e\left[\phi(x) - \phi_\infty\right]}{k_B T}\right\} \tag{2.7}$$

where k_B is Boltzmann constant (k_B=1.38x10^{-23}J/K), *e* denotes elementary charge (*e*=1.6022x10^{-19}C) and *T* is temperature.

The expression ζ_j^{1/z_j} is evidently independent of the type of the mobile carrier (interstitials or vacancies, electrons or holes). A given electrical potential difference influences all mobile charge carriers according to their charge. If all defects are effectively monovalent, a positive value of the electrical potential difference ($\phi(x) - \phi_\infty$) will deplete all positive charge carriers by the factor $\exp\left|\frac{e\Delta\phi}{k_B T}\right|$, while all the negative charge carriers will be enriched by the same factor. This is shown in Figure 2.2 for the (a) Frenkel and (b) anti-Frenkel conductors.

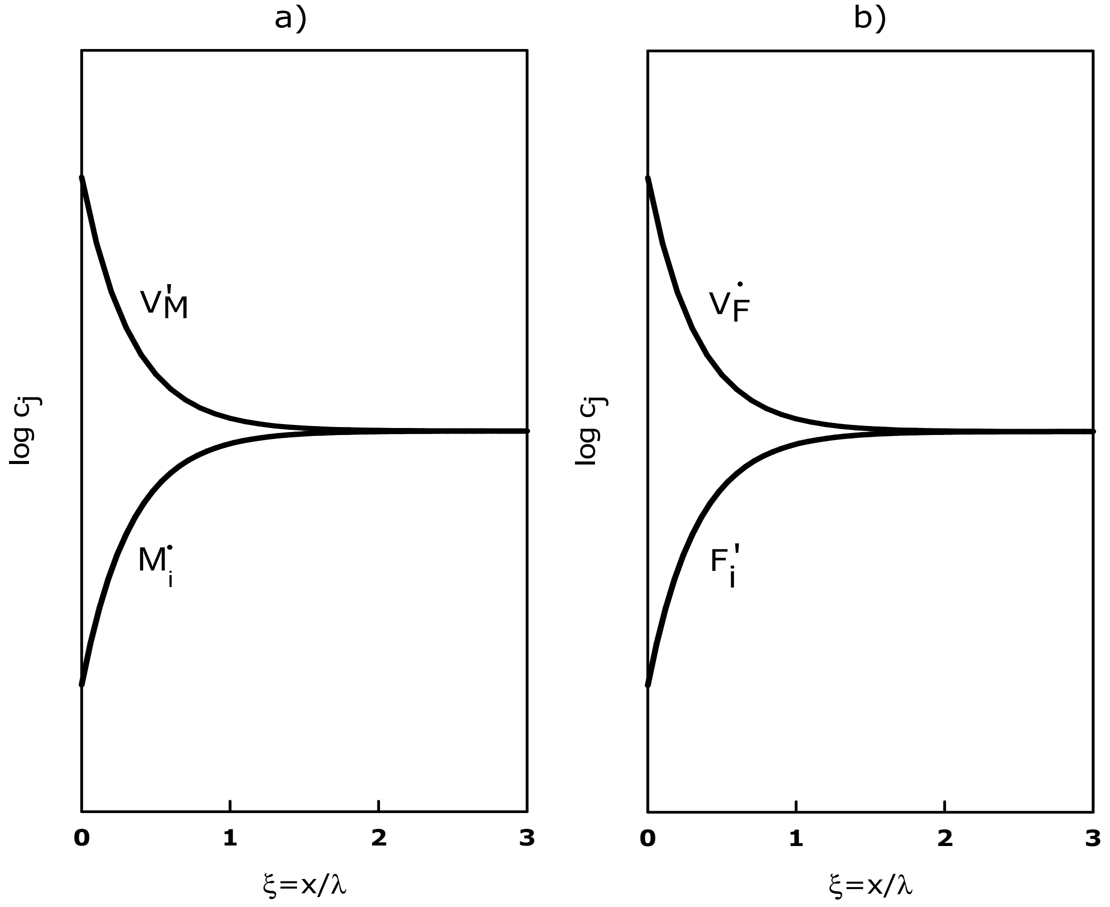

Figure 2.2. The defect concentration profile for positive electrical interface potential in a ionic conductor containing a) Frenkel defects (AgCl, AgBr…, M=Ag) and b) anti-Frenkel defects (CaF_2, BaF_2…).

The value of the interface potential is determined by chemical interaction and will be strongly dependent on the neighbouring phase and on temperature. Taking into account the first Maxwell equation, the curl of the electrical field is zero in absence of time dependent magnetic field.

$$\nabla x E = 0 \qquad (2.8)$$

The second Maxwell equation states that charges are sources of the dielectric displacement field, and we assume that the dielectric constant $\varepsilon\varepsilon_0$ is uniform in all directions, also of the electrical field:

$$\nabla E = -\frac{\rho}{\varepsilon\varepsilon_0} \qquad (2.9)$$

where ρ denote charge density (which is obtained from the defect concentration using $\rho = \sum_k z_k e c_k$), ε and ε_0 are the relative permittivity and the dielectric constant of free space, z_k is the charge number of the defect k.

By combination of the two Maxwell equations, eq. (2.8) and (2.9), we obtained the electrical potential, which is related to the charge density via the Poisson equation:

$$\nabla^2 \phi = -\frac{\rho}{\varepsilon\varepsilon_0} \tag{2.10}$$

This equation (2.10), combined with the condition of the continuity of the electrochemical potential (2.7), in one-dimensional form reads:

$$\frac{d^2}{dx^2}\left[\phi(x) - \phi_\infty\right] = -\frac{e}{\varepsilon\varepsilon_0}\sum_k c_{k,\infty} z_k \exp-\left[z_k e \frac{\phi(x) - \phi_\infty}{k_B T}\right] \tag{2.11}$$

This relation is very well known in literature as the Poisson-Boltzmann equation.

2.3. Concentration Profiles in the Space Charge Zones

The solution of Poisson-Boltzmann equation for the semi-infinite boundary conditions leads to Gouy-Chapman profiles of concentration of the charge carriers. If contrarily we have to assume that the charge density ρ is frozen and constant, we obtain a Mott-Schottky profile.

2.3.1. Gouy-Chapman Profiles

In the following we consider the case that only two major charge carriers are relevant. They are equivalently but oppositely charged (subscripts + and -): $z_+ = |z_-| = z$. This is important for the discussion of the intrinsic regime in ion conductors, and there are no problems in the application to other charge carriers so long as the absolute charge numbers are the same. For reasons of electroneutrality the bulk concentrations are equal: $c_{+,\infty} = c_{-,\infty} = c_\infty$. In term of the concentration enhancement ζ we obtain the differential equation which can be written as:

$$\frac{d^2 \ln \zeta_\pm}{d(x/\lambda)^2} = \frac{1}{2}\left(\zeta_\pm - \zeta_\mp\right) \tag{2.12}$$

where *x* is the distance from the interface. As a result, $x = 0$ and $x = \infty$ refer to the interface and the bulk, respectively. λ is the Debye length,

$$\lambda = \left(\frac{\varepsilon\varepsilon_0 k_B T}{2z^2e^2c_\infty}\right)^{1/2} \tag{2.13}$$

If both defects are mobile and in case of electrochemical equilibrium, then $\zeta_\pm = \zeta_\mp^{-1}$. The differential equation of the concentration enrichment (2.12) can be rewritten as:

$$\frac{d^2 \ln \zeta_\pm}{d(x/\lambda)^2} = \frac{1}{2}\left(\zeta_\pm - \zeta_\pm^{-1}\right) \tag{2.14}$$

The equation (2.14) can be integrated using the boundary condition:

$$\zeta_{\pm}(x=0)=\zeta_{\pm 0} \text{ and } \zeta_{\pm}(x\to\infty)=\zeta_{\pm\infty}=1 \qquad (2.15)$$

The result is applicable over the entire local coordinate range and also for smaller splitting effects:

$$\zeta_{\pm}(x)=\frac{c_{\pm}(x)}{c_{\pm\infty}}=\left(\frac{1+\vartheta_{\pm}\exp(-x/\lambda)}{1-\vartheta_{\pm}\exp(-x/\lambda)}\right)^{2}=\zeta_{\mp}^{-1}(x) \qquad (2.16)$$

The parameter ϑ is dependent on ζ_0 and, hence, on c_0, and is defined by

$$\vartheta_{\pm}=\frac{\zeta_{\pm 0}^{1/2}-1}{\zeta_{\pm 0}^{1/2}+1}=-\vartheta_{\mp} \qquad (2.17)$$

This parameter represents the degree of influence [1985Ma2]. In the following we follow Ref. [1995Ma1]. For $\vartheta=0$ (i.e. $\zeta_{\pm 0}=1$) in the space charge region the defect chemistry is the same as in the bulk (this is known as the flat band case or zero charge case in the semiconductor physics or electrochemistry respectively). It approaches +1 for the maximum enrichment ($\zeta_{\pm 0}\gg 1$) and -1 for maximum depletion ($\zeta_{\pm 0}\ll 1$) (Figure 2.3).

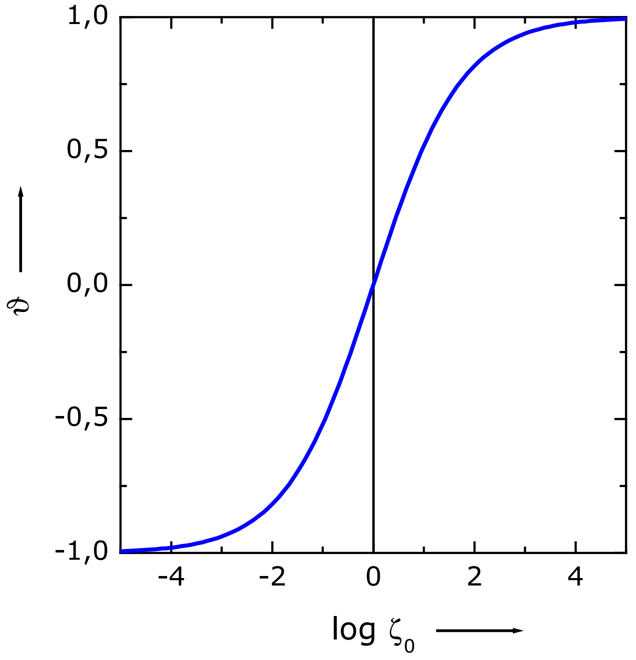

Figure 2.3. The relation between the degree of influence and the concentration increase at the interface [1985Ma2].

The changes in defect cosncentrations as a result of space charge effects are of direct and crucial importance in questions of reactivity, catalysis and interfacial kinetics, and they are of particular significance with respect to electrical effects.

Depending of the space charge situation the conductivity type (ionic/electronic) can change as a function of the space charge potential. This is the case in which an ionic and an electronic defect are the majority charge carriers (mixed conductors).

2.3.2. Mott-Schottky Profiles

While Gouy-Chapman profiles serve as a natural picture for accumulation layers, enrichment effects can also be found in Mott-Schottky situations. Then the conductivity determining carrier has to be a minority carrier with high mobilities in order to surpass the bulk value significantly. Now we refer to an extrinsic situation in which the mobile majority species are impurity compensated, with a flat impurity profile (Figure 2.4). The impurity is assumed to be incorporated during preparation but immobile under measurements temperature.

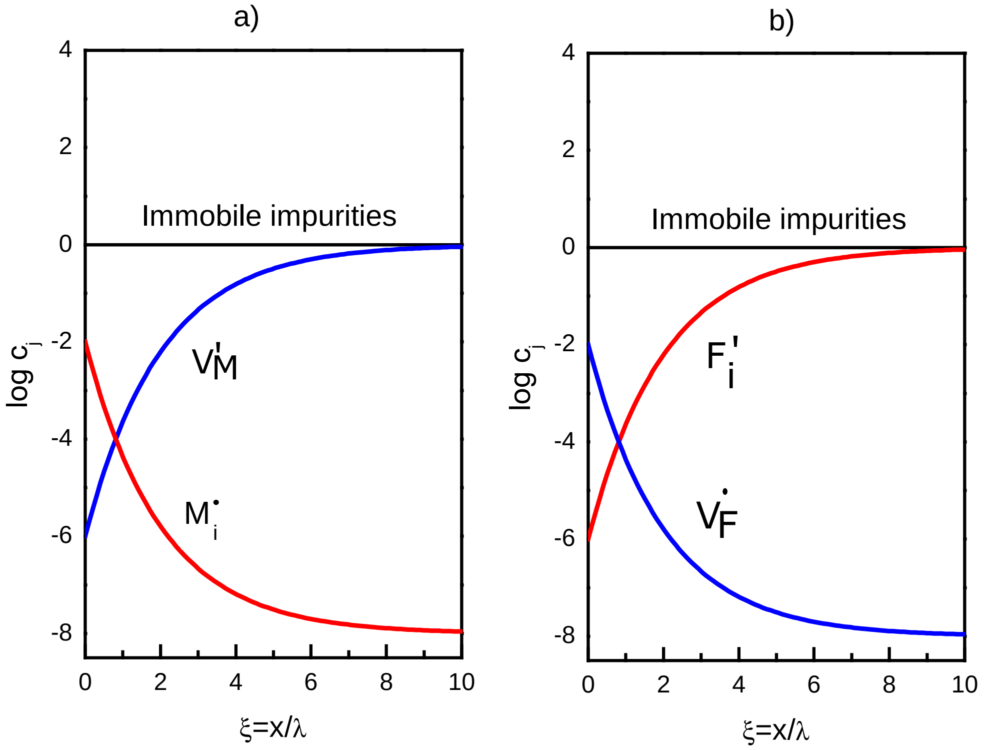

Figure 2.4. The defect concentration profiles for positive immobile impurities in a ionic conductor containing a) Frenkel defects (AgCl, AgBr…, M=Ag) and b) anti-Frenkel defects (CaF_2, BaF_2…).

Even in extrinsic situations in which the mobile majority defects are accumulated, the Poisson-Boltzmann equation (2.11) is still valid. If it is however depleted as assumed in the Mott-Schottky model, the constant quantity $c_{imp,\infty}$ dominates the charge density and hence Poisson's equation becomes:

$$\frac{d^2}{dx^2}\phi(x) = \begin{cases} -\dfrac{z_{imp}ec_{imp,\infty}}{\varepsilon\varepsilon_0} = \text{const}, & 0 < x \le \lambda^* \\ 0, & x \ge \lambda^* \end{cases} \tag{2.18}$$

This equation (2.18) can be easily integrated with the boundary conditions $\phi'(\lambda^*) = 0$ and $\phi(\lambda^*) = \phi_\infty$, resulting in a parabolic potential profile:

$$\phi(x) = \frac{-z_{imp}ec_{imp,\infty}}{2\varepsilon\varepsilon_0}\left(x - \lambda^*\right)^2 + \phi_\infty \tag{2.19}$$

where λ^* is defined as the effective space charge thickness:

$$\lambda^* = \sqrt{\frac{2\varepsilon\varepsilon_0}{z_{imp} e c_{imp,\infty}}\left(\phi_\infty - \phi_0\right)} \tag{2.20}$$

A comparison with the Debye length (λ) shows that:

$$\frac{\lambda^*}{\lambda} = \sqrt{\frac{4 z_{imp} e}{k_B T}\left(\phi_\infty - \phi_0\right)} \tag{2.21}$$

When the ratio λ^*/λ becomes larger the interfacial effect increases. In the Gouy-Chapman case, the space charge effect was concentrated strongly at $x = 0$, even for large potentials, and the layer could not penetrate into the material because of the stronger screening. Figure 2.5 compares the two cases and shows that for the same value of the interfacial potential the space charge region in the Mott-Schottky case is significantly more extended than in the Gouy-Chapman case.

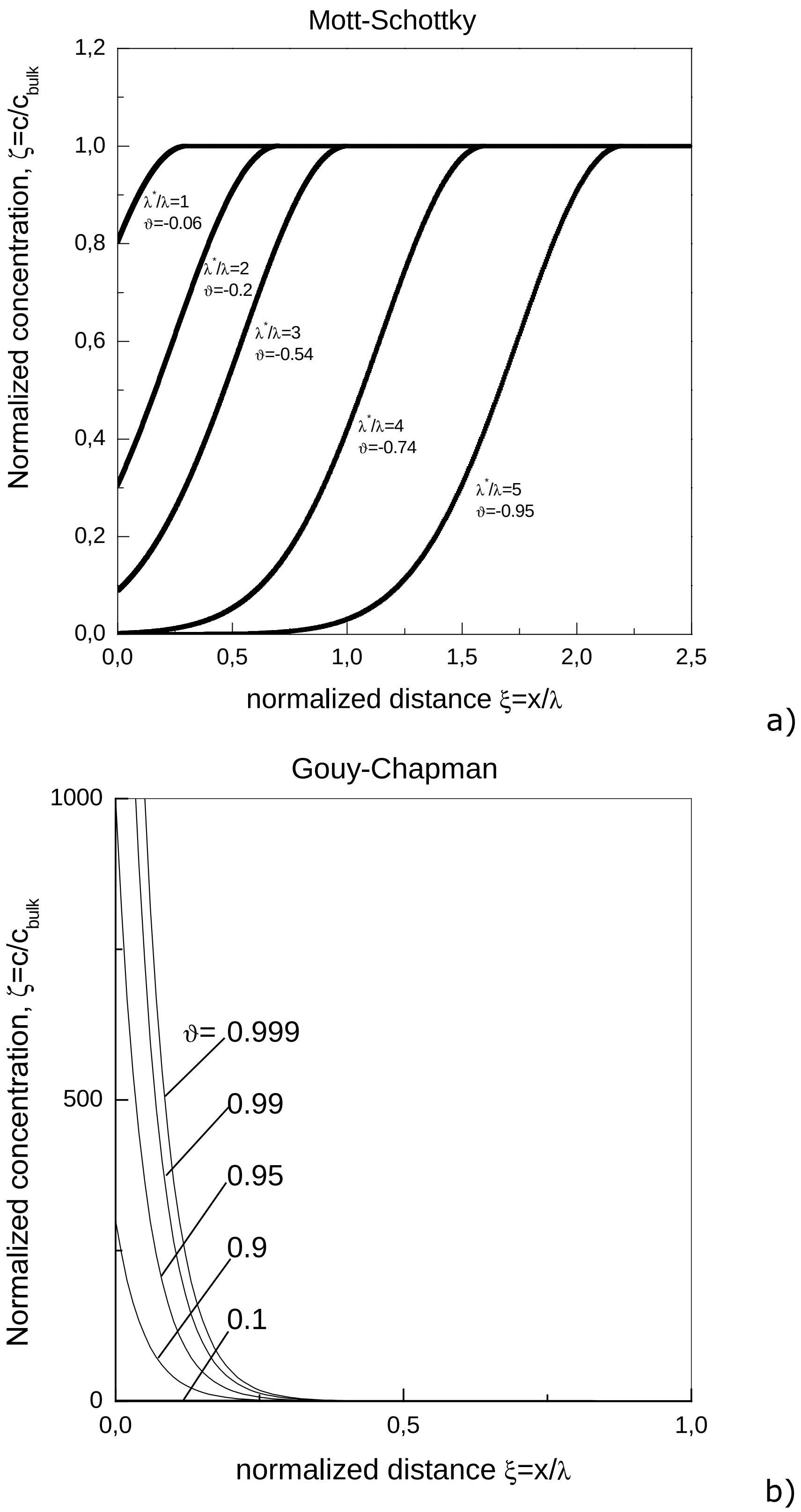

Figure 2.5. a) Depletion profile in the Mott-Schottky case and b) ehancement profiles in the Gouy-Chapman case as a function of the strength of the effect measured by ϑ.

As the depletion increases ($\vartheta \to 1$) the boundary layer is almost cleaned out. At the point $x = \lambda^*$ the concentration reaches the bulk value. When $x \le \lambda^*$ the defect concentration can be written:

$$\zeta_j^{1/z_j}(x) = \left[\frac{c_j(x)}{c_{j,\infty}}\right]^{1/z_j} = \exp\left(\frac{x-\lambda^*}{2\lambda}\right)^2 \qquad (2.22)$$

In the overlap situation (when thickness of layer is smaller than $2\lambda^*$), the electroneutrality is not obeyed and the layer is charged throughout. Rather in this case, the boundary conditions are $\phi'(x = \ell/2) = 0$ and $\phi(x = 0) = \phi_0$. Therefore, the integration of Poisson's equation (2.10) yields a potential profile [2006Jam],[2007Ma]:

$$\phi(x) = \frac{-z_{imp}ec_{imp,\infty}}{2\varepsilon\varepsilon_0}\left[\left(x-\frac{\ell}{2}\right)^2 - \left(\frac{\ell}{2}\right)^2\right] + \phi_0 \qquad (2.23)$$

and the defect concentration profile:

$$\zeta_j^{1/z_j}(x) = \left[\frac{c_j(x)}{c_{j,\infty}}\right]^{1/z_j} = \exp\left\{\frac{z_{imp}}{4\lambda^2}\left[\left(x-\frac{\ell}{2}\right)^2 - \left(\frac{\ell}{2}\right)^2\right] - \frac{z_{imp}e}{k_BT}(\phi_0 - \phi_\infty)\right\} \qquad (2.24)$$

Since the mobile majority carrier is depleted, Mott-Schottky case usually deals with resistive boundaries. If a minority carrier of the same sign as the impurity has a very high mobility (u_{mi}/u_{ma} ratio should be very high), it can be conceived that its accumulation can lead to an increase in the overall conductance, even though the impurity level is not exceeded.

2.4. Conductivity Effects

When conductivity measurements are performed in the direction perpendicular to the active interface, the most strongly insulating part of the profile is responsible for the electrical properties, while measurements parallel to the active interface senses the highly conducting parts. Electrical depletion layers are preferably investigated in the first mode, enrichment layers in the second mode.

The lateral conductivity is the sum of all the mobile carriers in the layer.

$$\sigma_{\mathrm{m}}^{||} = \sum_{\mathrm{j}} \sigma_{\mathrm{j},\infty}^{||} \frac{1}{\ell} \int_0^{\ell} \frac{\mathrm{c_j(x)}}{\mathrm{c}_{\mathrm{j},\infty}} \mathrm{dx} \tag{2.25}$$

where ℓ is the thickness of the layer.

2.4.1. Gouy-Chapman Case

In this case both defects are in spatial equilibrium with $z_+ = |z_-| = z$. Let consider the case of Frenkel defects, in which $V_M^{'}$ are enriched and $M_i^{\bullet}$ are depleted at the interface, for a positive interfacial potential.

For large interfacial spacings ($\ell > 4\lambda$) the concentration profile can be integrated analytically and is found that the contributions of the two defects can be divided in the contribution of the bulk (which extend through the whole sample as a background value right up to the boundary), given by $\sigma_{\pm,\infty}$, and an excess value $\Delta\sigma_{\pm}^{||}$ [1987Ma1].

$$\Delta\sigma_{\pm}^{||} = \frac{4\lambda}{\ell} \sigma_{\pm,\infty} \left(\frac{2\vartheta_{\pm}}{1 - \vartheta_{\pm}} \right) \tag{2.27}$$

and the total conductivity of each defect can be expressed as:

$$\sigma_{\pm}^{||} = \sigma_{\pm,\infty} + \Delta\sigma_{\pm}^{||} = \sigma_{\pm,\infty} + \frac{4\lambda}{\ell} \sigma_{\pm,\infty} \left(\frac{2\vartheta_{\pm}}{1 - \vartheta_{\pm}} \right) \tag{2.28}$$

The total excess in the conductivity is given by the sum of the excess contributions of both defects: $\Delta\sigma^{||} = \Delta\sigma_{+}^{||} + \Delta\sigma_{-}^{||}$.

In the case of large effects $\vartheta_- \to 1$ (for Frenkel defects or $\vartheta_+ \to 1$ for anti-Frenkel defects) and $1 - \vartheta_- \to 2\zeta_{-0}^{-1/2}$ and as result:

$$\sigma_-^{||} = \sigma_{-,\infty} + 2\frac{2\lambda}{\ell}\sigma_{-,\infty}\sqrt{\frac{c_{-0}}{c_{-\infty}}} = \sigma_{-,\infty} + \frac{2}{\ell}u_-\sqrt{2\varepsilon\varepsilon_0 k_B T c_{-0}} \tag{2.29}$$

In equation (2.29) the double Debye length (2λ) play the role of an effective thickness. The geometric mean of the two extreme concentrations ($\sqrt{c_{-0}c_{-\infty}}$) plays the role of an effective concentration.

For very small spacings ($\ell < 4\lambda$), the sample is charged overall and $\zeta_{\pm,\ell/2} = 1$ is no longer valid in the sample centre, but $\phi'(x = \frac{\ell}{2}) = 0$ does for symmetry reasons. Using approximation $\Delta\sigma_m^{||} \propto d\phi/dx\big|_{x=0}$ integration of the concentration profiles (2.16) leads to [1987Ma1], [2004Ma]:

$$\sigma_{\pm\ell}^{||} \cong \Delta\sigma_{\pm\ell}^{||} \cong \frac{2}{\ell}u_\pm\sqrt{2\varepsilon\varepsilon_0 k_B T(c_{\pm 0} - c_{\pm\ell/2})} \tag{2.30}$$

where $c_{\pm\ell/2}$ is the concentration in the centre, which is correlated with $c_{\pm 0}$ and ℓ via elliptical integrals of the first kind.

Comparing $\Delta\sigma_{\pm\ell}^{||}$ in case of $\ell < 4\lambda$, from equation 2.30) with that for $\ell = 4\lambda$ in equation (2.29), we can see that the space charge conductivity is increased by a factor of:

$$g_{GC} = \frac{4\lambda}{\ell}\sqrt{\frac{c_{\pm 0} - c_{\pm\ell/2}}{c_{\pm 0}}} \tag{2.31}$$

This represents the so-called nanosize factor [1995Ma1] corresponding to the overlap situation in the nanosized systems, and it can be calculated numerically. This factor compares the conductivity with the value at 4λ where the space charge zones are assumed to touch and start overlapping. The conductivity calculated in this situation gives results which are always smaller than the value extrapolated from semi-infinite layer, from equation (2.29) (extrapolated values assumed for the semi-infinite layers to finite situations and hence is beyond its range of validity).

2.4.2. Mott-Schottky Case

For large interfacial spacings ($\ell > 2\lambda^*$), from equation (2.25) and (2.22) the total conductivity can be written as contribution of both defects:

$$\sigma_m^{||} = \sigma_{+,\infty}^{||}\frac{1}{\ell}\int_0^{\ell}\frac{c_+(x)}{c_{+,\infty}}dx + \sigma_{-,\infty}^{||}\frac{1}{\ell}\int_0^{\ell}\frac{c_-(x)}{c_{-,\infty}}dx = \\ = \sigma_{+,\infty}^{||}\frac{2}{\ell}\int_0^{\ell/2}\frac{c_+(x)}{c_{+,\infty}}dx + \sigma_{-,\infty}^{||}\frac{2}{\ell}\int_0^{\ell/2}\frac{c_-(x)}{c_{-,\infty}}dx \tag{2.32}$$

or

$$\sigma_m^{||} = \sigma_{+,\infty}^{||}\frac{2}{\ell}\int_0^{\ell/2}\exp\left[z_+\left(\frac{x-\lambda^*}{2\lambda}\right)^2\right]dx + \sigma_{-,\infty}^{||}\frac{2}{\ell}\int_0^{\ell/2}\exp\left[z_-\left(\frac{x-\lambda^*}{2\lambda}\right)^2\right]dx \tag{2.33}$$

Since beyond λ^* the concentration reaches the bulk value, $\zeta_-^{-1}(x > \lambda^*) = \zeta_+(x > \lambda^*) = 1$, the contribution of each species follow:

$$\sigma_\pm^{||} = \sigma_{\pm,\infty}^{||} + \sigma_{\pm,\infty}^{||}\frac{2}{\ell}\int_0^{\lambda^*}\exp\left[z_\pm\left(\frac{x-\lambda^*}{2\lambda}\right)^2\right]dx \\ = \sigma_{\pm,\infty}^{||} + \sigma_{\pm,\infty}^{||}\frac{4\lambda}{\ell}\int_0^{\lambda^*/2\lambda}\exp\left[z_\pm\xi'^2\right]d\xi' \tag{2.34}$$

where $\xi' = \dfrac{x-\lambda^*}{2\lambda}$ is a normalized coordinate for simplicity of calculation.

The analytical integration of this type of integral is not possible, but equation (2.34) already indicates that the conductivity is proportional to the inverse interfacial spacing ($1/\ell$), taking into account that $\lambda^*/2\lambda$ is a constant determined by the space charge potential difference as defined in equation (2.21).

In the case of small spacings ($\ell < 2\lambda^*$), the calculations should use equation (2.24). The total lateral conductivity of each species is given by:

$$\sigma_{\pm}^{||} = \frac{2}{\ell}\sigma_{\pm,\infty}\int_0^{\ell/2} \exp\left\{\frac{z_{\pm}}{4\lambda^2}\left[\left(x-\frac{\ell}{2}\right)^2-\left(\frac{\ell}{2}\right)^2\right]-\frac{z_{\pm}e}{k_BT}(\phi_0-\phi_\infty)\right\}dx$$

(2.35)

To calculate the total conductivity, numerical integration of the contribution of each defect has been computed. The numerical results will be discussed in Chapter 6.

2.5. Example of Space Charge Zones: CaF_2/BaF_2 Heterolayers

The contact of two heterogeneous ionic systems can lead to a creation of a space charge zone at the interface. In such case different effects can occur at the interface and affect the conductivity of the materials. One reason for conductivity effects is due to the thermodynamic redistribution of fluoride ions from one phase to the other according to the different free energy levels in the two phases. This leads to an increase of the fluoride vacancy concentration in one conductor and of the fluoride interstitial concentration in the other conductor. The second mechanism is a unilateral or bilateral transfer of F^- to or from the interface layer in order to the lower interfacial core free energy.

According to the space charge profile from Figure 2.2b (Gouy-Chapman case) and from experimental evidence we can assume that F_i' and $V_F^{\bullet}$ carriers should be enriched in the space charge zones of CaF_2 and BaF_2, respectively. Figure 2.6 shows the defect concentration profile at the interface between CaF_2 and BaF_2 regarding the above mechanism in space charge regions.

For such large effect, $\vartheta_{\pm} \rightarrow 1$ and $1-\vartheta_{\pm} \rightarrow 2\zeta_{\pm 0}^{-1/2}$. As a result, Eq. (2.28) can be rewritten for F_i' in CaF_2 and $V_F^{\bullet}$ in BaF_2 as:

$$\sigma_i^{||}(CaF_2) = \sigma_{i,\infty}^{CaF_2} + 2\frac{2\lambda}{\ell}\sigma_{i,\infty}^{CaF_2}\sqrt{\frac{c_{i,0}^{CaF_2}}{c_{i,\infty}^{CaF_2}}} = \sigma_{i,\infty}^{CaF_2} + \frac{2}{\ell}u_i^{CaF_2}\sqrt{2\varepsilon^{CaF_2}\varepsilon_0 k_B T c_{i,0}}$$

respectively, (2.36a)

$$\sigma_v^{||}(BaF_2) = \sigma_{v,\infty}^{BaF_2} + 2\frac{2\lambda}{\ell}\sigma_{v,\infty}^{BaF_2}\sqrt{\frac{c_{v,0}^{BaF_2}}{c_{v,\infty}^{BaF_2}}} = \sigma_{v,\infty}^{BaF_2} + \frac{2}{\ell}u_v^{BaF_2}\sqrt{2\varepsilon^{BaF_2}\varepsilon_0 k_B T c_{v,0}}$$

(2.36b)

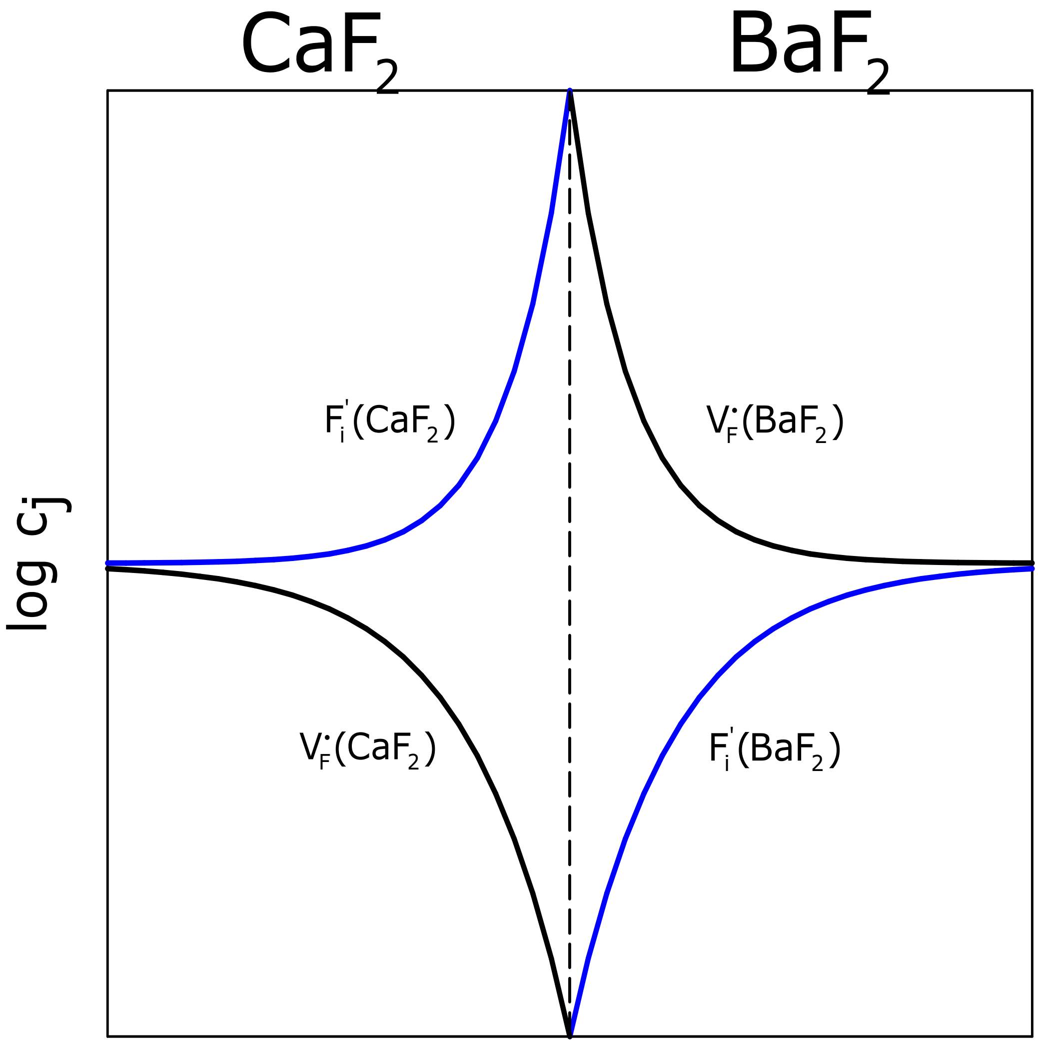

Figure 2.6. The defect concentration profile at the interface between CaF_2 and BaF_2: enrichment of the $F_i^{'}$ and $V_F^{\bullet}$ carriers in the space charge zones of CaF_2 and BaF_2 respectively.

Using Eq. (2.36a) and (2.36b), in case of only 2 layers (one CaF_2 and one BaF_2) the total conductivity can be expressed as:

$$\sigma_m^{||} = \sigma_{m,i}^{||}(CaF_2) + \sigma_{m,v}^{||}(BaF_2) \tag{2.37}$$

In case of *n* layers (total number of layers of CaF_2 and BaF_2) the total conductivity parallel to the interface can be written as follow:

$$\sigma_m^{||} \cong \frac{\sigma_m^{BaF_2}}{2} + \frac{\sigma_m^{CaF_2}}{2} + \frac{1}{\ell} \cdot \frac{n-1}{n} \cdot \left[u_v^{BaF_2} \sqrt{2\varepsilon^{BaF_2}\varepsilon_0 k_B T c_{v,0}^{BaF_2}} + u_i^{CaF_2} \sqrt{2\varepsilon^{CaF_2}\varepsilon_0 k_B T c_{i,0}^{CaF_2}} \right] \tag{2.38}$$

In Eq. (2.38) the effect of the top surface and the space charge contribution from the substrate were neglected. The contribution of the gas/solid interface is very small because it is only a single interface and this effect is expected to be much weaker than the effect of the substrate with its specific interaction.

If we assume a maximum interfacial effect (all possible sites at the interface are occupied by defects) in a simple continuum model $c_0^{BaF_2} = 1/V_m^{BaF_2}$ and $c_0^{CaF_2} = 1/V_m^{CaF_2}$ (V_m: molar value), we obtain the equation:

$$\sigma_m^{||} = \frac{\sigma_m^{BaF_2}}{2} + \frac{\sigma_m^{CaF_2}}{2} + \frac{1}{\ell} \cdot \frac{n-1}{n} \cdot \left[u_v^{BaF_2} \sqrt{\frac{2\varepsilon^{BaF_2}\varepsilon_0 k_B T}{V_m^{BaF_2}}} + u_i^{CaF_2} \sqrt{\frac{2\varepsilon^{CaF_2}\varepsilon_0 k_B T}{V_m^{CaF_2}}} \right] \tag{2.39}$$

The Eq. (2.30), (2.31), (2.38) and (2.39) was used to calculate the total conductivity of CaF_2/BaF_2 heterolayers, and also for fitting the experimental results. The numerical parameters and fitting results will be discussed in Chapter 6.

For the Mott-Schottky case, the equations used to calculate the total conductivity of CaF_2/BaF_2 heterolayers, (2.34) and (2.35), cannot be given as an analytical expression. Integration of this type of integral is done numerically and the results of fitting are detailed in Chapter 6.

Chapter 3

Physical and Electrical Properties of Calcium and Barium Fluoride

In recent years an increasing number of physical properties of different solid inorganic fluorides have been studied. The electronic localization that characterizes the fluorides allows better insight into solid-state research, and the applications of solid fluorides are various (e.g. related to optical, electrical, and energetic properties): silicon-on-insulator technology, epitaxial gate dielectrics, and three-dimensional integrated circuits. For these materials many future developments can be predicted based on such specific features as low refractive index, low boiling or melting point, and high ionic conductivity. Ionic conductors, materials in which specific ions can migrate preferentially with high mobility, are of prime importance for electrochemical measurements, and for devices such as high-temperature solid-state batteries and fuel cells, chemical filters and gas sensors [1957Ure],[1973Boll1],[1973Boll2],[1968Bars1],[1968Bars2],[1985Hag].

Among solid electrolytes, fluorine ion conductors have become a research field of growing importance. Materials with very good performance have been chosen as models of superionic conductors due to their structural simplicity and availability as large single crystals. The fluorine conductors have a significant anionic conduction at relatively low temperatures as a consequence of the higher mobility of F^- due to the smaller size, as well as its single charge, but even more because of less covalent bonding. As a consequence, these materials are amongst the best anionic conductors. Due to the high electronegativity of fluorine, most fluorides have large energy gap and often these materials are electronic isolators. Furthermore, the small size of F^- makes it a good candidate as a mobile ion in solids. Many investigations of CaF_2 and BaF_2 have been carried out and proved that these materials are ionic conductors (see e.g. in Ref. [1957Ure], [1973Boll1], [1973Boll2], [1968Bars1], [1968Bars2], [1985Hag]).

3.1. Structural and Physical Properties

The physical properties of ionic conductors are of great technical importance and have been a major reason for studying these systems. Detailed properties of the fluorides ion conductors are given in Ref. [1985Hag] as we consider in the following.

In this study CaF_2 and BaF_2 ion conductors were analyzed due to the relative low melting point, high cation polarizability and high ionic conductivity at lower temperature compared to other fluorides [1973Boll1],[1973Boll2],[1968Bars1],[1968Bars2],[1995Saito],[1999Puin].

CaF_2 and BaF_2 have both the same cubic fluorite structures as shown in Figure 3.1. In the fluorite structure the cations (Ca^{2+} or Ba^{2+}) form a face-centred cubic array and the fluorine anions (F^-) occupy the eight tetrahedral interstices formed by the large cations. These anions can also be represented as forming a simple cube penetrating the face-centred cubic array of cations. In other words, we can also view the structure as a simple cubic array of fluorine atoms with a calcium atom in the centre of alternate cubes.

The crystallographic unit cell dimensions and physical properties are summarized in Table 3.1.

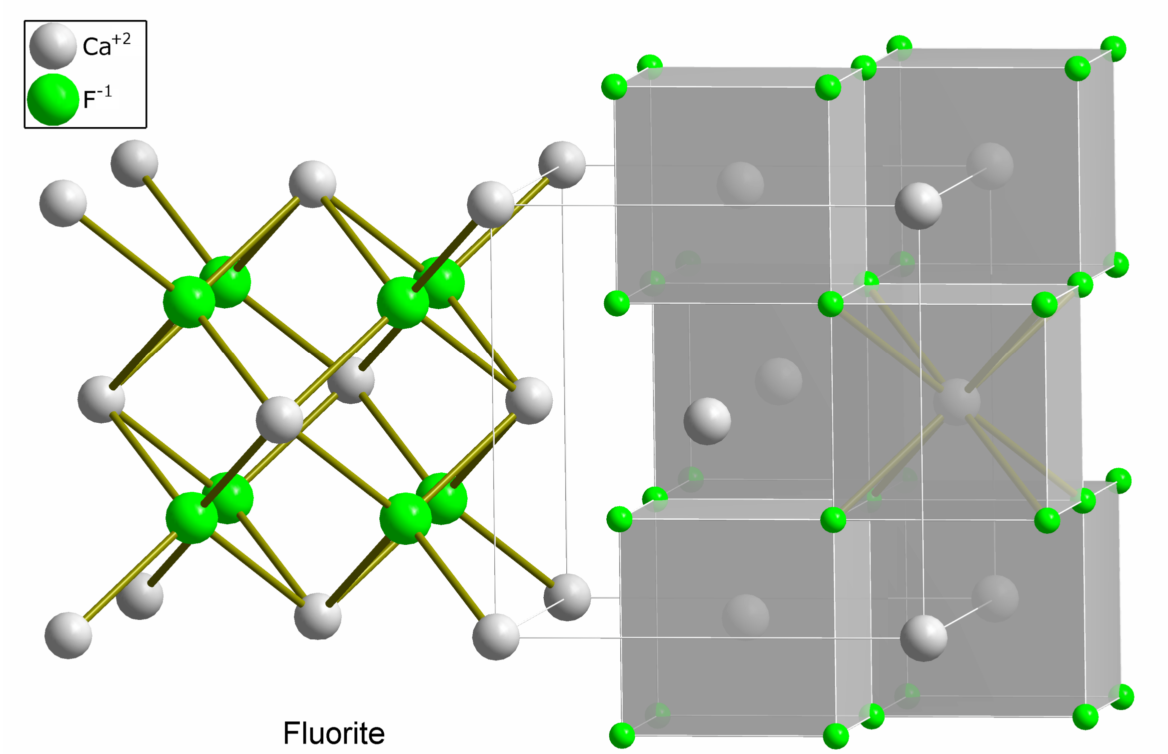

Figure 3.1. Unit cell of CaF_2 (or BaF_2) with fluorite structure.

Compound	**BaF_2**	**CaF_2**
Crystal Structure	Cubic fluorite	Cubic fluorite
Lattice constant (Å)	6.196	5.464
Thermal expansion coefficient at 298K (K^{-1})	18×10^{-6}	19×10^{-6}
Relative permittivity (ε_r)	7.4	6.8
Melting point (°C)	1355	1430
Band gap (eV)	11.0	12.1

Table 3.1. Structural and physical properties of CaF_2 and BaF_2 having the cubic fluorite structure

Compound	BaF_2	CaF_2
Intrinsic Disorder Type	anti-Frenkel	anti-Frenkel
h_F (eV)	$1.6^{(a)}$ $1.9\pm0.1^{(b)}$	$2.45^{(a)}$
h_i (eV)	$0.83^{(a)}$ $0.79\pm0.3^{(b)}$	$0.92^{(a)}$
h_v (eV)	$0.75^{(a)}$ $0.56\pm0.04^{(b)}$	$0.55^{(a)}$

Table 3.2. Defect properties of ionic conductors CaF_2 and BaF_2 ((a) from Ref. [1973Boll1] and [1973Boll2] and (b) from Ref. [1968Bars1] and [1968Bars2]).

where h_F formation enthalpy of the anti-Frenkel defects, h_i activation enthalpy of the mobility of the interstitial fluorine ions, and h_v activation enthalpy of the mobility of the fluorine ion vacancies. (1eV is equivalent to 96.5kJ/mol)

3.2. Basic Defect Structures

3.2.1. Intrinsic Region

The alkaline-earth fluorides CaF_2 and BaF_2 are very similar and both show an anion-Frenkel disorder (also called anti-Frenkel disorder). This mode of disorder involves the displacement of lattice anions (here the F^- fluorine anions are small enough) to the interstitial sites (Figure 3.2). This leads to formation of anion vacancies and interstitial anions with anion transport occurring via the migration of these defects.

In the structure element notation this reads:

$$F_F + V_i \rightleftharpoons F_i^{'} + V_F^{\bullet} \qquad (3.1)$$

with the mass action law:

$$\left[F_i^{'}\right]\left[V_F^{\bullet}\right] = K_{\bar{F}}\left(T\right) = \exp\frac{\Delta_{\bar{F}}S_m^0}{R}\exp-\frac{\Delta_{\bar{F}}H_m^0}{RT} \qquad (3.2)$$

where: $\Delta_{\bar{F}}S_m^0$ formation entropy of anti-Frenkel defects (in units of R), $\Delta_{\bar{F}}H_m^0$ formation enthalpy (in kJ/mol), T temperature, $\left[F_i^{'}\right]$ concentration of interstitial ions, $\left[V_F^{\bullet}\right]$ concentration of vacancies, and $K_{\bar{F}}\left(T\right)$ is the Frenkel constant.

And, thus, the electrical conductivity in the intrinsic region ($\left[F_i^{'}\right] = \left[V_F^{\bullet}\right] = \sqrt{K_{\bar{F}}\left(T\right)} = n_{\bar{F}}$) is taken to be:

$$\sigma = e n_{\bar{F}}(u_i + u_v) \qquad (3.3)$$

where: *e* is the elementary charge (e=1.6022x10^{-19}C), u_i and u_v are the mobility of the interstitial fluorine ions and, respectively, of the fluorine vacancies.

These large interstitial sites in the fluorine structure determine a relatively low energy for the creation of anion interstitials. In contrast, the levels of cation disorder in these alkaline-earth fluorides are low and an important consequence is that the rates of cation diffusion, which are affected by cationic defects, are low.

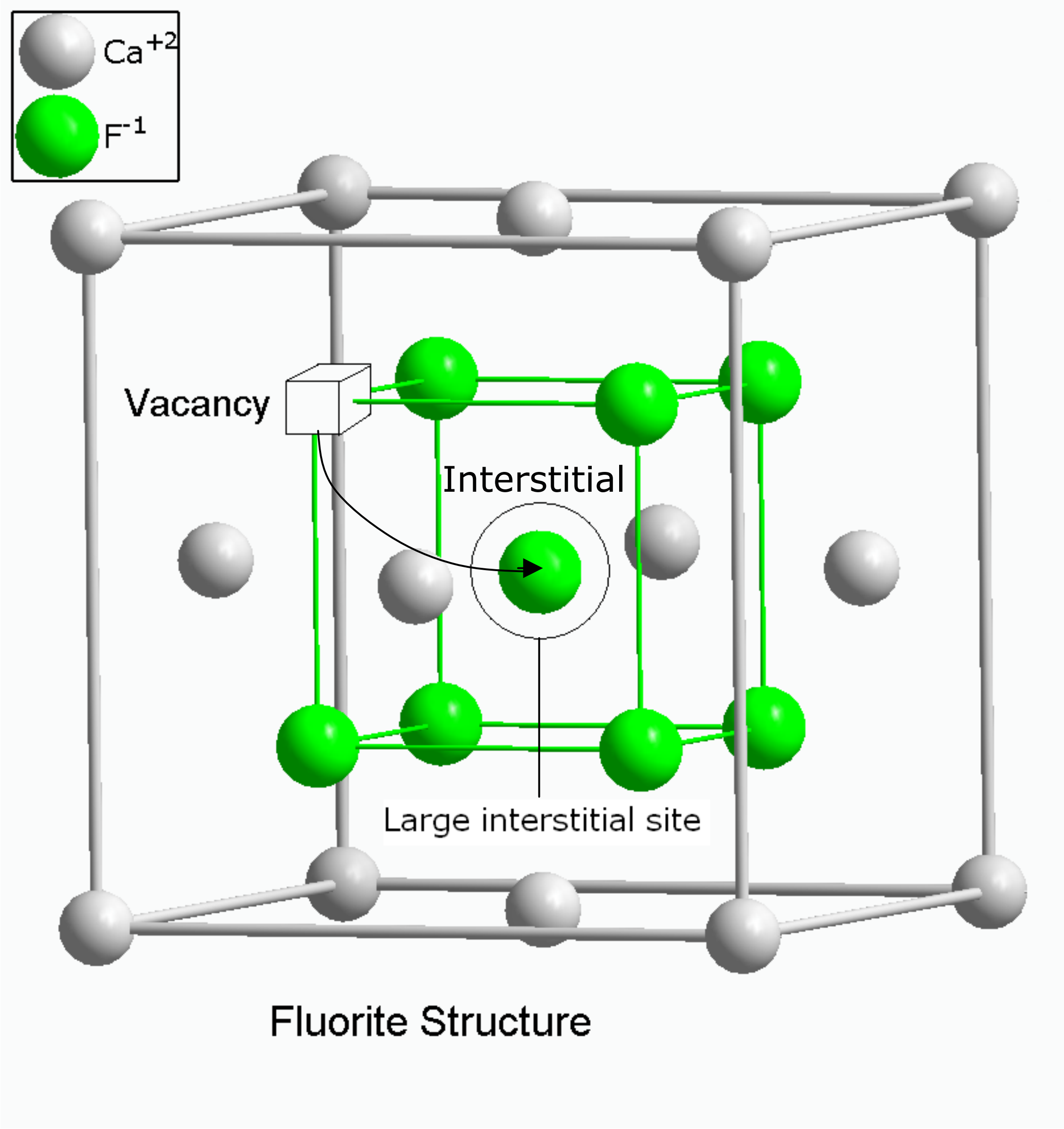

Figure 3.2. The formation of anti-Frenkel defects in a fluorite structure by movement of F^- to interstitial site and leaving behind a vacancy.

Transport properties in ionic conductors, both conductivity and diffusion, are determined by the migration of point defects (which correspond to deviations from the perfect translational periodicity of the solid). Therefore, the thermodynamic and kinetic behaviours of these materials are influenced by their defect structure.

From analysis of transport data (from measurements of conductivity or diffusion) the defect structure can be deduced, due to the fact that the conductivity and diffusion are controlled by both the concentration and mobility of defects.

Table 3.2 summarizes the nature and energetics of intrinsic disorder in CaF_2 and BaF_2 ionic conductors.

Numerous experimental investigations, involving static techniques such as optical spectroscopy as well as dynamic techniques such as electrical conductivity, thermal depolarization, dielectric relaxation, nuclear magnetic resonance (^{19}F NMR) have been used for studying ion conductors CaF_2 and BaF_2. The static methods provide information about the nature and site symmetry of the defects, whereas the dynamic ones measure properties such as diffusion constant and activation energy. The structural and transport properties were investigated also by computer simulation methods.

The results obtained by these techniques are far from being identical. In this study the values given in Table 3.2 were assumed to be the most reliable one.

3.2.2. Extrinsic Region

In addition to the intrinsic anti-Frenkel disorder, defects can also be created as "charge compensators" for impurity ions with a charge that is different from that of the host-lattice for which they substitute. For example, the replacement of Ca^{2+} or Ba^{2+} by a single charged cation (with a concentration C) leads to the increase in concentration of charge-compensating negative fluoride interstitials, while the concentrations of positively charged vacancies are reduced. The opposite occurs for negatively charged impurities.

At low temperatures, defects induced by single charged impurities dominate the defect concentration and hence the transport properties of the material, whereas at higher temperatures the intrinsic behaviour became predominant.

The impurities are incorporated at temperatures (above the melting point during the preparation of single crystal or for thin films due to the contamination of the equipment) that are higher than the measurement temperatures at which the foreign atoms are then immobile. In this case there are no compensation effects for the mobile defects, but overall electroneutrality is preserved, as follow:

$$\left[F_i^{'}\right] = \left[V_F^{\bullet}\right] + C \tag{3.4}$$

From Eq. (3.4) and Eq. (3.2) a new quadratic equation is obtained:

$$\left(\left[V_F^{\bullet}\right]+C\right)\left[V_F^{\bullet}\right]=K_{\bar{F}}\left(T\right) \tag{3.5}$$

with the solutions:

$$\left[V_F^{\bullet}\right]=-C/2+\sqrt{C^2/4+K_{\bar{F}}} \tag{3.6a}$$

$$\left[F_i^{'}\right]=C/2+\sqrt{C^2/4+K_{\bar{F}}} \tag{3.6b}$$

The extrinsic conductivity is given by:

$$\sigma/F=u_i\left(C/2+\sqrt{C^2/4+K_{\bar{F}}}\right)+u_v\left(-C/2+\sqrt{C^2/4+K_{\bar{F}}}\right) \tag{3.7}$$

From Eq.3.7 two extreme cases can be discussed:

1. $\sqrt{K_{\bar{F}}\left(T\right)}\ll C/2$. This case corresponds to an extrinsic material with high impurity content. In this case the concentration of fluorine interstitial ions is at the same level as the concentration of impurity, $\left[F_i^{'}\right]=C$ while the concentration of fluorine vacancies is much lower, $\left[V_F^{\bullet}\right]\ll\left[F_i^{'}\right]$, and, thus, can be neglected.

2. $\sqrt{K_{\bar{F}}\left(T\right)}\gg C/2$ in which the material can be considered intrinsic.

Chapter 4

Growth Processes and Experimental Setup

The question of the relative role of kinetics and thermodynamics in modern epitaxial growth techniques is of principal importance, to understand the control of composition, point-defect concentration and growth-rate. It plays an important role in optimizing the growth parameters as well as obtaining high-quality structures with planar or periodically modulated interfaces, highly defined geometry, and layer sequence.

4.1. Growth Processes

One of the classical methods of preparing a clean surface in UHV is evaporation and condensation of thin films. Depending on the surface and on the evaporation conditions, sublimed films can be polycrystalline or monocrystalline.

4.1.1. Thermodynamics of Growth

The thermodynamic classification of growth modes divides the film morphology into three classes determined by the balance of interfacial and surface free energies. It was noted that growth modes of thin films could be considered as a wetting problem, which was determined by:

$$\Delta\varepsilon = \varepsilon_f + \varepsilon_i - \varepsilon_s$$

where ε_s, ε_f and ε_i are the free surface energies of the substrate, the growing film and the interface energy, respectively. (More accurately one should use surface tensions.) This equation gives a formal distinction of the three growth modes depending on the sign of $\Delta\varepsilon$.

There are three main modes of epitaxial growth: (a) monolayer, (b) nucleated and (c) monolayer followed by nucleation.

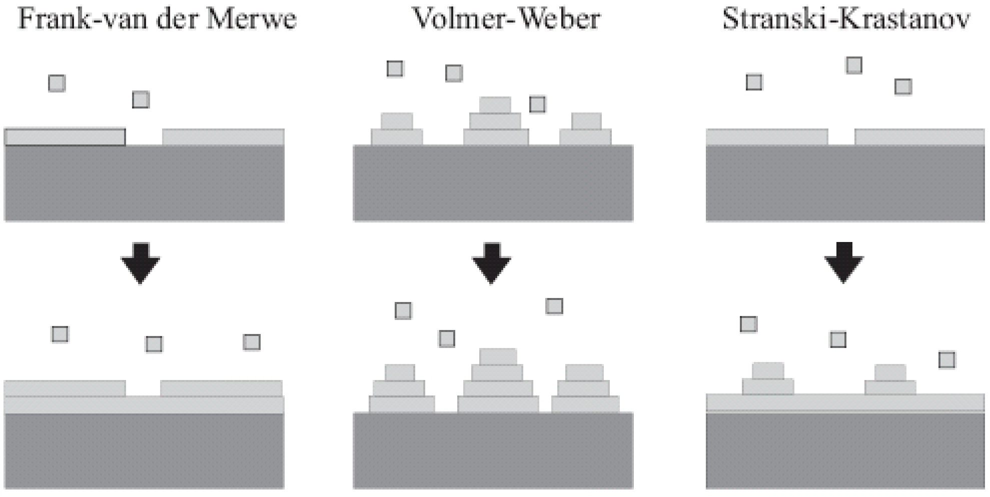

(a) **(b)** **(c)**

Figure 4.1.1. Schematic representation of the three thermodynamic growth modes.

The first mode is called Frank-van der Merwe (FM) or two-dimensional (2D) growth (Figure 4.1.1a) [1949Merwe]. In this mode, each layer tends to be completed before a new layer begins to grow on top of it. Monolayer growth occurs when the deposited atoms are more strongly bound to the substrate than they are to each other. The atoms aggregate to form monolayer islands of deposit which enlarge and eventually one complete monolayer coverage has taken place. The process is repeated for subsequent layer growth. For this reason the FM mode is also called *layer-by-layer* growth. In terms of static thermodynamics, it occurs when $\Delta\varepsilon \leq 0$, i.e. "wetting" of the surface by the deposited film takes place.

The opposite case is called the Volmer-Weber (VW) or three-dimensional (3D) growth (see Figure 4.1.1b) [1926Volmer]. In case of nucleated growth, the initial deposit atoms aggregate as small three-dimensional (3D) islands which increase in size as further deposition continues until they touch and intergrowth to form a continuous film. This mode is favoured where the forces of attraction between the deposited atoms are greater than that between them and the substrate. In this case the "wetting" condition is no longer fulfilled $(\Delta\varepsilon \geq 0)$.

The third, intermediate mode arises if the first few monolayers satisfy the layer-by-layer condition and the VW condition applies to all subsequent layers. This is called the Stranski-Krastanov mode (Figure 4.1.1c) [1938Stra]. This situation arises only in heteroepitaxy if a lattice mismatch between the substrate and the deposit material causes the growing layers to be strained. In such a case, it is often energetically favourable for the first few layers to grow in the layer-by-layer fashion, but after that, the strain is relieved more efficiently by the 3D mode.

4.1.2. Kinetics of Atomic Processes

In the kinetic picture, based on atomistic models, the growth mode is a complex balance of many competing processes, which are sketched schematically in Figure 4.1.2.1. The film morphology, as the outcome of this competition, is strongly influenced by the experimental conditions, i.e. the surface temperature and symmetry, the flux of adatoms impinging on the surface (deposition rate) and the choice of material. Each of the atomic processes is characterized by an activation energy and a prefactor. At a given temperature and deposition rate certain processes might be kinetically inhibited, whereas others are rate determined. Arrhenius-type exponential laws describe mathematically these activated processes. The basic atomic processes taking place during growth are: *deposition*, *surface diffusion* and *desorption*. A process competing with the deposition is the desorption. The desorption probability depends on two factors, the energy barrier necessary for the atom to overcome in order to leave the surface and the temperature T.

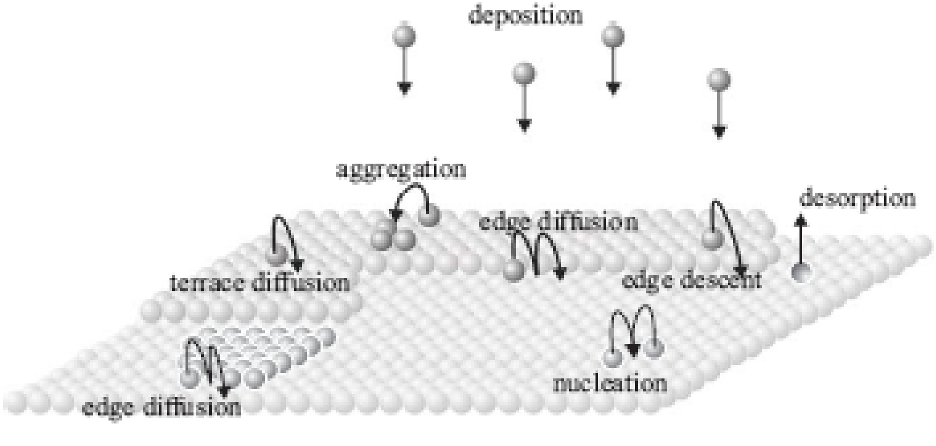

Figure 4.1.2.1. Atomic processes in the kinetics of 2-D film growth

The desorption rate increases if the temperature is increased, eventually reaching a point where the surface atoms begin to evaporate. Under MBE growth conditions that produce quality crystals, the desorption frequency is usually very low compared to the deposition rate, and it can therefore be treated as negligible [1995Bara].

The adatoms move on the surface by diffusion events, such as terrace, interlayer and edge-diffusion [2000Meiw]. These atomic events are thermally activated and their rates depend on the local surroundings and can usually be described by Boltzmann statistics. Once adsorbed, the atoms move across the surface depending on their diffusion coefficient.

If defects are present on the surface, the adatoms may be trapped at these sites forming nuclei for subsequent growth process, which is called heterogeneous nucleation. The other case is homogeneous nucleation where a stable nucleus is generated by more or less statistical aggregation of several (at least two) adatoms on regular sites. By addition of further adatoms, these nuclei will then grow. In contrast, islands up to that size can dissolve again.

When an adatom, wandering on a terrace, reaches a descending step, it encounters an additional energy barrier for hopping down the step known as the Erlich-Schwoebel (ES) barrier [1995Bara]. This is due to the fact that the adatom is more weakly bound to the substrate atoms when it is at the upper step edge. A modification to this picture has also been proposed. In this model, there is also a barrier for hopping upwards and the descending step barrier is encountered slightly before the adatom reaches the actual edge. The edge, therefore, acts reflectively towards atoms approaching from above. This effect is also known as diffusion bias.

In far-from-equilibrium growth the growth mode usually changes from 3D growth at low temperatures to layer-by-layer at higher temperatures. At low temperatures the local energy barriers at step edges prevent the surface adatoms from jumping down a step. At higher temperatures the surface adatoms become so mobile that they can overcome these barriers and the film grows according to the two-dimensional mode. Larger lattice mismatches generally favor island-like growth, and higher deposition rates, on the other hand, lead to a greater tendency towards layer-like growth. Under certain conditions, when the adatoms are mobile but the barriers at step edges suppress the inter-layer transport, the growth results in the creation of large, ordered, pyramid-like formations on the surface. This is called the unstable MBE growth mode. It was first detected by Villain in 1991 [1991Villa].

Using the MBE technique to prepare thin films, some basic models and principles turned out to be very useful in predicting and understanding epitaxial growth modes and film structures.

Supersaturation and Forced Layer Growth

Because of the high supersaturation of the condensing atomic beam, the real growth process is determined to a large extent by kinetic principles. For epitaxial and polycrystalline films, generally, by condensation at low temperature result small grain sizes, while by condensation at high temperatures leads to large grains. Accordingly, monolayer nucleation can be induced by high supersaturation (low temperature, high growth rate), resulting in a quasi van der Merwe or forced layer growth mode, which enable one to produce more or less layer by layer grown epitaxial films, even in nonwetting systems near the wetting limit.

Misfit and Misfit Dislocations

The lattice misfit f is a very important parameter to determine epitaxial growth. In a one-dimensional model it is defined by

$$f = \frac{b - a}{a}$$

where b and a are the lattice parameters of films and substrates, respectively. If the contacting lattice planes of both crystals show the same two-dimensional symmetry (homosymmetric interfaces), this definition also applies for interface. In the growing film the misfit to the substrate can be accommodated by elastic strain or by misfit dislocations. For small misfit, it may be energetically favourable for the film to accommodate completely to the substrate by elastic strain, forming a pseudomorphic film without any dislocations. There is a critical misfit, below which the monolayer is pseudomorphic. In general its order is about 10%.

For $f < 0$ the film is under expansive strain and the critical misfit becomes larger. While for $f > 0$ the film is under compressive strain and the critical misfit becomes smaller.

In particular, the heterolayers of CaF_2/BaF_2 have a lattice mismatch around 14% and leads to dislocations at the interface. These dislocations form already during growth of the first or second monolayer.

4.2. Experimental Setup

4.2.1. Deposition Method: Molecular Beam Epitaxy (MBE)

Molecular beam epitaxy (MBE) was developed in the early 1970s as a means of growing high-purity epitaxial layers of compound semiconductors [1971Cho],[1975Cho]. Since that time it has evolved into a popular technique for growing various compound semiconductors materials, as well as several other materials (metals, oxides …). Among the different crystal growth techniques, molecular beam epitaxy (MBE) represents the best one in order to grow metastable, very thin and highly controlled epitaxial layers.

The word "epitaxy" is derived from Greek meaning "arrangement on" and therefore a film of material deposited upon a crystalline substrate is said "epitaxial" if it repeats the crystallographic structure of the substrate.

Epitaxy refers to the ordered growth of one crystal upon another crystal. Because of the large range of possible compounds and their alloys, it is rare in device fabrication to grow bulk crystals of all these materials. Instead, it is more attractive to realize the wider range of materials by epitaxial growth. This is partly due to the difficulties involved in developing easy bulk crystal growth techniques for each new material and also because of historical reasons.

MBE can produce high-quality layers with very abrupt interfaces and good control of thickness, doping, and composition. Because of the high degree of control possible with MBE, it is a valuable tool in the development of sophisticated electronic and optoelectronic devices. Using MBE allows one to prepare thin crystalline films on crystalline substrates under ultrahigh vacuum (UHV) conditions. The first ion conductor heterolayers were prepared by Sata et al. [2000Sata].

In this chapter we discuss MBE growth of CaF_2 and BaF_2 layers necessary for understanding of ionic conductivity. In particular, we use the MBE technique to realize the heterolayers of CaF_2/Baf_2 on various substrates (Al_2O_3, Si, Nb-doped $SrTiO_3$) and different orientation of the substrates, epitaxial grown films whose thickness and elemental composition can be varied within a very few atomic layers. The interfaces are artificially tuned, with the aim of understanding the effects of the overall ion conduction.

Basic Principles of MBE

Using the MBE technique to prepare thin films, some basic models and principles turned out to be very useful in predicting and understanding epitaxial growth modes and film structures.

The molecular beam condition (where the free path of the particle is larger than the geometrical size of the chamber) is ensured for typical distances between the sources and the substrate, if the total pressure does not exceed 10^{-4} mbar. However, all MBE systems are provided with a means of reaching and maintaining an ultrahigh vacuum (around 10^{-10} mbar) and the operation is usually oil-free. One of the reasons why MBE systems have to be oil-free is the need to ensure that the substrate is atomically clean before growth. An ultrahigh vacuum (UHV) is essential for growing high-quality films, but it is not a sufficient condition; two other conditions need to be applied.

First, the internal pressure results from competition between the rate of gas evolution and the rate of pumping, so that is necessary to use construction and crucible materials with the lowest rate of gas evolution. The crucible material used for deposition is boron nitride for BaF_2 and graphite for CaF_2; witch combines a low rate of gases evolution with weak chemical activity in the range of temperature less than 1500°C.

Second, it is important to ensure cryogenic screening around the substrate so as to minimize stray fluxes of atoms and molecules from the walls of the chamber, which are at the room temperature, and from the heated components of the apparatus.

4.2.2. Substrate Preparation

A clean substrate surface is an important prerequisite for epitaxial growth, since contaminants from the atmosphere or other sources can easily contaminate the sources of CaF_2 or BaF_2 and cause crystal defects or degrade the electrical characteristics of the epitaxial layer.

The mounted substrates on the molybdenum block are put into the loading chamber and kept in high vacuum for several hours to outgas before moving them into the deposition chamber.

The substrates are outgassed again in the main chamber at different temperatures (depending on the type of substrates) before starting the deposition. This handling will result in some dust on the wafer surface that will produce defects, but with proper care, the amount of dust can be reduced.

The substrate temperature is ramped up, and is monitored using a spring-loaded thermocouple in vicinity of the molybdenum holder The system has a window facing the sample, then an optical pyrometer can be used to measure the real temperature of the substrate.

Materials and Orientation

The heterolayers of CaF_2/BaF_2 with different interfacial spacings and number of interfaces has been prepared on different substrates: Al_2O_3 (012), Si (111), Nb-doped $SrTiO_3$ (100) These two materials were chosen due to some advantages:

1. Sapphire Substrate

It has been shown that the ionic conductivity of CaF_2/BaF_2 heterolayers was dominated by interfacial effects and characterized by high conductivity values, particularly if the interfacial spacing is in the sub-Debye range [2000Sata]. The excess conductivity caused by the CaF_2/BaF_2 interface does not depend upon the orientation of the films or the substrate [2004Guo2]. The substrate itself causes a space charge effect which adds to the overall conductance as a constant contribution and is of the order of the effect of a single CaF_2/BaF_2 interface (or less), and hence totally negligible if the number of CaF_2/BaF_2 interfaces is high.

It was also found that the heterolayers grown on Al_2O_3 (012) exhibit a maximum interfacial concentration while the other heterolayers (grown on another Al_2O_3 orientation or MgO substrates) show distinctly smaller values (at 300°C, e.g. the concentration at the Al_2O_3 (006) substrate is smaller by one order of magnitude) [2004Guo1].

Now we are in the position to choose the substrate for further depositions. From now on all the heterolayers for parallel measurement have been prepared only on Al_2O_3 (012) substrate (CrysTec Kristalltechnologie, Germany) and the BaF_2 was the first deposited layer because growth occurs exclusively in (111) direction and can be obtained very tiny films with very smooth and continuous surface.

2. Silicon Substrate

The growth of single crystal insulating films on semiconductors is of interest for a number of reasons, including use as gate insulators or as a buffer layer for overgrowth with different semiconductor films, and because of interesting structural and electronic properties of the ionic/covalent interface.

In this study the (111) oriented Si substrates (Wacker-Chemitronic GmbH) were used due to the fact that films grown are of better quality than other oriented substrate, presumably due to the lower surface energy of this orientation [1984RWF]. At room temperature the lattice constant of CaF_2 is only 0.6% higher than that of Si (111), while that of BaF_2 is 14% higher. The substrate surface is (111) oriented with an accuracy better than 0.5°.

The fluorite crystal structure is very similar to the structure of Si, potentially allow epitaxial growth for (111) substrate orientation. However, the thermal expansion coefficients of the fluorides are about 7 times larger than in Si and the lattice mismatch between CaF_2 and Si is as high as 2.4% at 750°C, a typical growth temperature in MBE.

3. $SrTiO_3$ Conductive Substrate

The 0.5 wt% Nb-doped $SrTiO_3$ (100) substrates (STO:Nb) were used due to the fact that this material have very low resistivity compared to CaF_2 or BaF_2, and it can be used as the counter electrode for the perpendicular measurements. To ensure that we obtain a good electrical contact one side of the substrate was covered by Cr/Au.

Cleaning Procedure

The surface preparation of the substrates differs, and different cleaning procedures before loading substrates into the vacuum are necessary. For this chemical and thermal cleaning were performed. This section will discuss the parts of the procedure which are different:

1. The sapphire substrates Al_2O_3 (012) were optically polished on one side and coated with Ti films on the other to stabilize and homogenize the temperature.

Prior to the deposition, the substrates were cleaned with acetone in ultrasonic bath for 10 min. at room temperature, dried in nitrogen inert atmosphere and mounted in the loading chamber. After reaching a good vacuum the substrates are transferred into the growth chamber and moved to face the sources. The samples temperature is increased at 400°C for out gassing and kept for several hours in order to remove all traces of oxygen or organic impurities from the surface.

After this treatment the substrate temperature is increased until the deposition temperature and the deposition of CaF_2 or BaF_2 has been started.

The same procedure of cleaning was used for STO:Nb substrates.

2. The p^+-type (0.003–0.005 Ωcm, B-doped) and n^+-type (0.0046-0.0057 Ωcm, P-doped) (111) oriented Si substrates with offcut angles less than 0.5° and one side polished were used. Before cleaning all the Si substrates were coated with Au films on the unpolished side in order to obtain a good contact for the electrical measurements.

Then, the substrates are chemically cleaned using a modified RCA process developed by *Ishizaka et al.*[1982Ish], which leaves a thin protective oxide on the surfaces. After that the samples were cleaned with deionised water followed by dipping in a hydrofluoric acid (HF) solution for surface passivation. The Si (111) substrates are then immediately introduced in the loading chamber and outgassed for 1 h before loading into the growth chamber. No carbon traces were observed after the hydrogen-passivated layer was desorbed from the Si surface at the temperatures of 500°C. Prior to growth, inside the ultra high vacuum (UHV) system, Si (111) surfaces are cleaned by annealing the substrates at 950°C for 10 min., in order to remove the protective oxide layer and evaporate contaminants from the surface.

All the chemicals used in the cleaning procedure were VLSI Selectipur.

4.2.3. Experimental Setup of the MBE Chamber

In this work a stationary MBE chamber was used to prepare the CaF_2/BaF_2 heterolayers. The growth chamber of the MBE system and several of its subsystems are schematic illustrated in Figure 4.2.3.1, while in Figure 4.2.3.2 a short presentation of the effusion cell mounted in system is shown.

The MBE system consists of two main vacuum chambers: a growth chamber and a load lock chamber. The loading chamber is used to bring samples into and out of the vacuum environment while maintaining the vacuum integrity of the other chambers machine without opening the main chamber to air. Substrates are loaded onto the growth chamber via a magnetically coupled transfer rod located in transport tube. The sample holder is positioned so that the substrate faces the material sources.

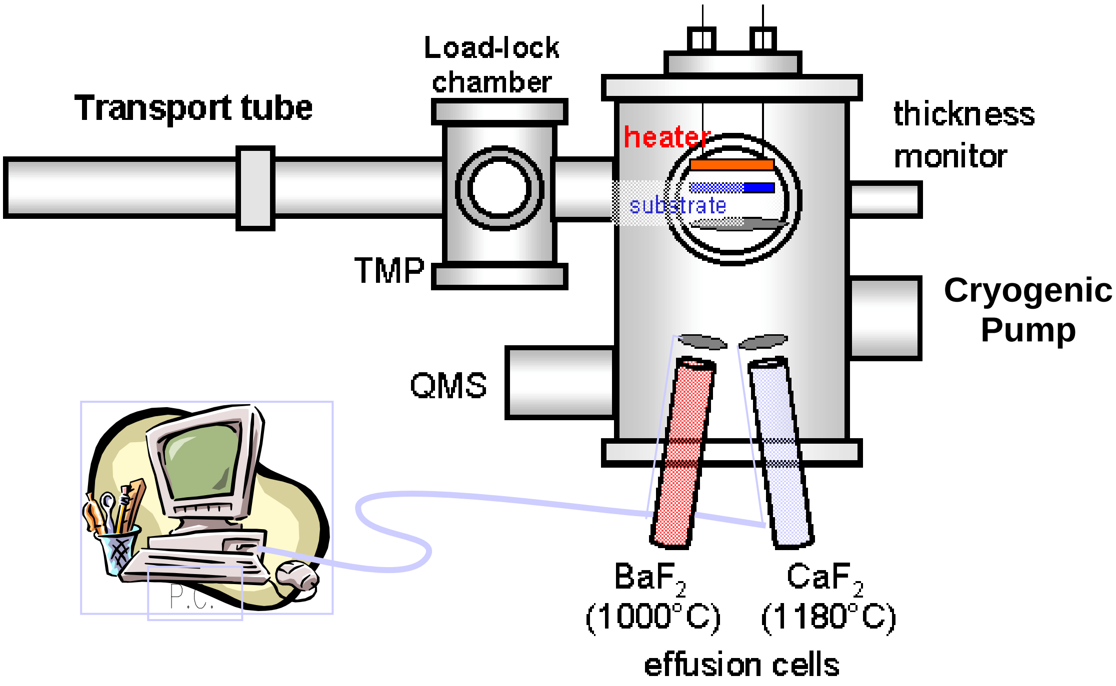

Figure 4.2.3.1. Diagram of the MBE system growth chamber

The chambers are pumped in series with turbo-molecular pumps (TMP, Varian Turbo-V 70LP), which is prepumped by a rotary pump.

Additionally a cryogenic pump (Cryo-Torr High Vacuum Pump, CTI-Cryogenics) is used, in order to achieve an ultrahigh vacuum. The cryopump consists of a cold head which is cooled to 15K by means of a closed cycle He refrigeration system. At the low temperature of around 15K most gases (e.g. O_2, N_2, CO_2) condense at the cold head. This pumping arrangement can keep the partial pressure of undesired gases, to less than ~10^{-10} mbar.

The substrate holder provides a mechanical support of holding and transporting the substrate in and out of the MBE chamber. The material used is Mo which is characterized by a low pressure and little outgassing. All other parts that are heated are made of materials such as W, Ta, Mo, pyrolytic boron nitride (PBN), pyrolytic graphite (PGR) which do not decompose or outgas impurities even when heated to 1400ºC.

To monitor the residual gases, to analyze the source beams, and to check for leaks, a quadrupole mass spectrometer (QMS, Balzers Prisma) is mounted in the vicinity of effusions cells. The rate of evaporation is monitored by a calibrated quartz crystal thickness monitor. A shutter can be used to cover the substrate partly during the sample preparation. This is particularly useful for the preparation of wedge-shaped samples.

An important part of an MBE system is effusion cells which are used to evaporate the materials (in our case 2 effusion cells: one for CaF_2 and another for BaF_2). The effusion cells are designed in a geometry which allows much less frequent collisions between atoms of material than collisions between atoms and the crucible wall. As a result, the flux distribution of evaporated material from a cylindrical effusion cell is a jet-like and can be described by a cosine function.

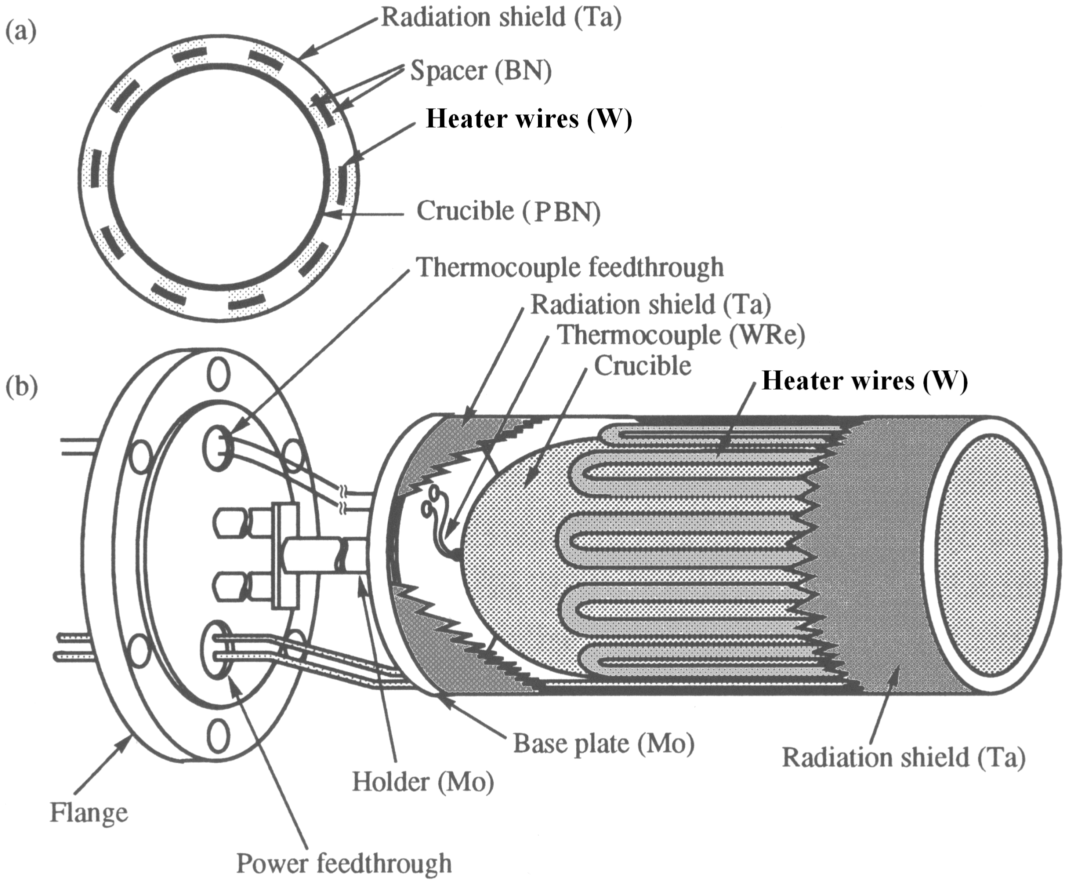

Figure 4.2.3.2. (a) Top view and (b) side view of an effusion cell with cylindrical pyrolytic boron nitride (PBN) crucible. The crucible is heated by W wires and heat-shielded by Ta foil. A thermocouple is used to measure the temperature of the crucible. The effusion cell is mounted on a contact flange with feedthroughs for the heater, the thermocouple and shutter [1993Schu].

A small diagram of an effusion cell mounted on a flange is shown in Figure 4.2.3.2.

The essential parts of such effusion cell are the crucible, heating wire, heat shield and thermocouple. In our MBE system, the crucible is made out of pyrolytic boron nitride (PBN) for BaF_2 deposition and of pyrolytic graphite (PGR) for CaF_2, both with cylindrically shape

The heater of the effusion cell consists of tungsten wire, mechanically kept in place by boron nitride spacers. Due to the low inductance of the heater filament the alternating current supplies is used and also reduce the magnetic field which would perturb the beam of evaporated material.

The effusions cells are independently heated until the desired material flux is achieved. The changes in the temperature of a cell as small as 0.5°C can lead to flux changes in the order of one percent. To control temperatures to about 1%, highly stable control loops with Tungsten-Rhenium thermocouples and proportion, integral, and derivative (PID) controllers are used. The material sources in the MBE system are located approximately 30 cm from the substrate in the growth position. In production systems, which are designed for larger wafers and greater uniformity, this distance is larger.

Computer controlled shutters are positioned in front of each of the effusion cells to be able to shutter the flux reaching the sample within a fraction of a second. Since shutters in front of the effusion cells reflect some of the power back into the cell, opening the shutters is known to cause flux transients on the order of a few percent. These transients are difficult to measure and depend on cell and system-specific factors such as the shutter type and location, heater element design, and thermocouple placement. As a result, the time required to open and to close a shutter must be much shorter than the time required for growing a monolayer of the material. This condition is required to grow sharp interfaces and very thin films.

4.2.4. X-Ray Diffraction (XRD) and Atomic Force Microscopy (AFM)

In order to understand growth processes and to get a better characterization of the films obtained, after deposition the samples were analysed by X-ray diffraction (XRD) and atomic force microscopy (AFM).

Conventional $2\theta-\theta$ scans were performed using the Cu K_α line for XRD and recorded by PHILIPS PW3710 XRD spectrometer. AFM was carried out on a TOPOMETRIX TMX2000 microscope operated in air.

AFM can produce high-resolution images of the surface of the sample. The tip-sample force in AFM is typically detected by measuring the bending of a flexible cantilever on which the tip is attached. As the tip approaches the sample surface, it first experiences log-range forces, such as van der Waals and electrostatic interactions, then specific bonds between the tip and the sample surface, followed by a rapid increase in the repulsive force. AFM can operate in either attractive or repulsive force modes. In the repulsive mode, or contact-mode AFM, the force is highly stable and images that show the periodic lattice structure of the samples are obtained.

The images can show perfectly ordered atomic structures or even defects that are much greater than an atom, when the net repulsive force applied on the sample surface by the tip is 0.1 nN or smaller.

Increasing the repulsive force, the contact area between the tip and the sample is much greater than an atom. The AFM images, nevertheless, still show well-ordered two-dimensional lattice structure owing to the periodic modulation of the force by the periodic lattice of the sample surface. The AFM experiments operated with a contact force much greater than 0.1 nN cannot truly exhibit atomic resolution.

In this study the AFM measurements were performed in air at the room temperature and the applied force on the tip was of order 2 nN.

4.2.5. Experimental Setup for Electrical Measurements

For parallel measurements the conductivity was determined by a.c. impedance spectroscopy at different temperatures, under constant flow of Argon as shown schematically in Figure 4.2.5.1. The impedance analyzer used to measure the impedance of the samples with frequencies ranging from 10^{-1} to 10^{7} Hz was Novocontrol Alpha-A high dielectric analyser.

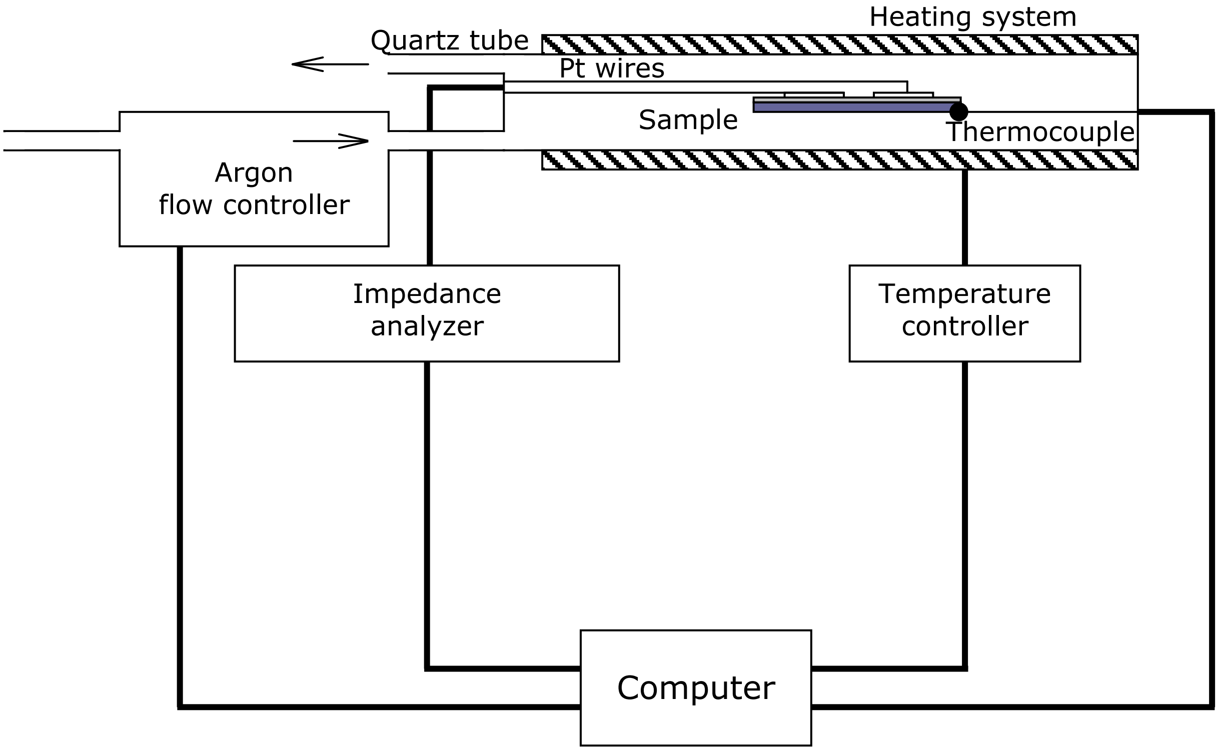

Figure 4.2.5.1. Schematic drawing of the setup used for the parallel measurements.

In Figure 4.2.5.1 is schematically represented the setup used for parallel measurements. The temperature controller for the heating system was Eurotherm 2416, and to control the flow of Ar (99,995% purity) in the quartz tube a Aera ROD-4 flow controller has been used. In order to measure with accuracy and better control the temperature in system a NiCr-Ni thermocouple was attached to the back side of the sample.

For the perpendicular measurements a tungsten probe tip in connection with a micromanipulator was combined with an impedance analyzer for the impedance measurements, which were carried out at varied temperatures under an argon atmosphere. The schematic diagram of the measurement setup is shown in Figure 4.2.5.2.

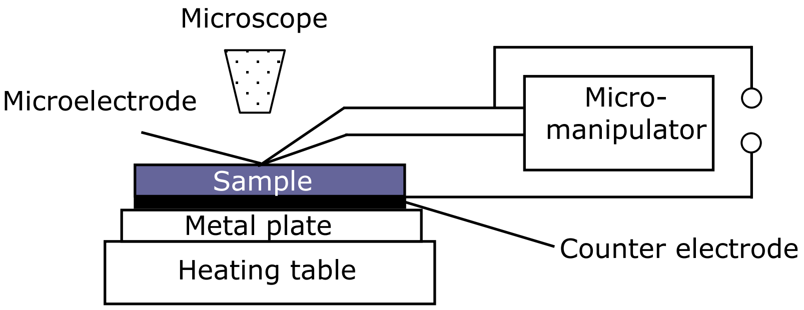

Figure 4.2.5.2. Schematic setup for perpendicular measurement.

Using the proper equivalent circuit for each type of measurement, the resistance of the heterolayers is obtained and converted to the conductivity (σ_m).

4.2.6. Impedance Spectroscopy in Solid State Electrochemistry

Impedance spectroscopy is a powerful method to characterise the electrical properties of materials and interfaces [1987Mac]. In solid state electrochemistry, one typically encounters situations where the electrical response of a system is determined by several single processes. In a galvanic cell, for example, both the electrodes and the electrolyte contribute to the total resistance. In case of a polycrystalline electrolyte, the electrolyte resistance comprises bulk and grain boundary contributions, and the electrode resistances may be caused by bulk as well as interfacial effects. In a conventional, stationary two-electrode d.c. measurement, one only obtains the overall sample resistance, i.e. the sum over all these individual processes. In a four-electrode arrangement, the use of different electrodes for current supply and voltage measurement can eliminate the influence of the electrodes. More detailed information on the electrical properties of a system is generally provided by a frequency dependent measurement of the a.c. resistance. In an impedance spectroscopy experiment, a small, alternating electrical signal is applied to the sample, and its response (the resulting current or voltage) is measured. By varying the frequency, ω, over several orders of magnitude, one can in many cases distinguish individual resistive processes due to differences in their relaxation times. The time required for a polarised region to equilibrate after an electrical perturbation is characteristic for the specific electrochemical process, and given that the relaxation times (or frequencies) of two processes are sufficiently different they can be separately measured by impedance spectroscopy. The latter condition is often fulfilled in solid state electrochemistry, since the relevant characteristic relaxation times (e.g. for electrode processes as compared to transport across grain boundaries) typically differ by several orders of magnitude. Even if a separation is initially not possible, one can often shift the relaxation frequencies in a favorable way by varying the experimental conditions.

The potential of impedance spectroscopy in the field of solid state ionics was realized after Bauerle [1969Bau] had demonstrated in 1969 that the technique can differentiate between bulk, grain boundary and electrode resistances. Today, impedance spectroscopy is probably the most important tool for investigating electrical transport and electrochemical properties of ionic solids [2002Fle]. To display experimental impedance data, different kinds of plots based on impedance Z ,admittance Z^{-1}, modulus iω Z or complex capacitance (iω Z)$^{-1}$ are used. Most common in solid state ionics are representations in the complex impedance plane (imaginary vs. real part of Z , often referred to as Cole-Cole plot) and Bode-plots (log(Z_{real}) or log(Z_{imag}) vs. log(ω)).

The interpretation of measured impedance spectra may be simple to extremely difficult, depending on the complexity of the investigated system. The most popular approach is based on constructing an electrical network representation, a so-called equivalent circuit. Such a network model, which may consist of resistors R, capacitors C and other elements, has to approximate the measured Z (ω) well over the whole frequency range. The simplest case is a single RC-element, i.e. one resistor and one capacitor in parallel, with impedance:

$$\bar{Z}_{RC} = \frac{R}{1 + i\omega RC} \tag{4.1}$$

In the complex impedance plane, such impedance yields a semicircle with diameter R (Fig.4.2.6.1a). It is clear that in the limit $\omega \to 0$ the influence of the capacitance has to vanish, and the d.c. resistance R is obtained. At higher frequencies, the real part of the impedance Z_{real} decreases due to the dielectric "opening" of the capacitance (displacement current), whereas the imaginary part Z_{imag} (or the phase shift between the currents going through the resistor and the capacitor) increases. The frequency where these two currents are equal and the imaginary part of the impedance reaches its maximum is the relaxation frequency, ωR, of the RC element. It is given by:

$$\omega_R = \frac{1}{RC} \tag{4.2}$$

Two serial RC elements lead to two well-separated semicircles in the complex impedance plane if their relaxation frequencies are sufficiently different (Fig.4.2.6.1b). In a real system, this may for example be realized by a large difference in the magnitude of the capacitances and similar values for the resistances. Hence, if a measurement yields one or several well-separated semicircles, the resistances and relaxation frequencies of the underlying processes can immediately be read from the Cole-Cole plot, and thus a capacitance can be calculated for each process. The magnitude of a capacitance is often already a strong indication of its physical origin.

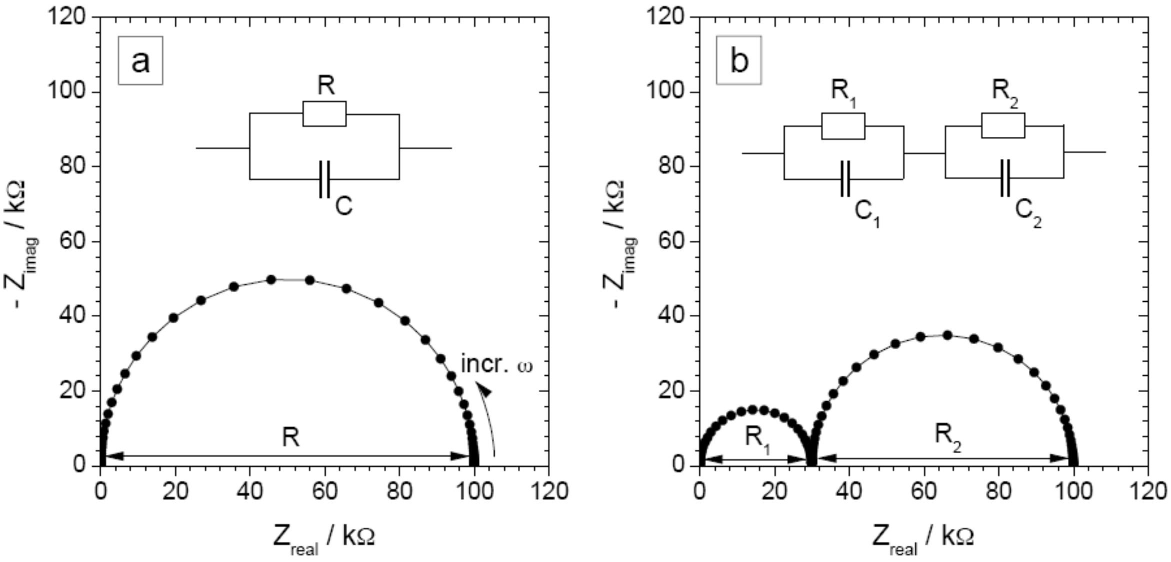

Fig.4.2.6.1. Simulated impedance spectra of one RC-element (a) and two serial RC elements with substantially different relaxation times (b); parameters: R = 100 kΩ, C = 1 µF; R_1 = 30 kΩ, R_2 = 70 kΩ, C_1 = 1 nF, C_2 = 10 µF; frequency range: 10^{-3} - 10^{6} Hz.

In many situations, however, the required equivalent circuit representation and thus the interpretation of impedance spectra is more complicated. Some of the difficulties frequently encountered when interpreting impedance spectra shall briefly be mentioned in the following:

Obviously, difficulties emerge if two serial processes have similar relaxation frequencies. In such a case the two semicircles overlap, and the resulting impedance behaviour may appear as a single, distorted arc in the complex impedance plane [2002Fle]. The decision on whether or not such a distorted semicircle consists of two components is aggravated by the empirical fact that experimental semicircles are always “non-ideal” to some degree, i.e. more or less depressed, even if they are caused by a “single” electrochemical process. Apparently, an RC element generally oversimplifies the real situation. A path frequently followed in order to deal with depressed semicircles is to replace the capacitor of an RC element by a so-called constant phase element Q, with impedance:

$$\bar{Z}_Q = \frac{1}{Q(i\omega)^n} \qquad (4.3)$$

A constant phase element may thus be regarded as a generalization of a capacitance, which takes account of the “non-ideality” of experimentally observed semicircles. The parameter n, a constant defined by Eq.(4.3), is essentially a measure of the degree of “depression” of such an arc. For n = 1, the constant phase element is identical to a capacitance, corresponding to a perfect semicircle in the Cole-Cole plot. For n < 1, one obtains more or less depressed arcs. By introducing constant phase elements one can often achieve an accurate fitting also for nonideal impedance arcs. From the fitting parameters Q and n, a capacitance C can then be calculated according to:

$$C = \left(R^{1-n}Q\right)^{1/n} \qquad (4.4)$$

It might be interesting to note that the impedance of an RQ element can be expressed as an integral over weighted RC elements [1941Cole],[1990Jam]

$$\bar{Z}_{RQ} = \int_{-\infty}^{\infty} \frac{R}{1 + i\omega RC(s)} F(s)ds \qquad (4.5)$$

with $C(s) = \left(R^{1-n}Q\right)^{1/n} e^s$ and

$F(s) = (2\pi)^{-1} \sin((1-n)\pi / s) / (\cosh(ns) - \cos((1-n)\pi / 2))$

The weight function F(s) has its maximum at s = 0, i.e. the capacitance of Eq.(4.4) corresponds to the RC element with the highest weight in the integral. Eq.(4.4) is therefore an approximation, which becomes more accurate as $n \to 1$.

Reviewing the literature in the field of solid state ionics, one finds that equivalent circuits are frequently proposed ‘ad hoc’ and tested in terms of their apparent agreement with the measured spectra. Intuitively, a good correspondence between experimental data and fit curve may then be taken as a confirmation that the proposed circuit provides a good description of the system under investigation. Such a course of action, however, may be problematic since even an excellent fit, i.e. very close agreement of experimental data and fit curve over a wide frequency range, is in general insufficient proof for the correctness of a model. The reason is that equivalent circuits are often not unique. Well-known are the cases where two (or more) physically different equivalent circuits are 'mathematically equivalent' in terms of their overall response, i.e. the same frequency dependence of the impedance $\overline{Z}(\omega) = Z_{real}(\omega) + iZ_{imag}(\omega)$ can be obtained with both circuits, however in general with different values for the individual circuit elements. An example is shown in Fig.6. Obviously, such a situation easily leads to misinterpretations. These last remarks are intended to show that great care has to be taken whenever interpretations of experimental impedance data are based on ad-hoc introduced equivalent circuits. It is always necessary to validate such interpretations by additional consistency checks, including a wide parameter variation, to see whether the dependence of the obtained fitting parameter values on experimental conditions is reasonable. Ideally, one finds a way to derive rather than postulate an equivalent circuit from a more general description.

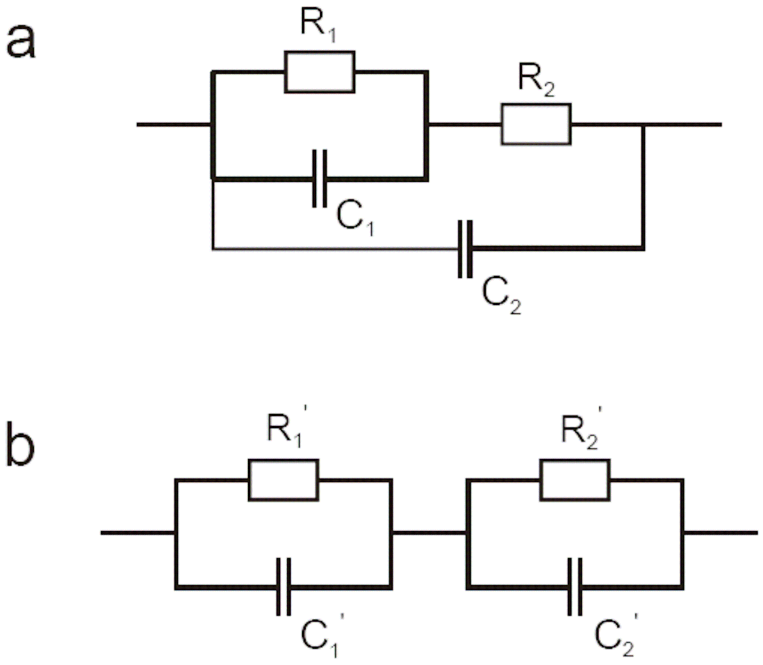

Fig.4.2.6.2. Example for two "mathematically equivalent" circuits

Chapter 5

Experimental Results

Different experimental investigations, involving static techniques such as optical spectroscopy as well as dynamic techniques such as electrical conductivity, thermal depolarization, dielectric relaxation, nuclear magnetic resonance (^{19}F NMR) have been used for studying ion conductors CaF_2 and BaF_2. The static methods provide information about the nature and site symmetry of the defects, whereas the dynamic ones measure properties such as diffusion constant and activation energy. The structural and transport properties were investigated also by computer simulation methods.

While the increase of the parallel conductivity of the CaF_2/BaF_2 heterolayers with periods larger than 50nm could be interpreted by semi-infinite space charges, the effects are more subtle when the individual layer thickness is less than 50nm. At such thickness, single layers lose their individuality and an artificial ionically conducting material with anomalous transport properties is generated [2006Jam]. The results demonstrate mesoscopic ion conductivity effect in nanosystems (extremely thin films, nanocrystalline materials). The origin of enhanced ionic conduction is not well understood, but an interfacial mechanism is clearly implied. As regards the space charge inducing mechanism two can apply: (i) a F^- transfer from one phase to the another; (ii) a charging of the interface of of other higher dimensional defects, such as dislocations.

The layer structure and the formation of extended crystal defects have strong influences on the density and the mobility of charge carriers in the multilayers that add to the purely chemical effects. In order to obtain more fundamental insight into conductivity effects, there are still some points to be clarified: (1) the detailed understanding of the mesoscopic situation; (2) the contribution of electronic carriers; (3) the annealing effects. To understand these effects in depth, electrical measurements were performed on parallel (along the interfaces) and perpendicular (to the interfaces) configuration of the heterostructures, and also measurements on single crystals.

5.1. Single Crystal Measurement

The purpose of this experiment is to study the ionic conductivity of fluorite-type crystals CaF_2 and BaF_2 and to determine the effective level of impurities. As the later is difficult to obtain otherwise, this is a natural parameter for fitting the experimental results obtained on thin films. The conductivity measurements were carried out on specimens who were cut from a part of single crystals commercially available with 99.999% purity (Crystal GmbH, Germany).

The samples were polished and cleaned in acetone by ultrasound bath. The thickness and surface area of the samples were 1 mm and 5x5 mm^2, respectively. On both sides of the samples Pt electrodes were deposited by d.c. sputtering at room temperature. The conductivity was determined by a.c. impedance spectroscopy at different temperatures between 610°C–100°C with frequencies from 1 to 10^7 Hz, under constant flow of Argon.

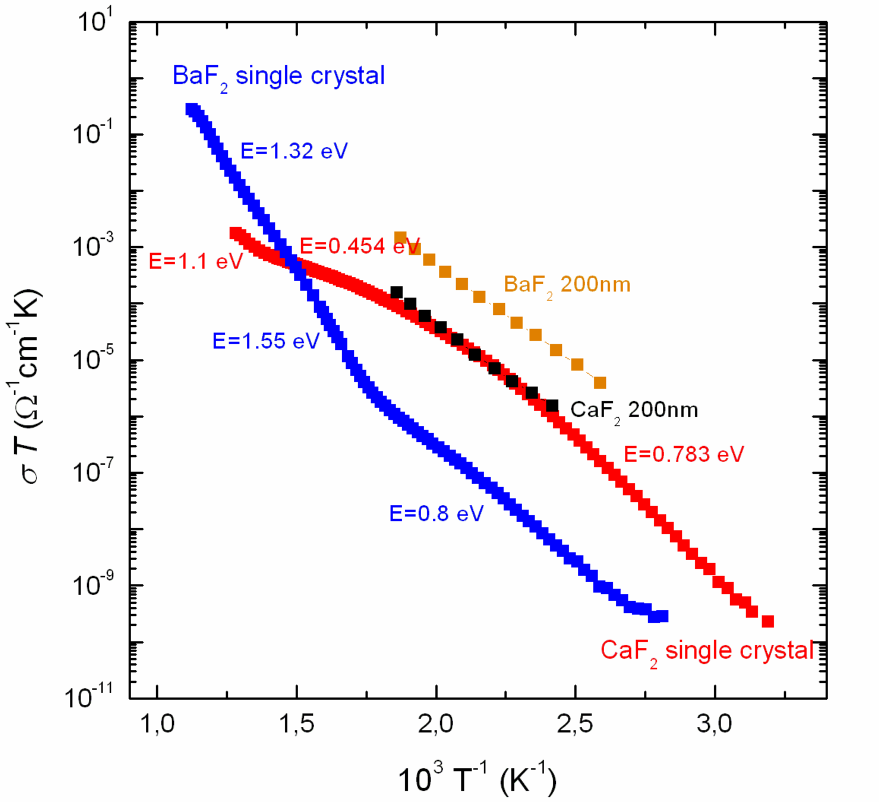

Figure 5.1.1. Arrhenius plots of the conductivity for single crystals of BaF_2 and CaF_2.

The specific electrical conductivity of CaF_2, and BaF_2 in the crystalline state is shown in Figure 5.1.1. For comparison the measured parallel conductivity of two thin films (200nm thickness) BaF_2 and, respectively, CaF_2, are also drawn.

In order to determine the concentration of impurities in extrinsic region the calculation uses published data on defect formation and mobility for BaF_2 from Ref. [1973Boll1], [1973Boll2], [1968Bars1] and [1968Bars2] and for CaF_2 from Ref. [1973Boll1] and [1973Boll2] as shown in Table 5.1. Both sets of the literature data were used in order to obtain the content of impurities and to make a comparation between them.

For both materials, BaF_2 or CaF_2, the major impurities can be assumed to be oxygen defects ($n = O_F^{'}$). This is a realistic assumption for the single crystals, but for the case of thin films, during preparation in main chamber of the MBE, other impurities can be incorporated as well. In this case the conductivity is given by:

$$\sigma = eu_v n_v + eu_i n_i$$

where n_v and n_i represent concentrations of fluorine ion vacancies and interstitial fluorine ions, respectively.

From the electroneutrality condition including $O_F^{'}$:

$$n_v = n_i + n$$

and from Frenkel relation:

$$n_v \cdot n_i = K_F$$

where K_F is the Frenkel constant.

The conductivity can now be written:

$$\sigma = e\left(u_v\left(n/2 + \sqrt{n^2/4 + K_F}\right) + u_i\left(-n/2 + \sqrt{n^2/4 + K_F}\right)\right)$$

Figure 5.1.2 shows that in the case of BaF_2 the fit using the data from Ref. [1973Boll1] and [1973Boll2] (blue curve) is almost perfect indicating a (singly charged) impurity content of 6.0×10^{16} cm^{-3}. Using the data from Ref. from Ref. [1968Bars1] and [1968Bars2] a good agreement with the measured conductivity is obtained. The differences can occur due to different values in the mobility of the carriers.

In the case of CaF_2 the fit is good only for the temperatures above 400°C (green curve in Fig. 5.1.3). Below 400°C impurity association may complicate the situation.

Compound	**BaF_2**	**CaF_2**
n_F (cm^{-3})	$2.56\text{x}10^{23}\exp\left(-\frac{9284}{T}\right)^{(a)}$ $7\text{x}10^{23}\exp\left(-\frac{10792}{T}\right)^{(b)}$	$2.56\text{x}10^{24}\exp\left(-\frac{14216}{T}\right)^{(a)}$
u_v ($cm^{-2}K/Vs$)	$\frac{1170}{T}\exp\left(-\frac{8704}{T}\right)^{(a)}$ $\frac{6.4\text{x}10^{2}}{T}\exp\left(-\frac{6498.5}{T}\right)^{(b)}$	$\frac{220}{T}\exp\left(-\frac{5920}{T}\right)^{(a)}$
U_i ($cm^{-2}K/Vs$)	$\frac{10000}{T}\exp\left(-\frac{9655}{T}\right)^{(a)}$ $\frac{4\text{x}10^{3}}{T}\exp\left(-\frac{9167.5}{T}\right)^{(b)}$	$\frac{3.34\text{x}10^{4}}{T}\exp\left(-\frac{10680}{T}\right)^{(a)}$

Table 5.1. The literature data on the concentration of the intrinsic defects, the defect formation energy and mobility for BaF_2 and CaF_2: (a) from Ref. [1973Boll1] and [1973Boll2], and (b) from Ref. [1968Bars1] and [1968Bars2].

where n_F is density of anti-Frenkel defects, u_v and u_i mobility of the fluorine ion vacancies and of the interstitial fluorine ions, respectively.

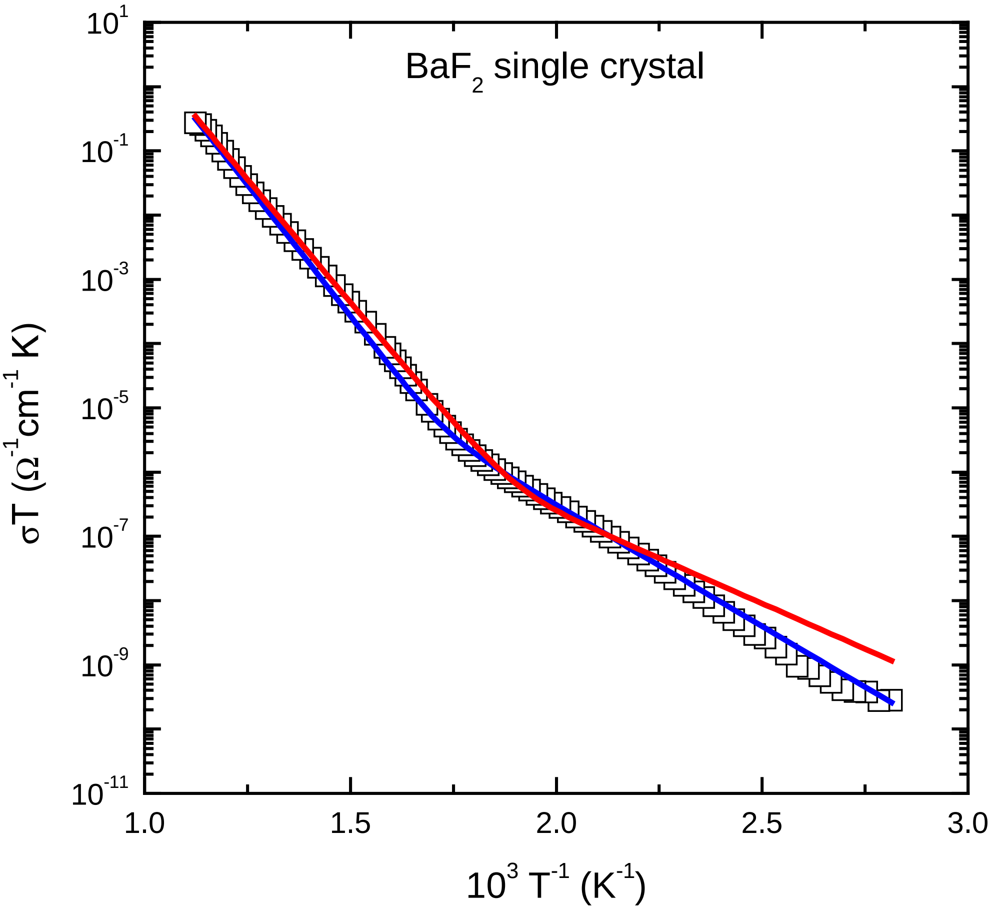

Figure 5.1.2. Temperature dependence of the measured anionic conductivity of the BaF$_2$ (open squares), together with result from fitting with an impurity content of 6x10^{16} cm^{-3} using the data from Ref. [1973Boll1] and [1973Boll2] (blue line), and an impurity level of 10^{15} using data from Ref. [1968Bars1] and [1968Bars2] (red line).

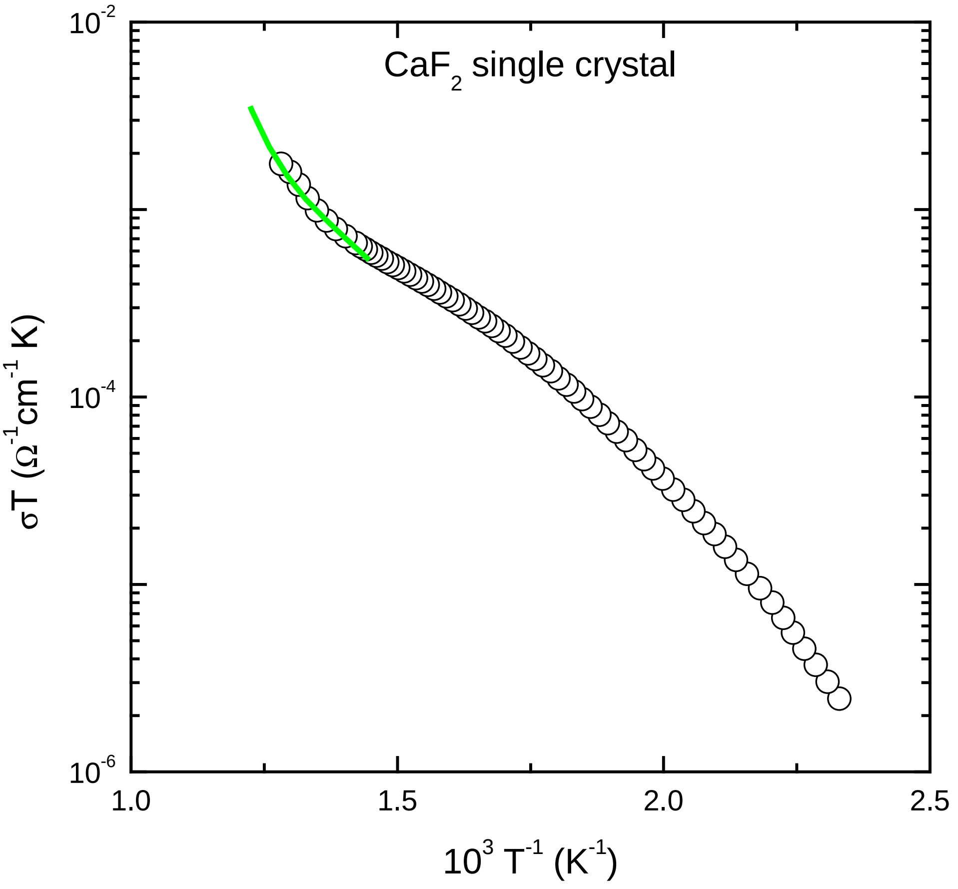

Figure 5.1.3. Temperature dependence of the measured anionic conductivity of the CaF_2 (open circles), together with result from fitting with an impurity content of $8x10^{16}$ cm^{-3} using the data from Ref. [1973Boll1] and [1973Boll2] (green line).

5.2. Heterolayers of CaF_2/BaF_2

5.2.1. Parallel Measurements

For all parallel measurements CaF_2/BaF_2 samples were grown on Al_2O_3 (012) substrates by MBE technique in a high-vacuum chamber with a base pressure of 10^{-9} mbar. Prior to deposition, all the Al_2O_3 substrates were optically polished on one side and coated with Ti films on the other side to stabilize and homogenize the temperature. Single crystals of CaF_2 and BaF_2 were sublimed at 1180° C and 1000° C, respectively. For all the samples, BaF_2 was deposited as the first layer because, in contrast to CaF_2, growth occurs exclusively in [111] direction. During growth, the substrate temperature was kept at 500°C, and the growth rate was about 1 nm/min [2000Sata],[2002Sata].

5.2.1.1. Thickness and Temperature Dependence

In order to obtain more fundamental insight into ionic processes, there are still some points to be investigated in more detail: the understanding of the mesoscopic situation (i.e. for film thicknesses thinner than 50 nm); the structural investigation of the interfacial and individual layer morphologies. For this reason, bilayer samples with various thicknesses of CaF_2 on top of constant layer of BaF_2, were prepared by molecular beam epitaxy technique. The investigation of the overall conductance as a function of the thickness permits the deconvolution of bulk conductivity of CaF_2 and interface effects between CaF_2 and BaF_2. In Ref. [2004Guo2] the authors have analyzed and deconvoluted the contributions of bulk and interfaces to the conductivity of BaF_2. Space charge contributions of surface layer and Al_2O_3 substrate contact could be identified.

Experimental

The thickness of the first layer BaF_2 was kept constant (around 200nm), and the thickness of second layer CaF_2 was varied from 200 nm to 25 nm (Figure 5.2.1) in order to tune the concentration profile from the semi-infinite space charge to situation in which the space charge regions overlap in the top layer.

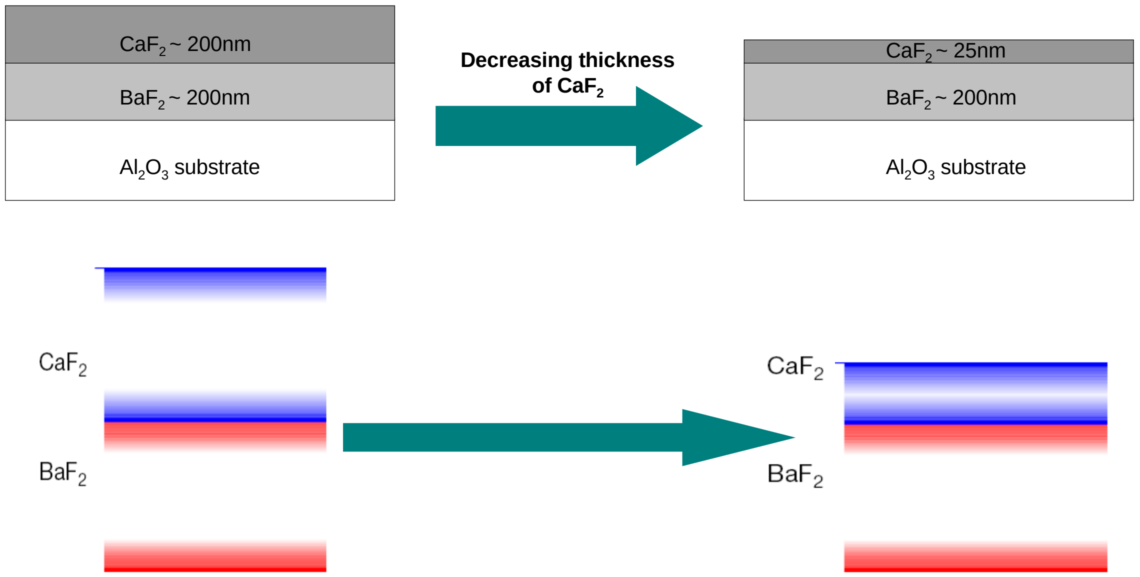

Figure 5.2.1. Schematic drawing of samples and space charge situation.

After growth, the films were cooled down to room temperature at a rate of 10°C/min. Then every sample was cut into two halves. Two 300 nm thick rectangular Pt electrodes with a spacing of 1mm in 13mm length were deposited on one half of the sample surface by d.c. sputtering at room temperature (Figure 5.2.2).

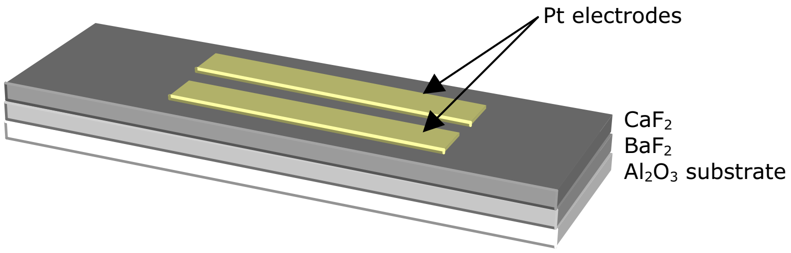

Figure. 5.2.2. Configuration of Pt electrodes on top of CaF_2 layer.

After annealing the sample at 610°C for 12 h in argon atmosphere (99.999% purity), the lateral conductivity was measured by a.c. impedance spectroscopy in the temperature range of 610–100°C with frequencies ranging from 1 to 10^7 Hz (with the experimental setup shown in Figure 4.2.5.1). The other half was used for thickness measurement, X-ray diffraction (XRD) and atomic force microscopy (AFM) measurements.

Results and Discussion

XRD measurements were carried out for all the films by conventional $\theta/2\theta$ scans using the Cu K_α line at room temperature. As shown in Figure 5.2.3, all the investigated samples exclusively exhibit [111] orientations. Surface morphologies of the films were detected by AFM. A typical image (2x2 μm) is displayed by Figure 5.2.4 showing that the surfaces are smooth with a uniform out-of-plane orientation.

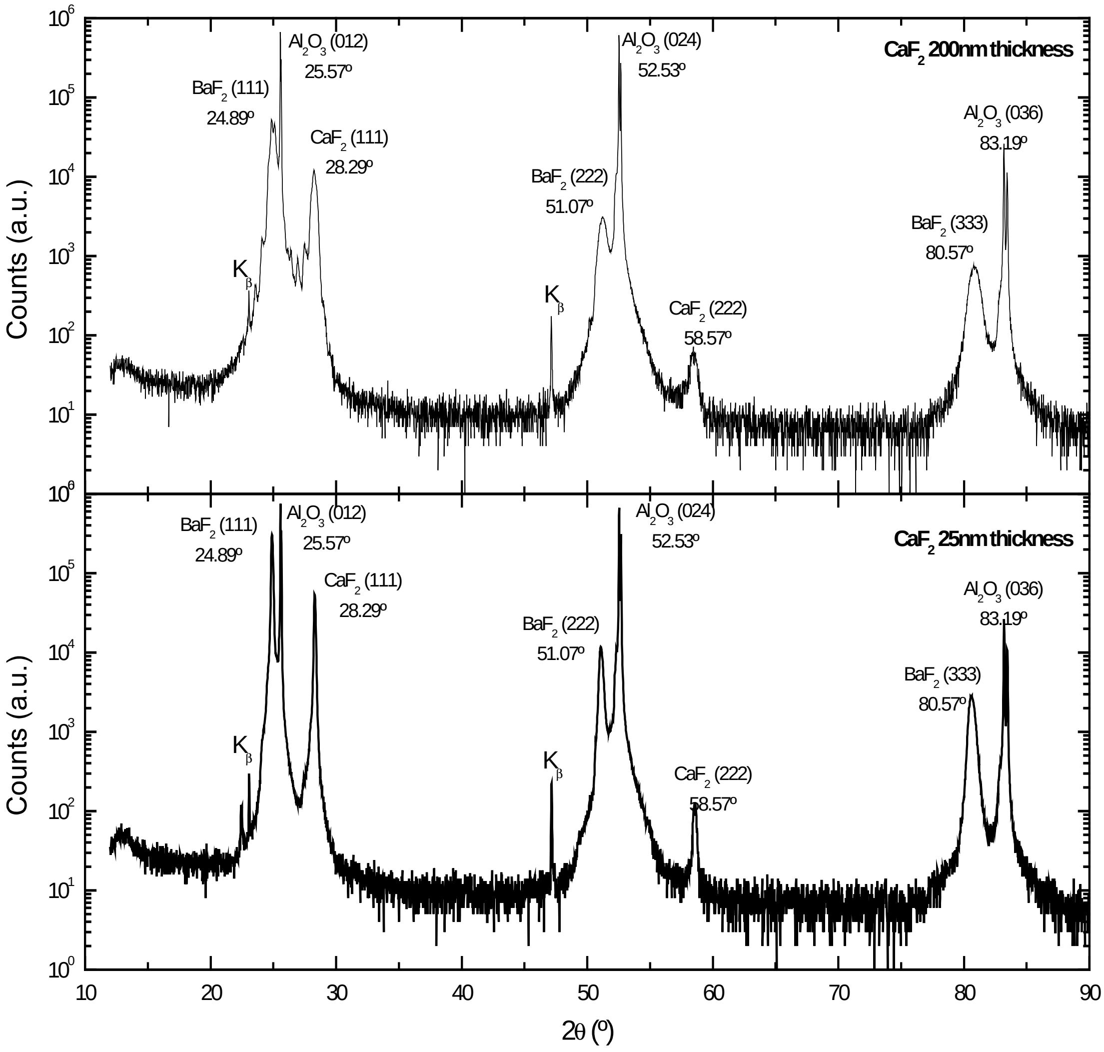

Figure 5.2.3. XRD patterns for the 200nm and 20nm CaF_2 grown on top of the 200nm BaF_2 on Al_2O_3 (012) substrate.

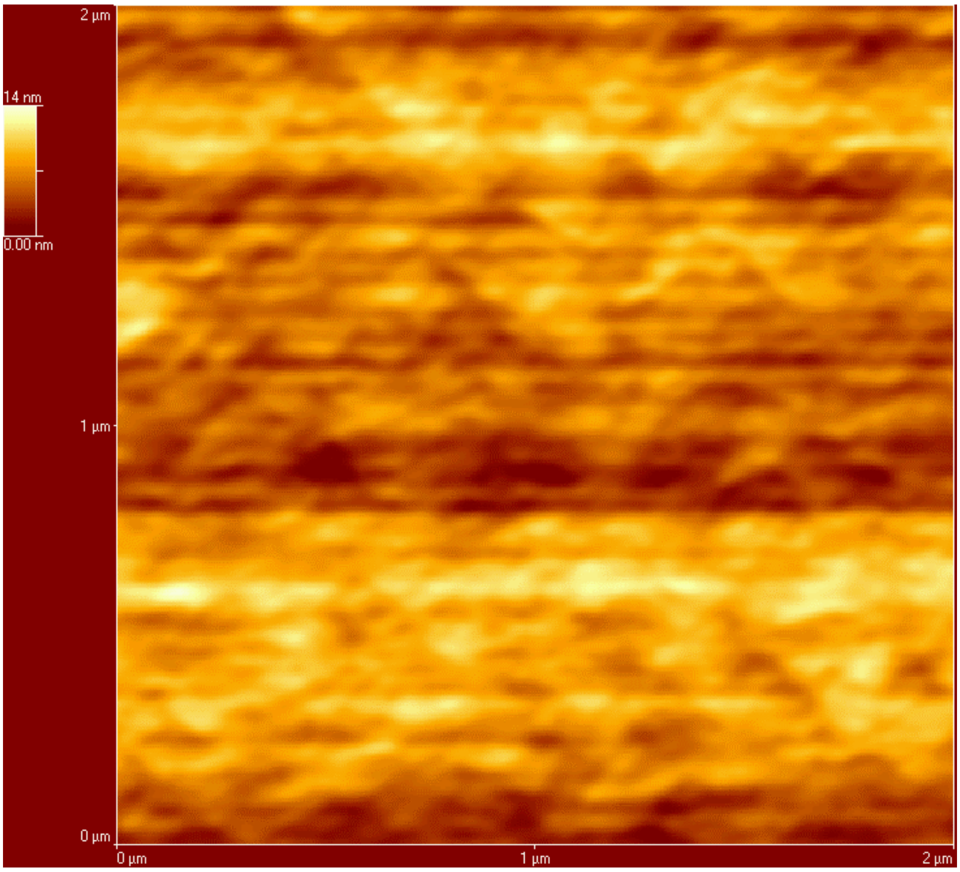

Figure 5.2.4. Surface morphology of the top layer for CaF_2/BaF_2 film grown on Al_2O_3 (012) substrate investigated by AFM technique in an area of 2x2 μm.

In a.c. impedance spectroscopy measurements, the samples typically exhibited one semi-circular arc and one incomplete arc attributed to the electrode effects (Figure 5.2.5). The effective capacitance of the high frequency arc is determined by stray capacitances and does not allow one to separate possible domain boundary resistances in the impedance spectrum. We extracted the overall film resistance from the intersection of this arc with the real axis. From electrode distance and area, the normalized parallel conductance (Y^{II}) could be calculated which after division through the total film thickness (L) yields the effective overall film conductivity ($\sigma_{\mathrm{m}}^{\mathrm{II}}$).

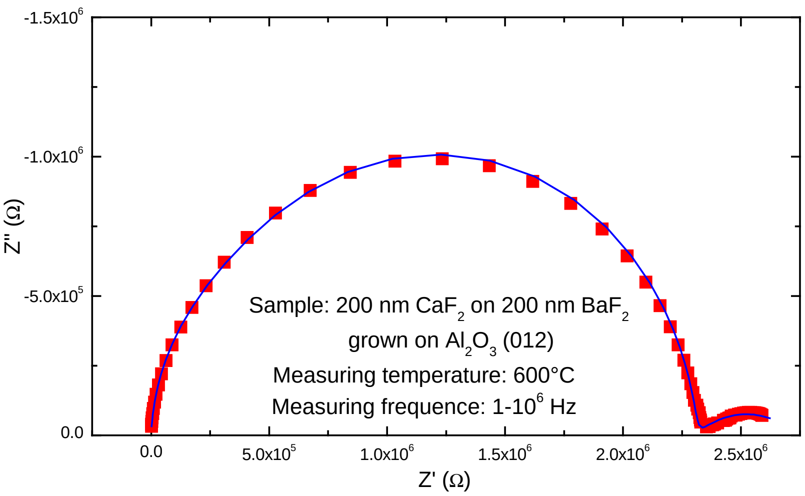

Figure 5.2.5. A typical impedance spectrum for the CaF_2/BaF_2 bilayer grown on Al_2O_3 (012). The measured temperature is 600°C, frequency ranges from 1 to 10^6 Hz.

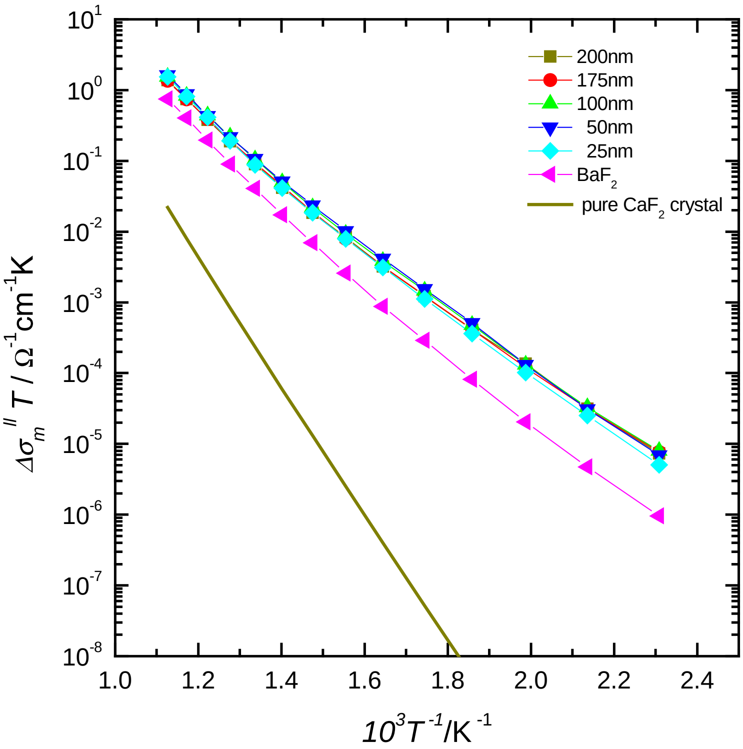

Figure 5.2.6. Arrhenius plots for CaF_2 films with different thicknesses (25÷200 nm) grown on top of 200 nm BaF_2 on Al_2O_3 (012) substrates. The bulk conductivity of a pure single crystal CaF_2 [1973Boll1] and the conductivity of single layer BaF_2/Al_2O_3 (012) are also drawn here for comparison.

Figure 5.2.6 displays the thickness dependence of $\Delta\sigma_m^{\parallel}$ for all the films together with the theoretical calculated conductivity of pure single crystal CaF_2 [1973Boll1] and conductivity of a single layer of 200nm BaF_2 on Al_2O_3 (012). The measured parallel conductivity of the films is larger than the conductivity of single crystal CaF_2. Taken into account the conductivity contribution from all the interfaces (between BaF_2 and substrate and BaF_2/CaF_2) and bulk parts of each layer, the normalized parallel conductance with respect to the dimensions perpendicular to the x-axis $(Y^{\parallel})$ can be expressed by:

$$Y^{\parallel} = Y_{sub} + Y_{BaF_2} + Y_{int} + \sigma_{\infty}(CaF_2) \cdot \ell$$

where: Y_{sub} is the contribution of the substrate/BaF_2 interface, Y_{BaF_2} refers to the contribution from the bulk BaF_2 layer, Y_{int} is the excess value due to the CaF_2/BaF_2 interface, $\sigma_{\infty}(CaF_2)$ is the bulk conductivity of the CaF_2 layer and ℓ is the thickness of the top layer of CaF_2. The contribution of the gas/solid interface can be neglected because the effect of the gas phase is expected to be much weaker than the effect of the oxide substrate with its specific interaction [1995Ma1]. The contribution of the substrate/BaF_2 interface and of the bulk BaF_2 layer is assumed constant for all the samples since all the bilayers have the same BaF_2 thickness and were grown on the substrates with the same orientation. The effects of the bulk CaF_2 and that of CaF_2/BaF_2 interface can be separated by substracting, for of each individual sample, the values of the normalized conductance of the 200 nm thick BaF_2 layer on Al_2O_3 substrate.

$$Y_{CaF_2}^{\parallel} = Y^{\parallel} - (Y_{sub} + Y_{BaF_2}) = Y_{int} + \sigma_{\infty}(CaF_2) \cdot \ell$$

In Figure 5.2.7 the normalized conductance of the CaF_2 on top of the 200nm BaF_2/Al_2O_3 layer grown on Al_2O_3 (012) at given temperatures is plotted as a function of thickness.

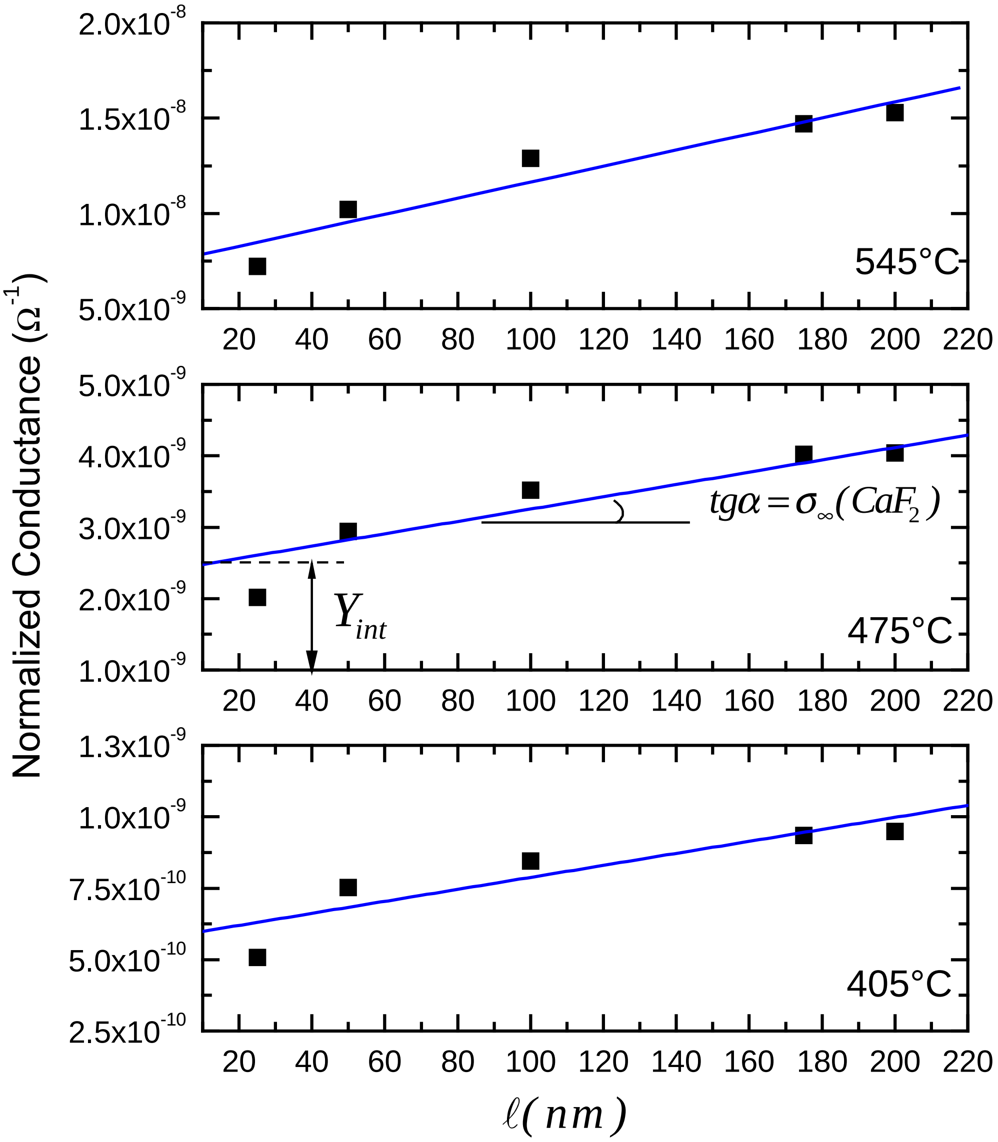
2.0x10-8
1.5x10-8
1.0x10-8
5.0x10-9
545°C
5.0x10-9
4.0x10-9
3.0x10-9
2.0x10-9
1.0x10-9
$tg\alpha = \sigma_\infty(CaF_2)$
Y_{int}
475°C
1.3x10-9
1.0x10-9
7.5x10-10
5.0x10-10
2.5x10-10
405°C
20 40 60 80 100 120 140 160 180 200 220
Normalized Conductance (Ω^{-1})
$\ell(nm)$

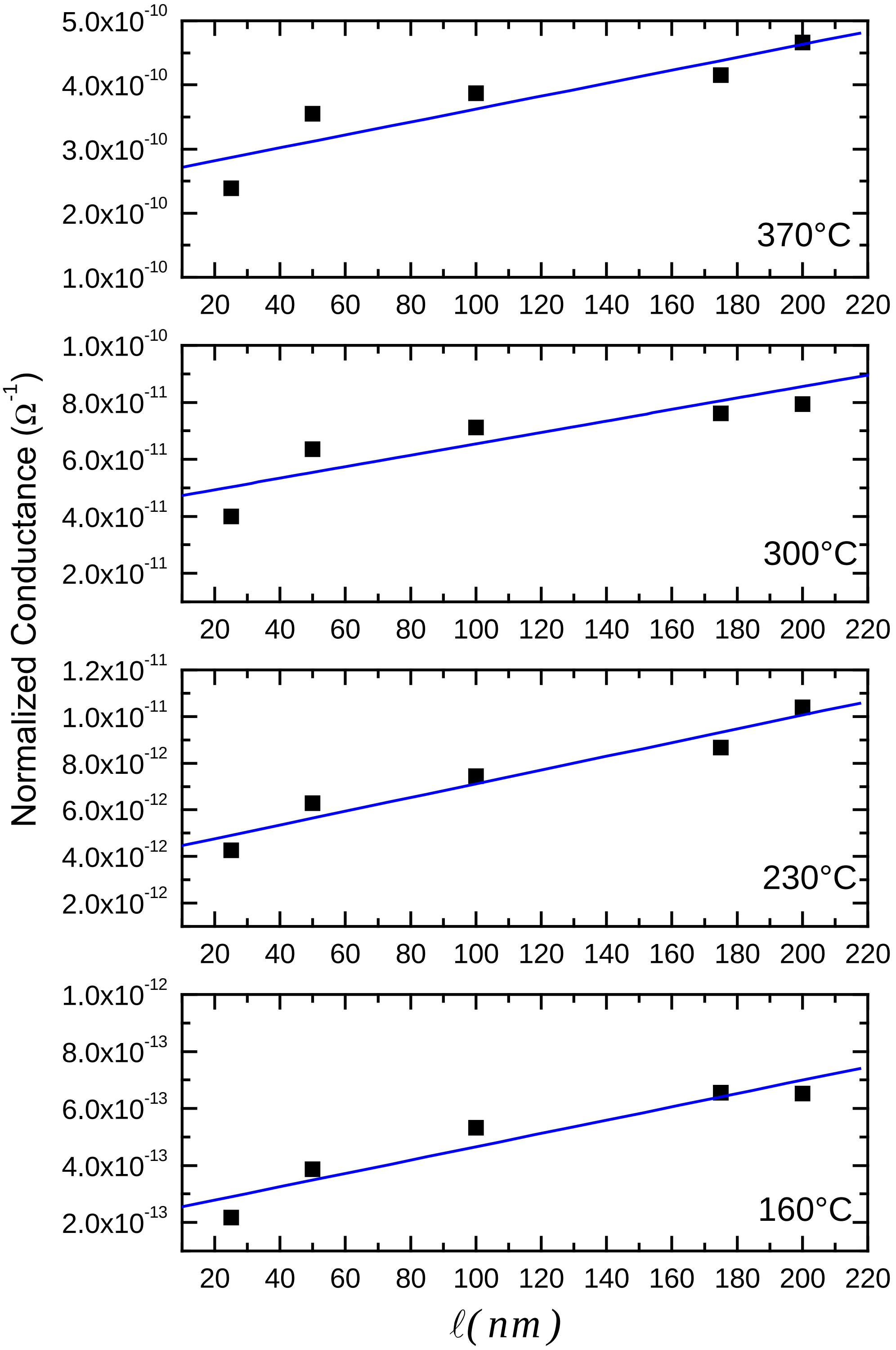

Figure 5.2.7. Normalized conductance $Y^{||}_{CaF_2}$ of (111) CaF_2 as a function of thickness at given temperatures.

The bulk conductivity of the CaF_2 layer ($\sigma_\infty(CaF_2)$) can be now calculated from the slope of the linear part, and from interception with Y-axis the CaF_2/BaF_2 interface contribution can be estimated.

Figure 5.2.8 show the temperature dependence of the bulk conductivity of CaF_2 as calculated from the slope ($\sigma_\infty(CaF_2)$), and the theoretical estimation in extrinsic region (σ_{th}, with an impurity content of ~$1.0x10^{17}$ cm^{-3}).

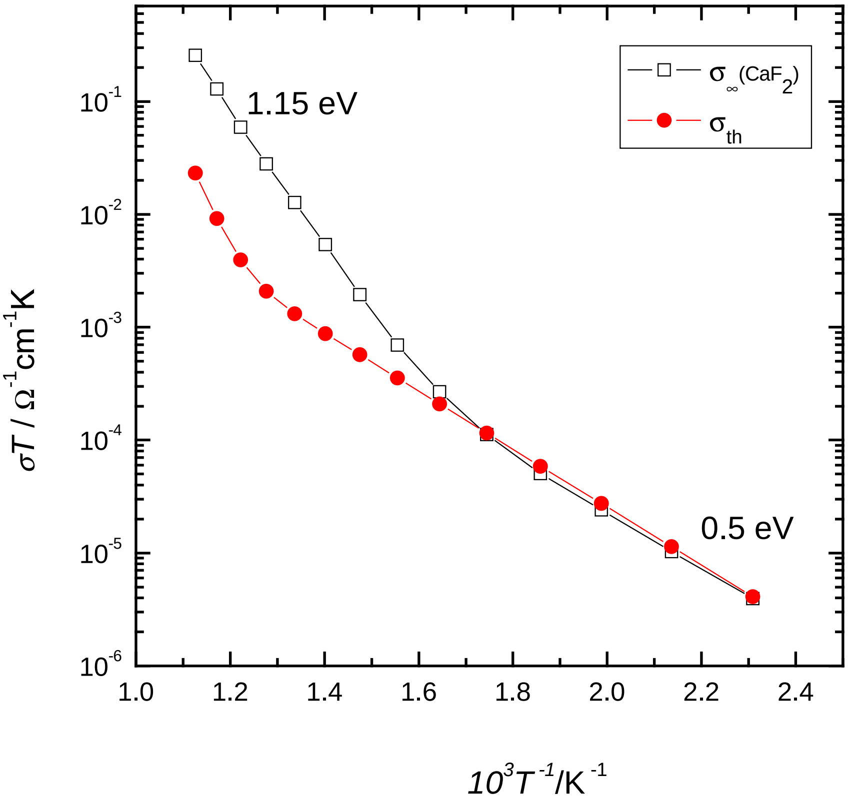

Figure 5.2.8. Arrhenius plot of the bulk conductivity of CaF_2 as calculated from the slope ($\sigma_\infty(CaF_2)$), and from the theoretical estimation in extrinsic region (σ_{th}, with an impurity content of ~$1.0x10^{17}$ cm^{-3}).

A good agreement between estimated $\sigma_\infty(CaF_2)$ and the theoretical calculation in the extrinsic region is only achieved at lower temperature. Due to the growth of the samples in MBE conditions and the use of very pure starting chemicals the major impurities can be assumed to be oxygen defects ($O_F^{'}$).In this case a value of an impurity content of ~$1.0x10^{17}$ cm^{-3} is almost the same like as previous works [2000Sata],[2004Guo1].

In Figure 5.2.9 is plotted the CaF_2/BaF_2 interface contribution from this analysis, and compared to previous studies. There are no major differences between the values of the normalized conductance for one interface.

In the high temperature region, the difference between the $\sigma_\infty(CaF_2)$ and the theoretically calculated bulk conductivity cannot be explained yet and further intensive exploration is necessary.

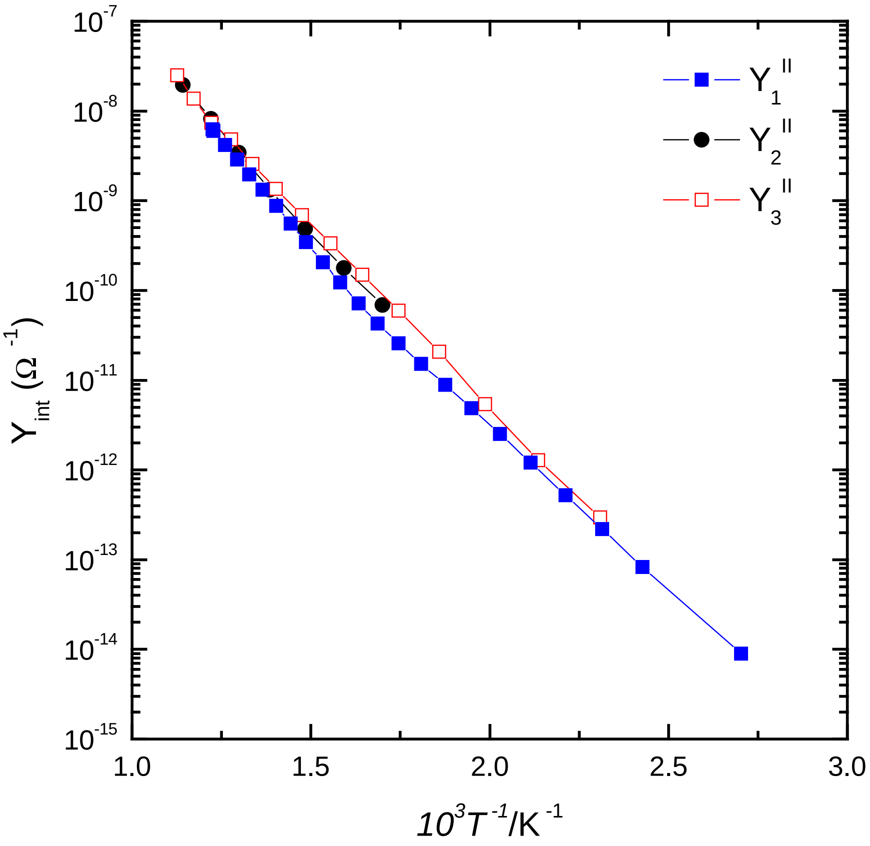

Figure 5.2.9. Normalized conductance of CaF_2/BaF_2 interface (Y_{int}). Blue colour refers to wok done in Ref. [2000Sata], black one is taken from Ref. [2004Guo2], and red refers to this study.

5.2.1.2. Annealing Effects

It is very well known that by introducing interfaces in ionic systems the overall parallel ionic conductivity to the interfaces can be improved, but also represents a powerful tool to tune defect chemistry and ion conductivity properties.

The purpose of this experiment is to understand annealing effects, in particular, the anomalous increase in the resistance of the sample (or decrease of the parallel conductivity of the sample) as the annealing temperature increase. Depending by the numbers of pairs of CaF_2/BaF_2 layers the conductivity degradation occurs between 300°C and 500°C on first heating.

Figure 5.2.10 shows the configuration of the samples with different thicknesses of individual layer and the ionic conductivity profiles from a semi-infinite space charge situation to a mesoscopic situation, in which the space charge layers overlap.

The films used for this study were grown in the MBE chamber with the same parameters described before, but all samples exhibit a total thickness of about 400 nm, also the number of interfaces is different from sample to sample. Periodicity and thickness were varied over a wide range (individual layer thicknesses: 6.5-200 nm) by computer-controlled effusion cell shutters [2000Sata],[2002Sata].

The electrodes were deposited from the same material (Pt) and in the same configuration as in previous experiment.

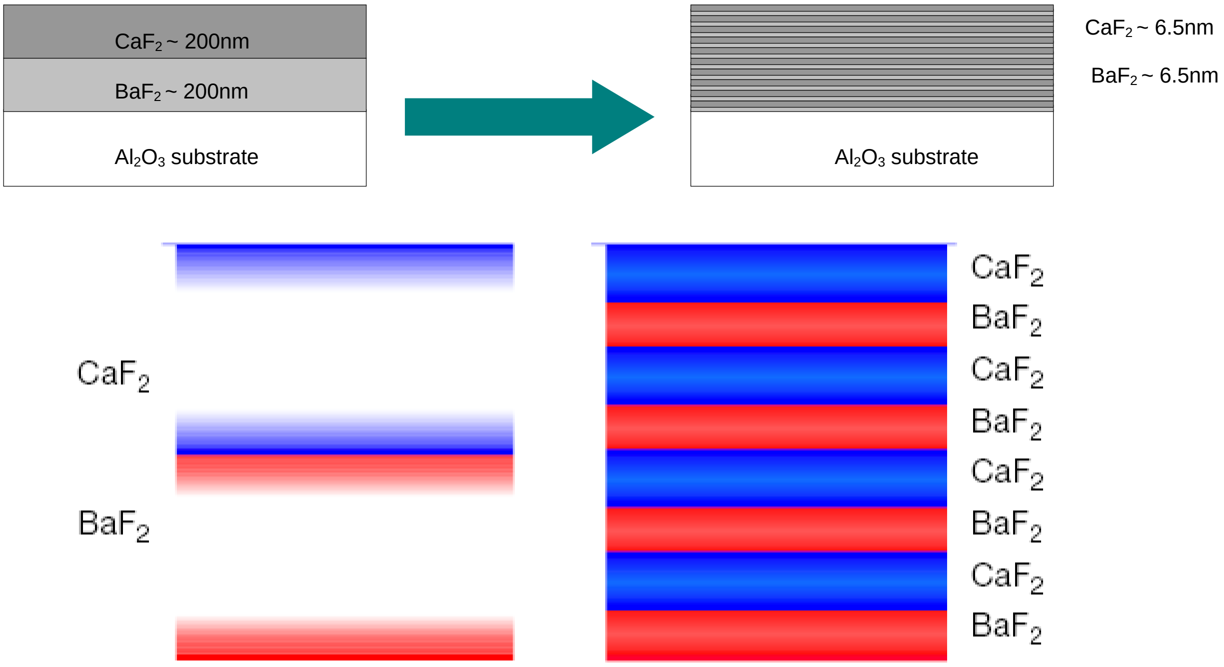

Figure 5.2.10. The configurations of the grown samples with different thicknesses of individual layer ranging from 200nm to 6.5 nm (up) and conductivity profiles in the semi-infinite space-charge and mesoscale situations (down).

Also, XRD measurements were performed for all the samples by conventional $\theta/2\theta$ scans using the Cu K_α line at room temperature. As shown in Figure 5.2.11, all the investigated samples exclusively exhibit [111] orientations, independent of numbers of layers.

A typical image (5x5 μm) is displayed by Figure 5.2.12 and shows a smooth surface (roughness ~4nm), with a very good out-of-plane orientation.

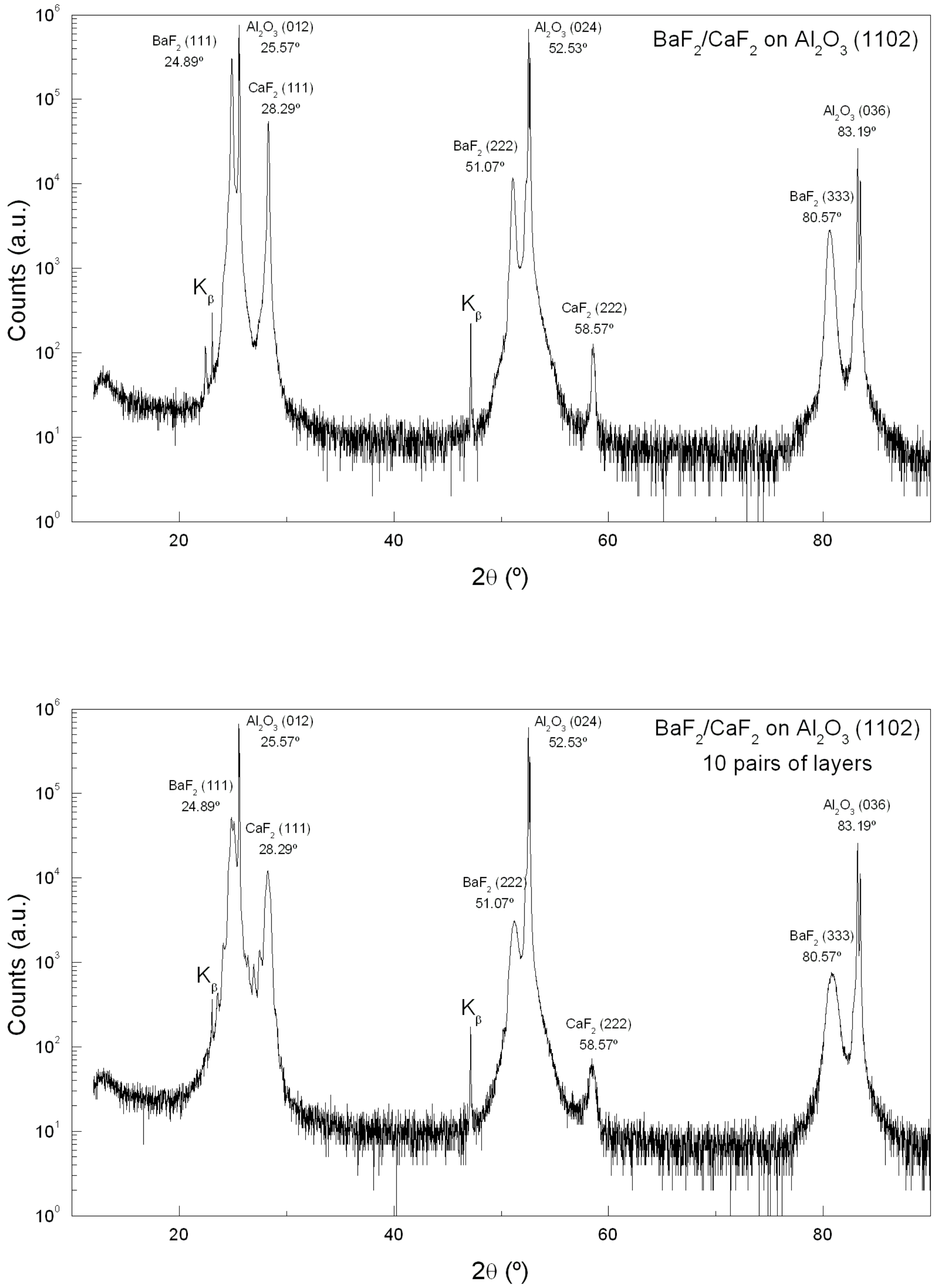

Figure 5.2.11. X-Ray Diffraction pattern for CaF_2/BaF_2 heterostructures (~400nm) on Al_2O_3 substrate with different thicknesses: one pair of 200 nm each layer (up) and 10 pairs with 20 nm thickness of each layer (down).

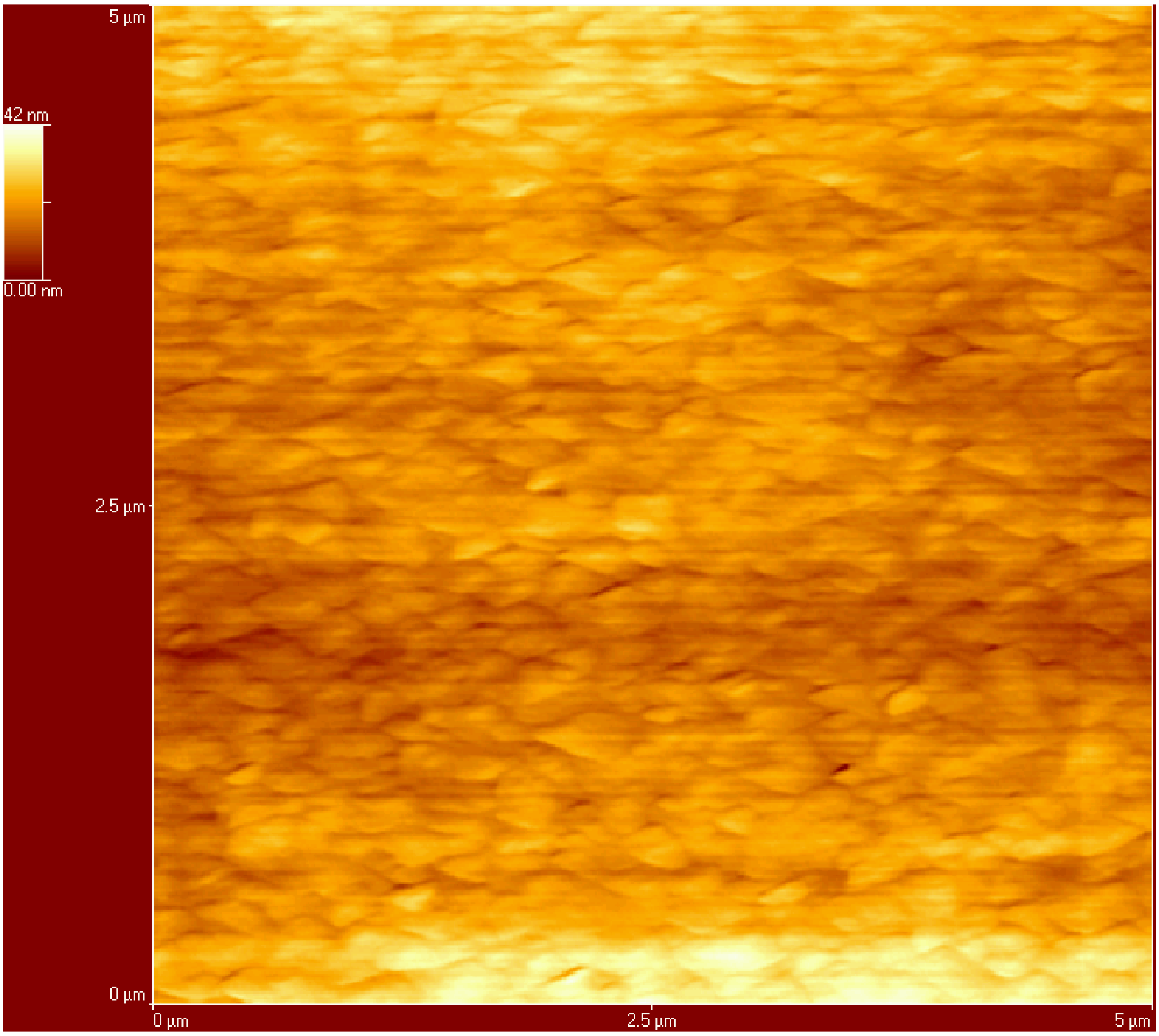

Figure 5.2.12. Surface morphology of the top layer for CaF_2/BaF_2 heterostructure with 20 pairs, grown on Al_2O_3 (012) substrate investigated by AFM technique in an area of 5x5 µm.

The samples were annealed at two different temperatures: 250°C and 600°C for 12 h in argon atmosphere (99.999% purity). Later on, the lateral conductivity was measured by a.c. impedance spectroscopy with frequencies ranging from 1 to 10^7 Hz and in a temperature range that did not exceed the annealing temperature: one sample from 50°C to 250°C, and a second from 50°C to 600°C (see the experimental setup in Figure 4.2.5.1).

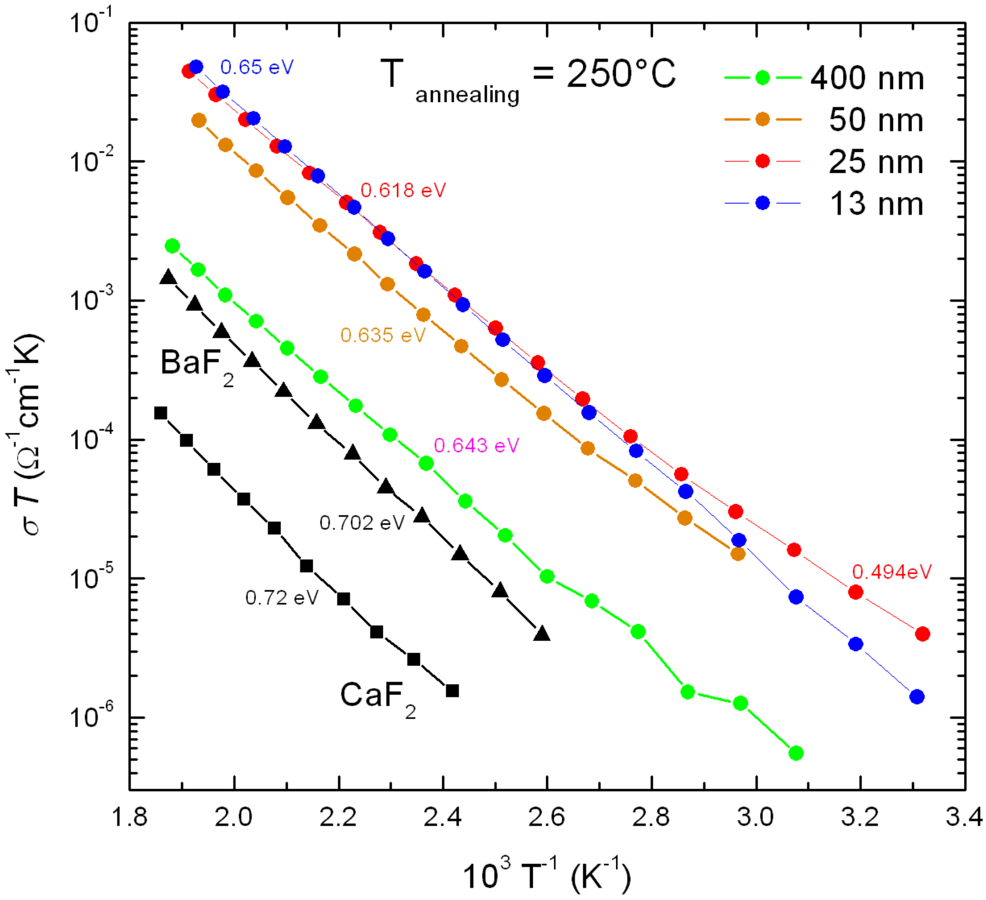

Figure 5.2.13. Arrhenius plot of the heterostructures annealed at 250°C.

Conductivity results determined from impedance spectroscopy for the samples annealed at 250°C are given in Figure 5.2.13. The measured effective parallel conductivity increases with increasing interfacial density (decreasing period) in the period range 400 nm to 13 nm (the period refers to the thickness of a pair: CaF_2 plus BaF_2 layer).

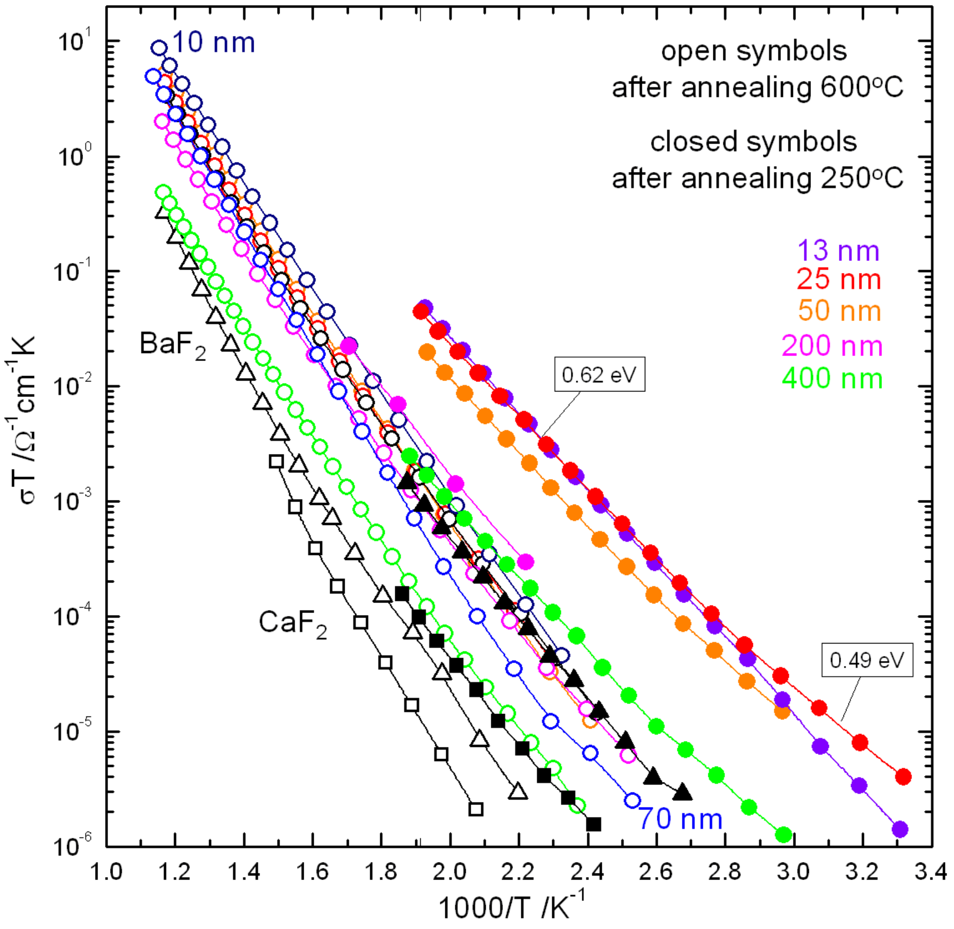

Figure 5.2.14. Arrhenius plot of the heterostructures annealed at 250°C (closed symbols) and at 600°C (open symbols).

With T_{max} ≈ 250°C which is much lower than the previous annealing temperature (600°C), as-grown conductivity values from the first heating are reproducible in thermal cycles. The heterolayers show conductivities that are higher than those of pure CaF_2 or BaF_2 films (Figure 5.2.14).

Low temperature annealing leads to an increase in conductivity values by at least one order of magnitude, but also the activation energies is lowered by more than 0.1eV, decreasing with increasing interfacial densities. In this low temperature annealed sample values of the activation energy, calculated from the slope of the conductivity, suggest that the carriers responsible for conductivity are, mainly, the vacancies in both materials ($V_F^\bullet$).

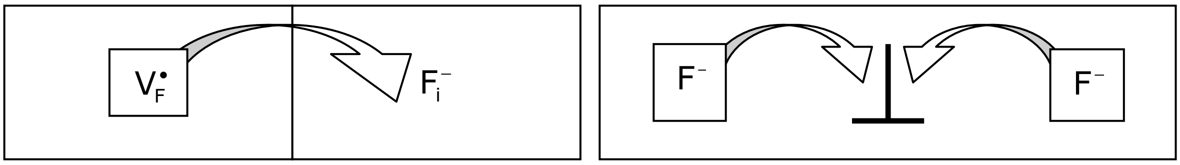

a) b)

Figure 5.2.15. Schematic representation of the conduction mechanism in (a) the annealed samples and (b) non-annealed samples.

This can be associated with the existence of unstable dislocations not only at the interface, but also inside the layers that can be annealed out by thermal treatment. These dislocations at the interfaces form already during growth of the first or second monolayer due to extremly high lattice mismatch. Internal dislocations leading to enhanced non-equilibrium conductivities has been observed in different ionic system [1995Saito],[1999Puin],[1987Maier3],[1996Fle]. These unstable dislocations have to be distingueshed from the misfit dislocations that absorb misfit strain and are stable constituents of the interfaces. (Figure 5.2.15b)

In assumption of maximum interfacial concentrations, the conductivity relation based on semi-infinite space charge which describes both temperature and thickness dependence is given by Eq. (2.39).

Using equation (2.39) for fitting the data, and with assumption the that for low temperature annealed samples the main carriers are vacancies in both layers, and for high temperature annealed samples that the main carriers are vacancies in BaF_2 and interstitials in CaF_2, a good agreement is obtained for thick samples (Figure 5.2.16).

This results in a clear picture: in annealed samples there is a fluorite (F^--ions) transfer from one phase to the other. This leads to an increase of fluoride vacancy concentration in one phase and of the fluoride interstitial in the other (Figure 5.2.15a). In a non-annealed samples this is superimposed by charging of dislocations leaving vacancies in the vicinity (Figure 5.2.15b).

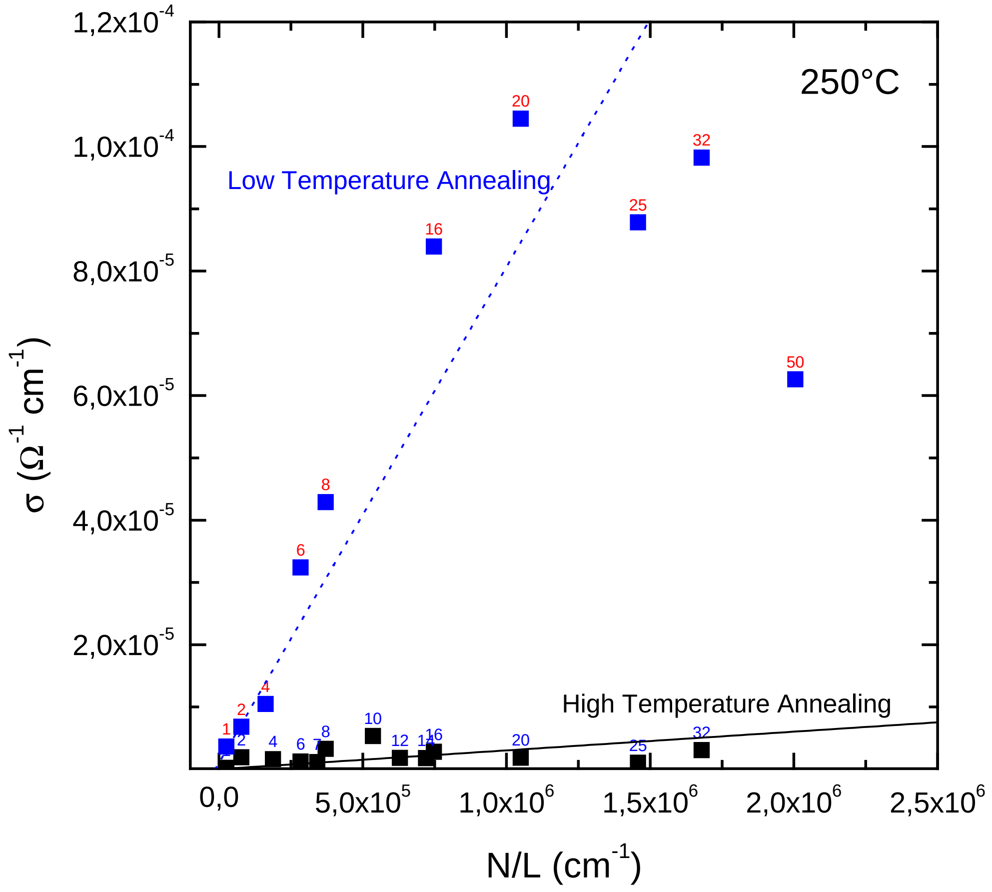

Figure 5.2.16. Variation of ionic conductivity with N/L at T= 250°C.

Figure 5.2.16 shows that the thickness dependence.The upwards bending reminds of the anomaly seen in Sata et al. [2000Sata]. This point will be observed again in Chapter 6.

Apart from that, the differently annealed samples show a similar behaviour as regards, the thickness dependence of annealed samples coresponding to Eq.(2.38).

The conductivity stabilization owing to the dislocations annealing occurs between 300°C and 500°C on first heating. In particular, the first cycles suffer from non-equilibrium effects. Figure 5.2.17 shows an example of the anomalous decrease of the parallel conductivity of the sample as the annealing temperature increase, from 100°C to 600°C. The sample was kept at different temperatures for 12 h in argon atmosphere. The experimental results became stable in time after annealing at 500°C.

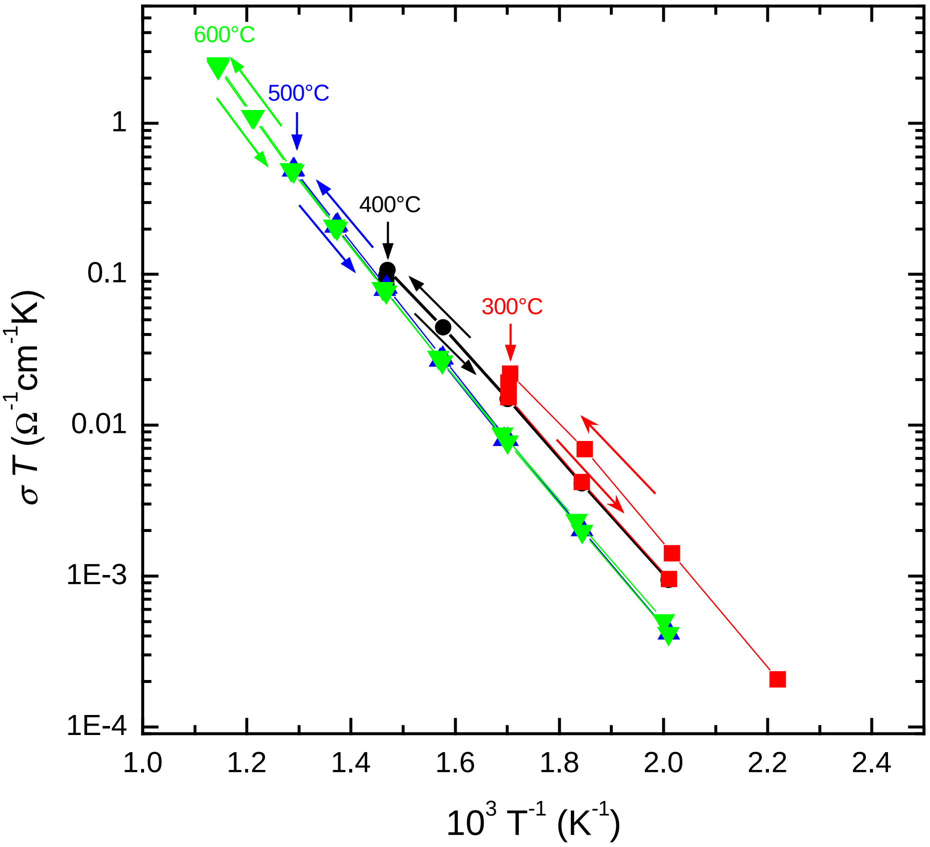

Figure 5.2.17. Decreasing of the parallel conductivity as the annealing temperature increase.

5.2.2. Perpendicular Measurements

As shown in the previous chapters, the lateral ionic conductivity increase linear with inverse interface spacing $1/\ell$ when ℓ is greater than the space charge thickness. As ℓ decreases further, the conductivity did not just linearly increase, it even bent upwards.

Extremely useful information is now also expected from conductivity results perpendicular to the interface which requires an appropriate substrate.

5.2.2.1. Si Substrate

For this experiment we need conductive substrates and CaF_2 films were grown on Si(111) substrates (both n^+ and p^+ mounted on the same holder) by MBE technique in a high-vacuum system with a base pressure in the 10^{-9} mbar range and a pressure is $5x10^{-8}$ mbar during deposition. Single crystal of CaF_2 is sublimed at 1100° C from a graphite crucible. After annealing Si (111) substrates in the MBE chamber at 950°C for 10 min. the shutter of effusion cell was open for another 5 min. with CaF_2 evaporating at a rate of 0.5 monolayer/min. After deposition to an initial layer of CaF_2 around 2-3 nm (4-5 monolayers) the substrates were cooled down to the deposition temperature.

When CaF_2 molecules are deposited at a lower rate, the time they stay as surface molecules is longer than at a higher deposition rate. Because the mobility of surface molecules is higher than the mobility of bulk molecules, at a low deposition rate, due to the longer residence time as surface molecules, CaF_2 molecules have greater chance to migrate to the proper epitaxial positions. This process is influenced not only by the deposition rate or the quality of the surface of Si (111) and, also, by the temperature of the substrate.

In this study, the samples have been prepared with different substrates temperature, which leads to the different growth rates, and have determined the influence on the epitaxial quality of CaF_2 layer. The thin films were prepared with the substrates temperatures in range of 400°-750°C. After the deposition the samples were cooled down to room temperature with a rate lower than 1°C/min. The CaF_2 is under a large tensile strain in the plane parallel to the interface for very thin epitaxial layers because of large thermal-expansion coefficient between CaF_2 and substrate (the linear expansion coefficient: $19x10^{-6}$ K^{-1} for CaF_2, compared with $2.5x10^{-6}$ K^{-1} for Si at room temperature) [1985Hash]. The tensile planar strain can result at room temperature if interfacial defects, which accommodated lattice mismatch at growth temperature, are not annealed out during cooling. If the cooling rate is too high, the large tensile strain in thin films will result in cracking of thicker films. But for high-quality thicker films do not crack because the strain can anneal out [1985Scho].

To determine the epitaxial quality, the X-Ray Diffraction and AFM measurements were performed.

The X-Ray Diffraction pattern of the thin films grown on Si (111) surface, with different substrate temperature (400°C, 500°C, 625°C, 750°C), is shown in Figure 5.2.18. For all the thin films grown on Si (111) substrate, the XRD measurements show a very well (111) orientation of CaF_2 thin film and low traces of SiO_2 (presumably due to insufficient annealing of the substrate for removing the protective layer from the surface).

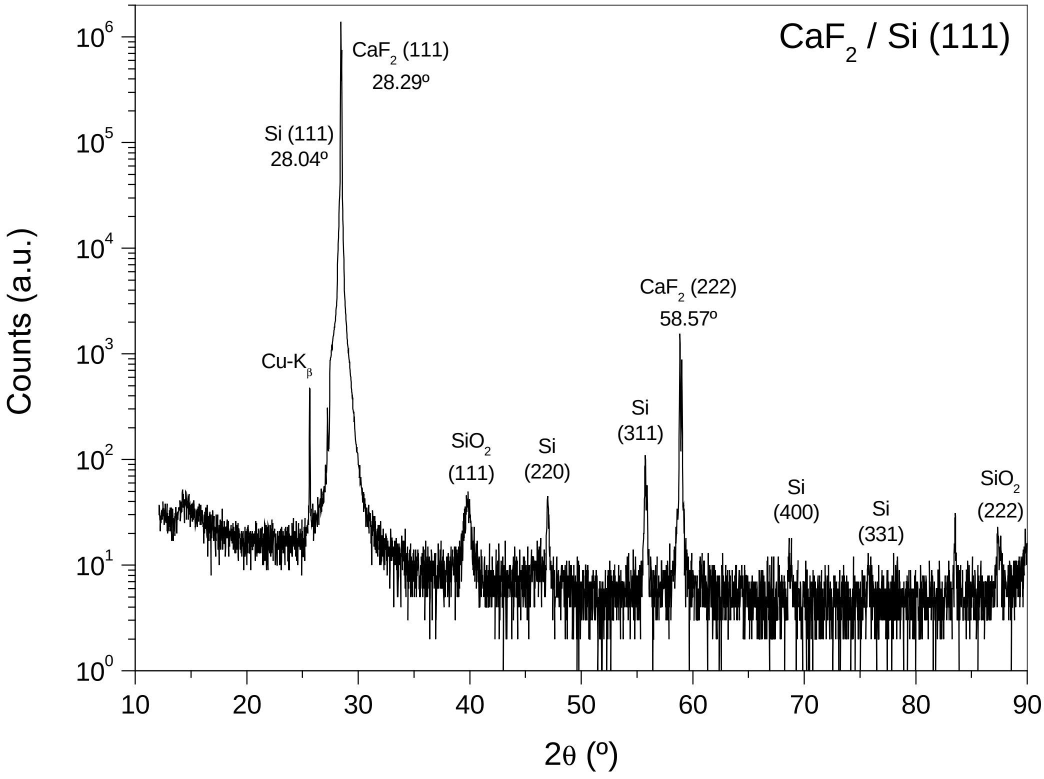

Figure 5.2.18. Typical X-Ray Diffraction pattern for CaF_2 (~200nm) on Si (111) substrate grown by MBE technique.

While using only the XRD measurements to demonstrate the high quality single-crystal growth of CaF_2 on (111) Si, it does not give the whole picture. In addition, scanning electron microscopy (SEM) was used to examine the surface morphology of the epitaxial films.

Using this method to study the surface of the layers reveals useful information about growth kinetics.

Figure 5.2.19 shows AFM images of the surfaces of around 200 nm thick CaF_2 thin films grown: (a) at 400°C (a), (b) at 500°C, (c) at 625°C and (d) at 750°C on (111)-oriented Si. The surface morphology of the samples, which were grown in same conditions, but on different Si substrates (n^+-type and p^+-type) is very similar.

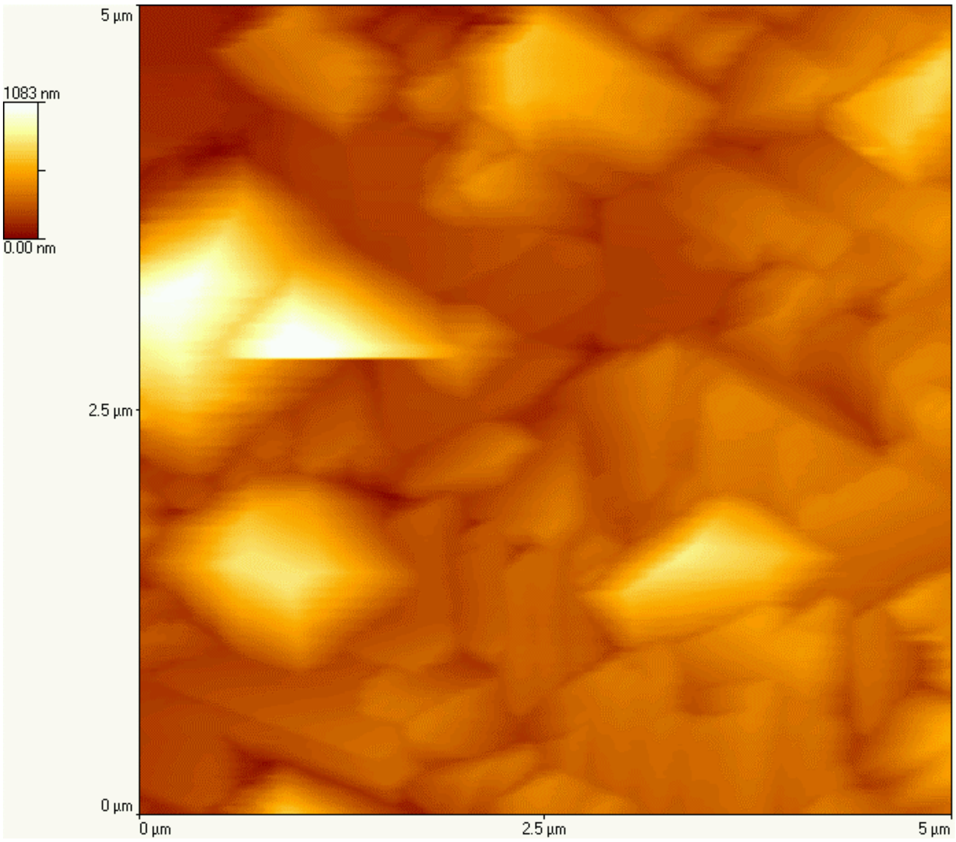
5 µm
1083 nm
0.00 nm
2.5 µm
0 µm
0 µm
2.5 µm
5 µm

(a)

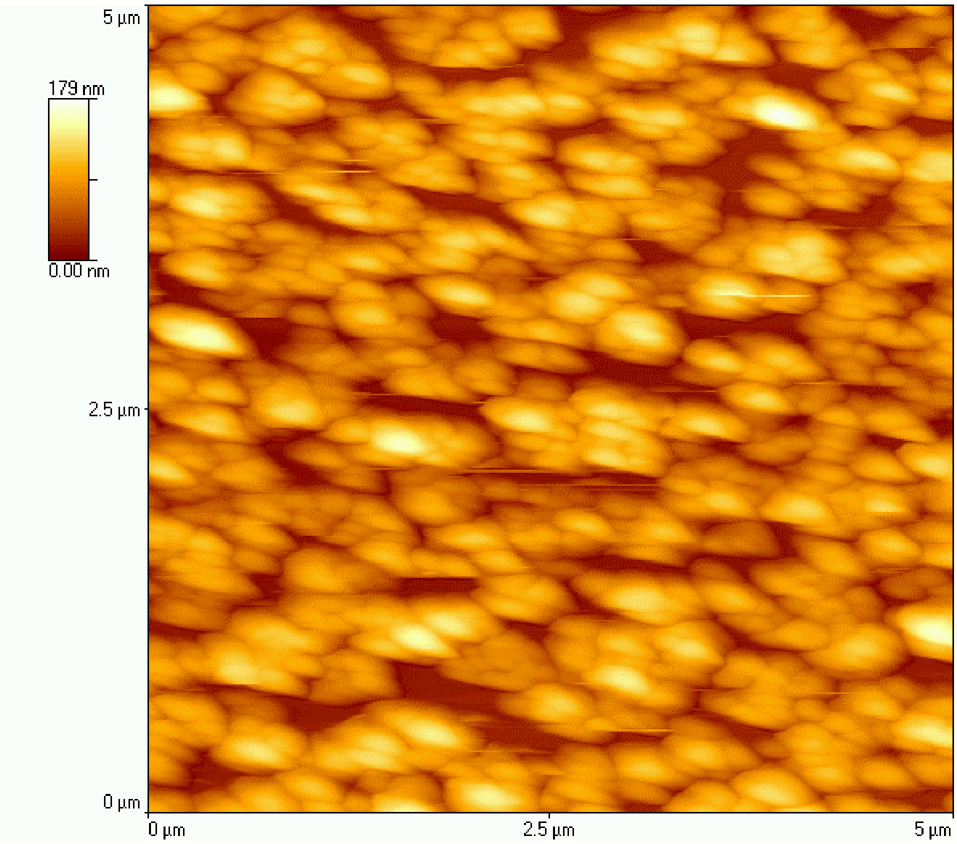
5 µm
179 nm
0.00 nm
2.5 µm
0 µm
0 µm
2.5 µm
5 µm

(b)

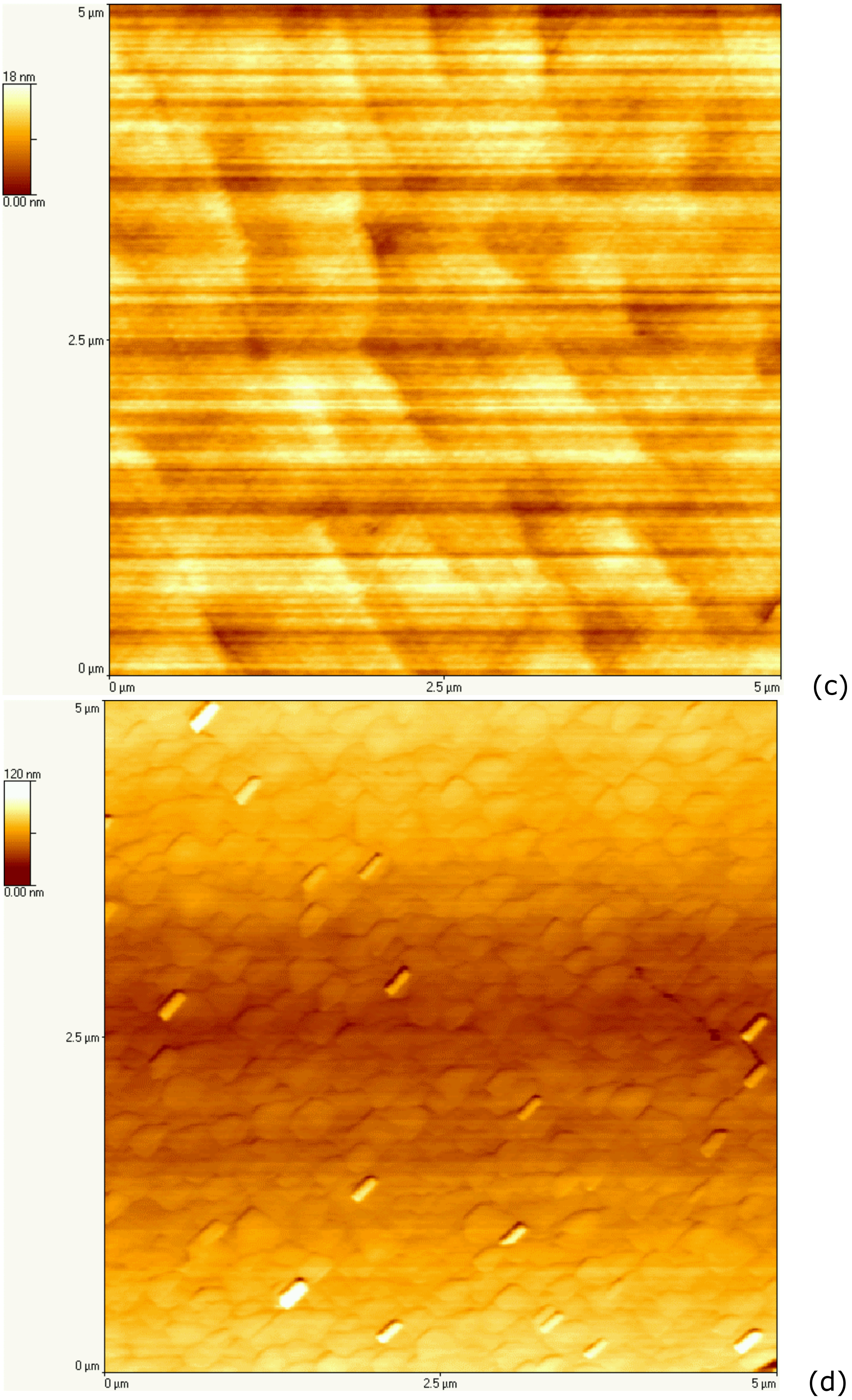

Figure 5.2.19. AFM images of the surfaces of around 200 nm thick epitaxial CaF_2 films grown on (111) oriented Si substrate: (a) at 400°C (a), (b) at 500°C, (c) at 625°C and (d) at 750°C.

As shown in Figure 5.2.19 the growth mechanism is changing with substrate temperature:

a) At 400°C the growth mode is three-dimensional (Volmer-Weber growth). In this case, the initial deposit atoms aggregate as small three-dimensional (3D) islands which increase in size as further deposition continues until they touch and intergrowth to form a continuous film. The AFM image shows that the roughness of the (111) CaF_2 surface is very high due to the formation of a big pyramids, and also some large misoriented crystallites (Figure 5.2.19a).

b) At 500°C the same three-dimensional growth mode occurs, but the grains size is decreased and the number of nucleation centres is increased. This leads to a decrease in the roughness (Figure 5.2.19b).

c) At 625°C the growth mode changes to a two-dimensional or layer-by-layer growth (Frank-van der Merwe growth). The surface is smooth and the roughness that is observed in image is too fine to be resolved at this scale (Figure 5.2.19c).

d) At 750°C a two-dimensional growth is also observed, with the surface roughness a little increased (Figure 5.2.19d).

The most important feature occurs at 625°C, where the three sets of parallel straight steps with 60° angles between each set are observed. The straight step lines result from dislocation glide to relieve the thermal mismatch strain on cool-down from growth to room temperature.

AFM measurements show that epitaxially CaF_2 layers can be grown on (111) oriented Si (both n^+ and p^+-*type*) if the substrate temperature is in the 625°C-750°C range. This results are in a good agreement with previous works [1993Zogg],[1992Blun].

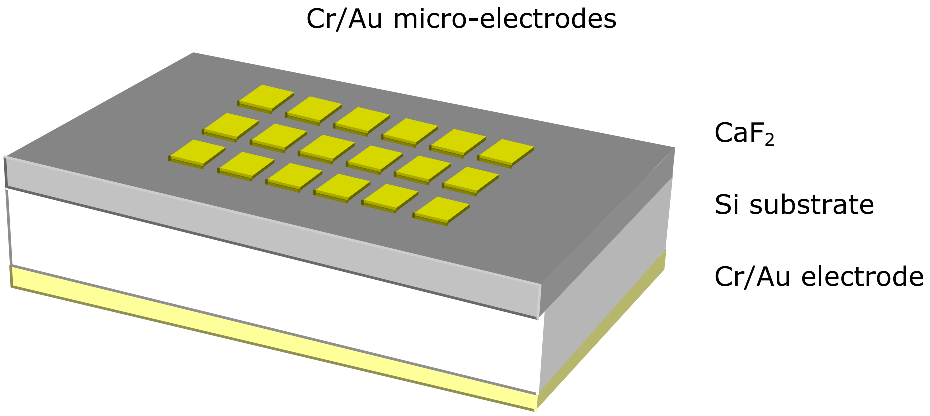

Figure. 5.2.20. Configuration of the MBE grown samples used for perpendicular measurement with Au electrodes on top of CaF_2 layer on Si (111) substrate.

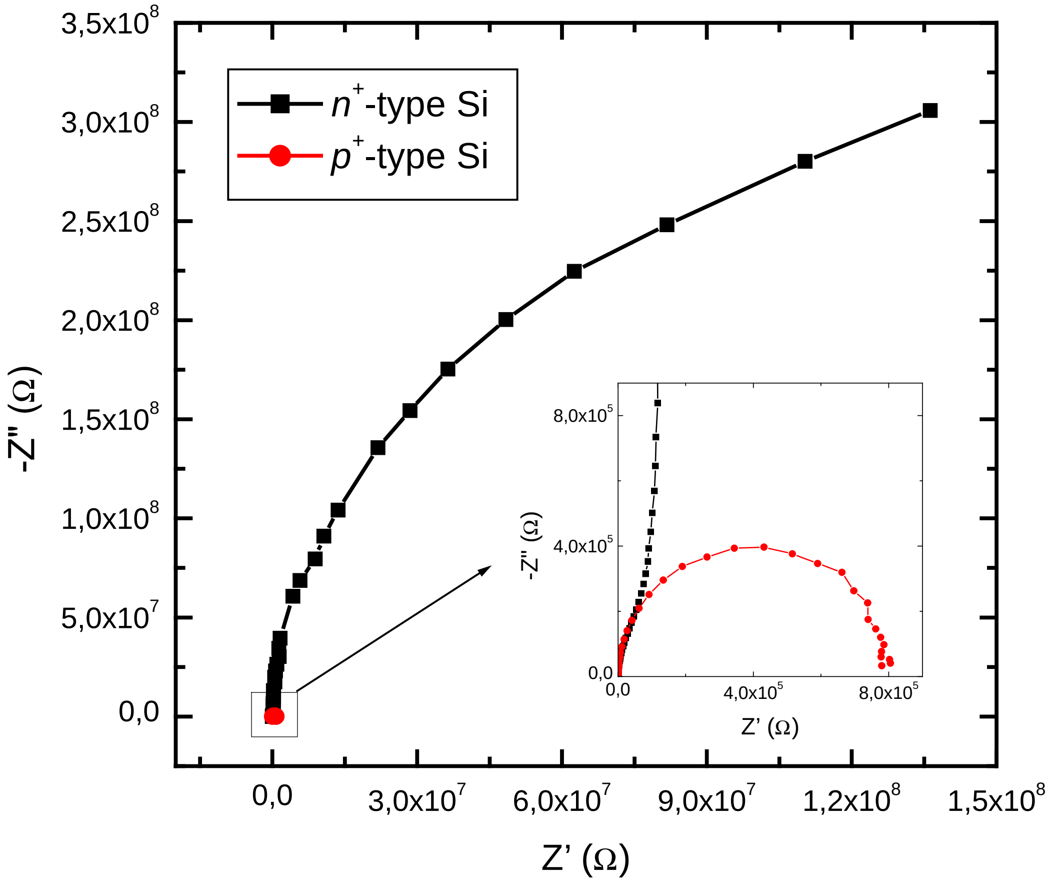

Figure 5.2.21. The impedance spectra for the CaF_2 grown on Si (111): red points refer to the samples grown on p^+-*type* Si, and black points for n^+-*type* Si. The measurements were carried out at room temperature, and frequency ranges from 1 to 10^7 Hz.

After growth, the films were cooled down to room temperature at a rate of 5°C/min. For electrical measurements an array of 0.5x0.5 mm with a spacing of 0.5 mm of 200 nm thickness Cr/Au contacts were deposited on the sample surface by d.c. sputtering at room temperature (Figure 5.2.20).

The perpendicular conductivity was measured by a.c. impedance spectroscopy at the room temperature with frequencies ranging from 1 to 10^7 Hz (see the experimental setup in Figure 4.2.5.2). For electrical measurements soft micro-tips were used and the force applied on the Au-contacts on top of the samples surface was chosen in order to not penetrate the thin films. All the measurements were performed in air.

Figure 5.2.21 shows the measured impedance spectrum for CaF_2 thin films grown on both (111) oriented n^+*-type* and p^+*-type* Si.

For the CaF_2 samples deposited on (111) p^+*-type* Si substrate a full semicircle is obtained, without any evidence of the blocking electrode or contribution from the interface CaF_2/Si. To analyze the data only a simple RC-parallel model was used, due to the fact that the resistance of the Si substrate is very small and can be neglected:

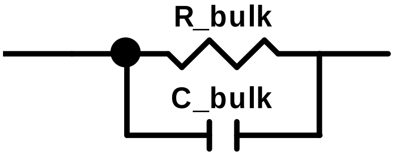

From the values of resistance and capacitance obtained, the perpendicular conductivity and dielectric constant were calculated. The relative dielectric constant was found to be ε=8.7 which is in a good agreement with literature data of 7.4 (at 1 KHz). The perpendicular conductivity was $4x10^{-11}$ $\Omega^{-1}cm^{-1}$ and is in same range with extrapolated data to the room temperature, from the single crystal measurements.

For the samples on n^+*-type* Si an overlapping of two semicircles was found. In order to fit the experimental data a simple model was assumed:

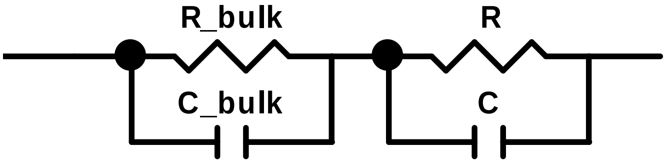

Because the first semicircle (from high frequency range) is on the same order of magnitude as p^+*-type* Si, the first RC circuit refers to the bulk properties of CaF_2 layer and second is assumed to be a contribution due to the interface between the ionic conductor and substrate. The values obtained for resistance and capacitance are similar with the values for p^+*-type* Si. The fitting data for the second semicircle indicate the existence of a boundary zone of a width of around 200 nm.

This is a very interesting result and cannot be explained by now. More detailed investigations are necessary in order to elucidate this behaviour. Owing to these complications we turned to $SrTiO_3$ electrodes.

5.2.2.2. $SrTiO_3$ Substrate

CaF_2/BaF_2 heterolayers were grown on STO:Nb substrates by MBE in a high-vacuum system with a base pressure in the 10^{-10} mbar range and a pressure of $5x10^{-8}$ mbar during deposition [X.X.Guo, I.Matei, Y.G.Guo, J.-S.Lee, J.Maier, in preparation]. Before deposition, all the STO:Nb substrates were optically polished on one side and covered with Cr/Au films on the other side in order to obtain a good electrical contact for the bottom electrode. Single crystals of CaF_2 and BaF_2 were sublimed at 1180° C and 1000° C, respectively.

Heterostructures composed of alternate CaF_2/BaF_2 thin layers were epitaxially grown. For all the samples, BaF_2 was deposited as the first layer because growth on this substrate occurs also exclusively in [111] direction. During growth, the substrate temperature was kept at 500°C, and the growth rate was about 1 nm/min.

All the heterolayers prepared for perpendicular measurements exhibit the same total thickness, however the number of interfaces is varied from sample to sample. Periodicity and thickness were varied over a wide range (the individual layer thicknesses ranging from 100 nm to 5.5 nm) by computer-controlled effusion cell shutters.

After growth, the films were cooled down to room temperature at a rate of 10°C/min. For electrical measurements microelectrodes of Cr/Au of 0.1 mm diameter with a spacing of 0.5 mm and 200 nm thickness were deposited on the sample surface in order to have the top electrodes. For the back electrode, the bottom side of the sample was covered by Cr/Au and then attached to a metal plate by a conducting Ag paste as shown in Figure 4.2.5.2.

The measurements performed in the perpendicular direction yield the impedance spectra as displayed in Figure 5.2.22. Using the equivalent circuit shown in the figure for fitting the experimental data, the resistance of the heterolayer is obtained and converted to the perpendicular conductivity ($\sigma_{\mathrm{m}}^{\perp}$). In this model the resistance of the substrate (R_S) was too small compared to the total resistance of the heterolayers, and therefore was neglected.

The high frequency semicircle refers to the contributions of the heterolayers and the low frequency part represents the blocking electrode (in this case the STO:Nb substrate which is blocking for fluorine ions).

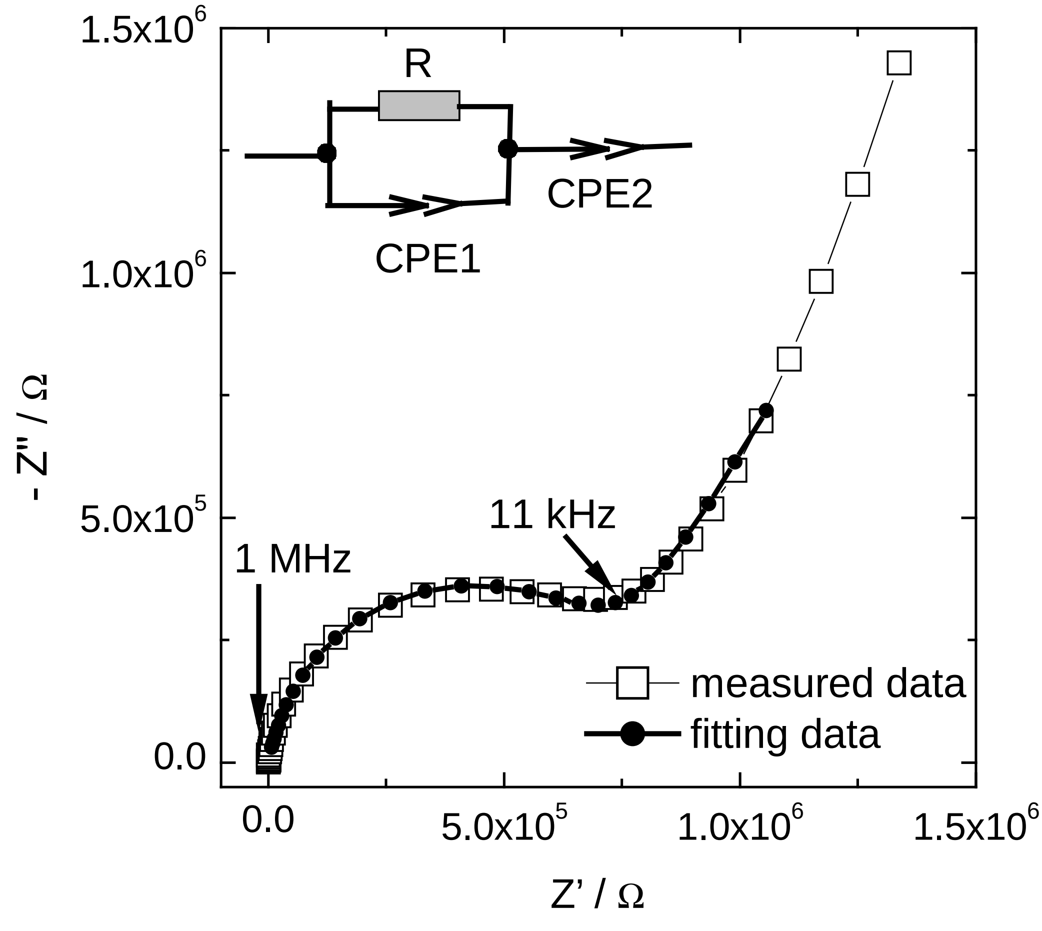

Figure 5.2.22. The typical impedance spectrum for the heterolayer and the model used for fitting the perpendicular experimental data (after X.X.Guo et al.).

The resulting Arrhenius plots (see Figure 5.2.23) for the heterolayers with different spacings (ℓ) reveal different regimes (after X.X.Guo et al.). For moderate spacings $\sigma_{\mathrm{m}}^{\perp}$ only slightly increases with ℓ^{-1} as blocking bulk contributions determine the overall value and the interfacial effects are too small to have a major influence. Taking into account the value of the activation energy of the carriers, (calculated from the slope of the curve in Arrhenius plot) we assume that in this regime the main contribution to the resistance of the samples is given by the bulk parts of CaF_2 (experimental obtained value of 1.1eV compared to the data of the thick CaF_2 films). It seems to be a realistic assumption due to the fact that $\mathrm{F}_{\mathrm{i,CaF_2}}^{'}$ represent minority carriers and the mobility is smaller than in BaF_2. In this regime: $\sigma_{\mathrm{m}}^{\perp} << \sigma_{\mathrm{m}}^{\mathrm{II}}$.

Again, for extremely small spacings, the activation energy of 0.92eV clearly indicate that the interstitial fluorine in CaF_2 play the main role in resistance of the heterolayers. This can be explained if we assume a frozen-in diffusion of the impurity as will be shown in Chapter 6.

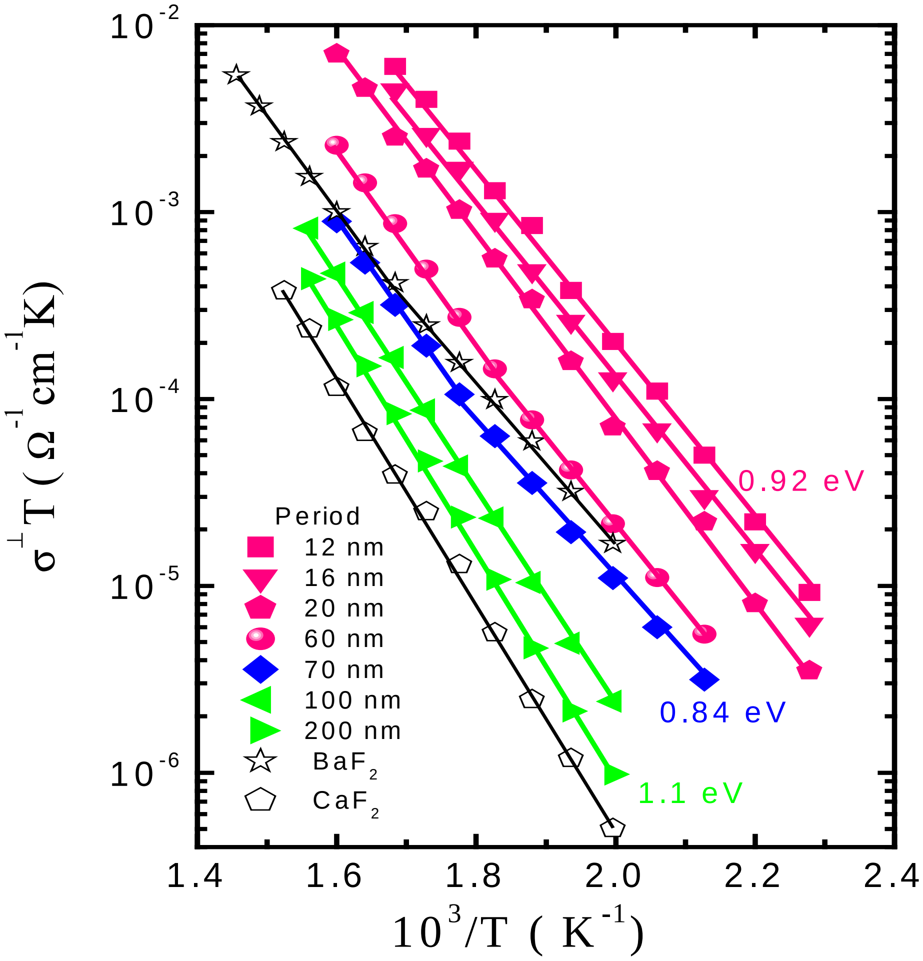

Figure 5.2.23. Arrhenius plot of the heterostructures with different spacings measured in perpendicular direction to the interfaces (after X.X.Guo et al.).

For moderate interfacial spacings the obtained activation energy of 0.84eV cannot indicate which carrier is responsible for the resistance. It can be a mixture of the contributions from carriers from both materials.

These results clearly refer to the semi-infinite and the overlap situations as discussed for the lateral conductivities. Furthermore, a space charge thickness of 10 nm extracted from the first regime is consistent with previous studies.

In short, CaF_2/BaF_2 heterolayers have been epitaxially grown on the conductive single-crystal STO:Nb substrates, which enables us to carry out the conductivity measurement in the perpendicular direction to the interfaces. The obtained partial results are consistent with our previous interpretations for the lateral counterpart. This provides an important independent support as here, in compare to the lateral measurements, the most resistive parts of the profile are provided.

Chapter 6

Numerical Modelling of the Mesoscopic Behaviour

Using the space charge model based on Gouy-Chapman profiles, the characteristics of the linear dependence for large interfacial spacings are in agreement with the experimental data [2000Sata], [2002Sata]. However, this is different for the films of very small spacings, that has been investigated in Ref. [2000Sata]: the anomalous steep increase of conductivity, and the abrupt transition between two limits call for a refinement of the defect chemistry at the CaF_2/BaF_2 interfaces. Note that indications for an upwards bending are also seen in non-annealed samples in this work at low temperature (see Figure 5.2.16), possibly due to a diminished spacing of dislocations network and interfaces.

In this study, the thickness dependence of the layer conductivities is numerically calculated using both the Gouy-Chapman, and the Mott-Schottky modes and the numerical result are compared with experimental data from studies which have been done on this ionic system [2000Sata],[2002Sata],[2004Guo1],[2004Guo2]. In direct comparison to the experimental data, we find that the Mott-Schottky mode can indeed reproduce the quantitative features of the experiments.

The calculation of the defect concentration profiles implies the knowledge of the electrical potential profile, and additionally the relationship between concentration and electrical potential being given by Poisson’s equation (Eq. 2.10) (see also Ref. [2006Jam]).

6.1. Gouy-Chapman Profile

As presented in Chapter 2, according to the space charge profile from Figure 2.2b and from experimental evidence we can assume that $F_i^{'}$ and $V_F^{\bullet}$ carriers should be enriched in the space charge zones of CaF_2 and BaF_2 respectively (Figure 2.6).

With this assumption, the total conductivity parallel to the interface can be written as follow:

$$\sigma_m^{||} \cong \frac{\sigma_m^{BaF_2}}{2} + \frac{\sigma_m^{CaF_2}}{2} + \frac{1}{\ell}\cdot\frac{n-1}{n}\cdot\left[u_v^{BaF_2}\sqrt{2\varepsilon^{BaF_2}\varepsilon_0 k_B T c_{v,0}^{BaF_2}} + u_i^{CaF_2}\sqrt{2\varepsilon^{CaF_2}\varepsilon_0 k_B T c_{i,0}^{CaF_2}}\right] \tag{6.1}$$

where: *u*: mobility of the respective fluoride defect in the indicated phase, $\varepsilon\varepsilon_0$: dielectric constant, V_m: molar value, the superscripts CaF_2 (or BaF_2) refer to the defect enriched in CaF_2 (or BaF_2), *n*: number of layers).

If we assume a maximum interfacial effect (all possible sites at the interface are occupied by defects, with the maximum majority carrier concentrations in both materials: $c_0^{BaF_2} = 1/V_m^{BaF_2}$ and $c_0^{CaF_2} = 1/V_m^{CaF_2}$) in a simple continuum model, we obtain the equation:

$$\sigma_m^{||} = \frac{\sigma_m^{BaF_2}}{2} + \frac{\sigma_m^{CaF_2}}{2} + \frac{1}{\ell}\cdot\frac{n-1}{n}\cdot\left[u_v^{BaF_2}\sqrt{\frac{2\varepsilon^{BaF_2}\varepsilon_0 k_B T}{V_m^{BaF_2}}} + u_i^{CaF_2}\sqrt{\frac{2\varepsilon^{CaF_2}\varepsilon_0 k_B T}{V_m^{CaF_2}}}\right] \tag{6.2}$$

In the calculations, the thermodynamic and defect chemical data from Barsis and Taylor's publications [1968Bars1] ans [1968Bars2] are used for BaF_2 and those from Bollmann for CaF_2 [1973Boll1]. Figure 6.1 shows the calculated results based on the Gouy-Chapman model and experimental results from Ref. [2000Sata].

The dotted line refers to the calculation from Eq. (6.2), which can fit the experimental data for large interfacial spacings ($\ell > 50nm$). For small spacings ($\ell < 30nm$), the conductivity follows the relationship described in Eq. (2.30). In other words, the conductivity is increased by the g_{GC} factor given by Eq. (2.31) compared with respect to the non-overlap situation at 4λ, as the solid line shown in Figure 6.1.

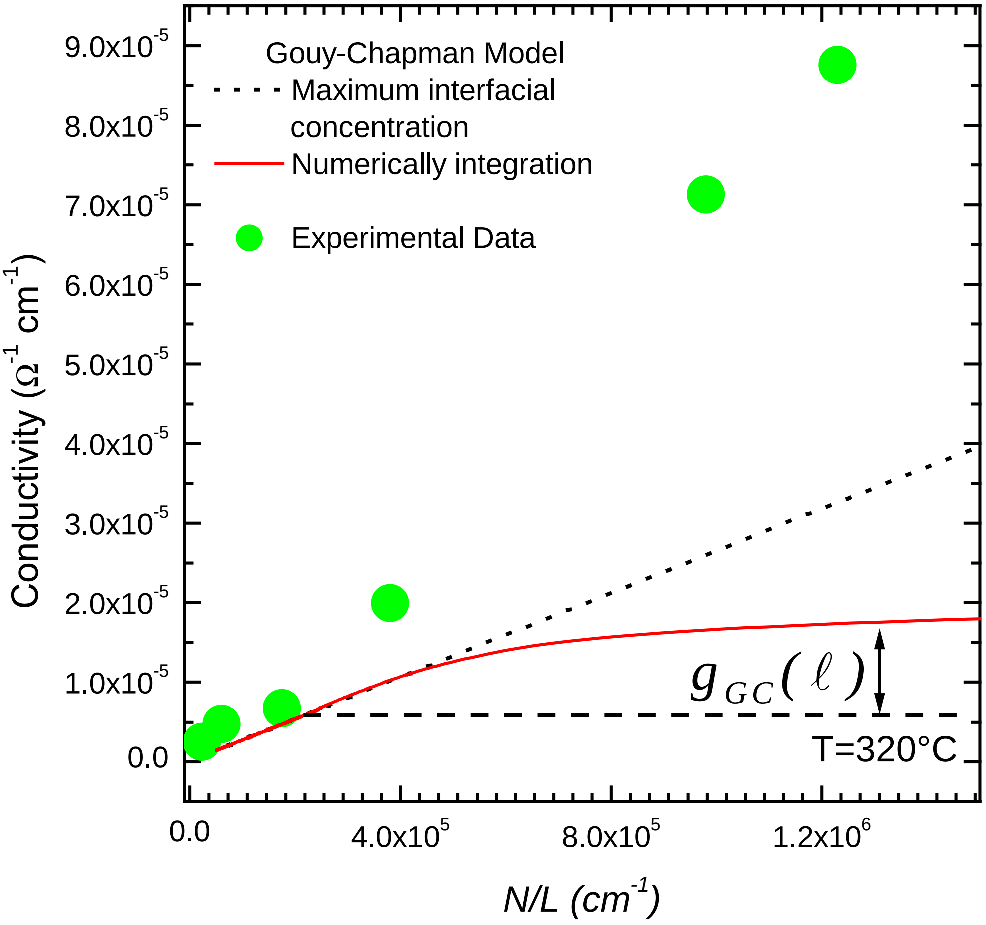

Figure 6.1. Effective lateral conductivity in the case of Gouy-Chapman space charge profile as a function of the inverse spacing between the interfaces. The dotted line refers to calculation of the conductivity for maximum interfacial concentration, and red line refers to the numerically integration of concentration profile, green points represents the experimental results from Ref. [2000Sata].

It can be clearly seen that the Gouy-Chapman model can not describe the steep increase of the conductivities for small spacings and the features of the abrupt transition.

6.2. Mott-Schottky Model

The Mott-Schottky model describes an extrinsic situation when immobile impurities are present in the film and the concentrations of impurities is constant in all thickness range of the layers. (Figure 2.4) In this case the mobile majority carriers are, in the bulk, compensated by impurities. The Mott-Schottky model assumes that the mobile majority defects are depleted at the interface, while the minority are accumulated.

Since the mobile majority carrier is depleted, the Mott-Schottky case usually deals with resistive boundaries. If a minority carrier of the same sign as the impurity, however, has a very high mobility ($^{u_{mi}}\!/_{u_{ma}}$ ratio should be very high), it can be conceived that its accumulation leads to a increase in conductance, even though the impurity level is not exceeded.

Let consider a single charged impurity ($z_{imp}=1$) with a constant concentration and calculate concentration profile in the layers. This assumption is realistic based on the fact that induced coupled plasma (ICP) measurements of the evaporated materials indicated in BaF_2 a single-positive charged impurity (B-boron) in concentration of about 10^{18} cm^{-3} in the samples (after X.X.Guo et al.). In fact, treatment of the samples in oxygen always leads to a decrease of conductivities and a shift of the transition knee to the large value of $1/\ell$. In view of this point, the required high mobility ratio of accumulated and depleted carriers and in view of the observed activation energies, we assume the following situation: In BaF_2 layers $F_i^{\prime}$ as majority carriers compensated by positive dopants in the bulk are depleted and $V_F^{\bullet}$ as minority carriers enriched in the space charge zone. This is consistent with a transfer of F^- from BaF_2 to CaF_2 as the mechanism for ion distribution at the interfaces assumed in Ref. [2000Sata]. As a result, the fluoride vacancies ($V_F^{\bullet}$) are accumulated at the interface of BaF_2 and the interstitials ($F_i^{\prime}$) in CaF_2. Since the mobility of $V_F^{\bullet}$ in BaF_2 is one order of magnitude larger than that of $F_i^{\prime}$ in CaF_2 at the current investigated temperature regime (<350 °C), the contribution from CaF_2 layers to the total conductivity can be neglected. Therefore in the following we neglect the contributions from CaF_2 and exclusively refer to BaF_2 for which we adopt a Mott-Schottky model. As a consequence of the charge transfer and the contribution of charge, there will be a significant increase of $F_i^{\prime}$ in CaF_2 while the $V_F^{\bullet}$ carriers are depleted.

Using parameters from Table 1, the electrical potential profile and defect concentration profiles has been calculated with equation (2.23) and (2.24) respectively and plotted in Figure 6.2 and Figure 6.3.

$c_{imp,\infty}$ Impurity concentration in bulk (cm^{-3})	Temperature (°C)	$\lvert\Delta\phi\rvert = \lvert\phi_0 - \phi_\infty\rvert$ Space charge potential difference (mV)	λ Debye length (nm)	λ^* Effective space-charge thickness (nm)
10^{18}	320	548	3.2	21

Table 6.1. Parameters used for calculations in the case of Mott-Schottky model.

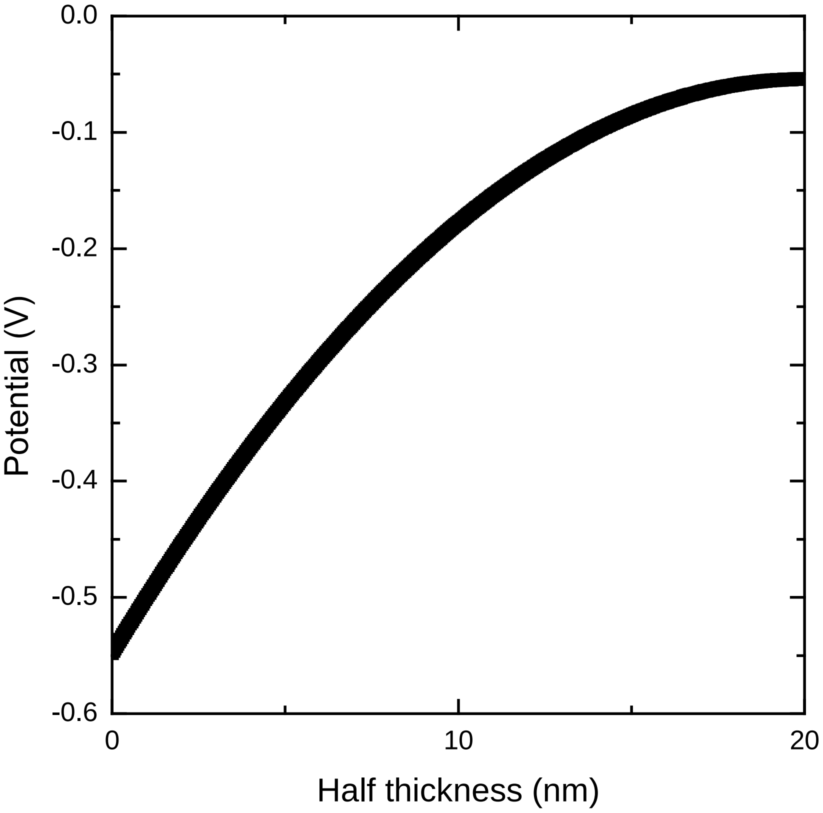

Figure 6.2. Parabolic profile of the potential in Mott-Schottky model.

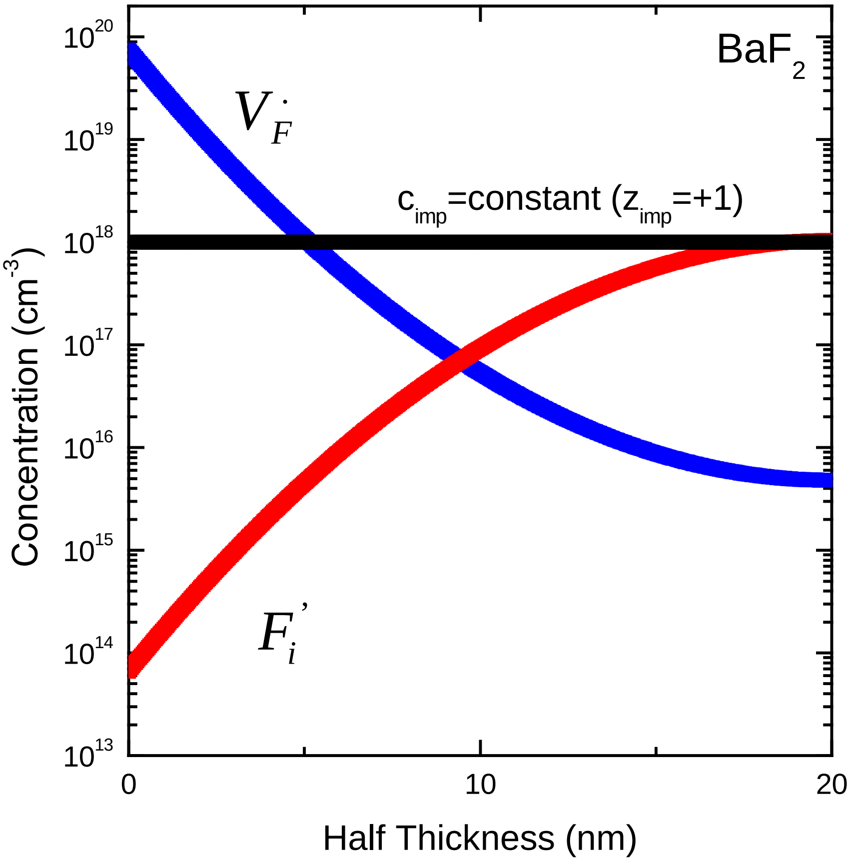

Figure 6.3. The defect concentration profile at the interface between CaF_2/BaF_2 in BaF_2.

The integration of Eq. (2.34) and (2.35) has been done numerically. Figure 6.4 shows the results calculated based on the Mott-Schottky model with the constant impurity profiles. From the figure, it can be seen that now not only the linear part for large spacings but also the behaviour at small spacings can be well fitted. The transition between two regimes occurs at about 40 nm ($\approx 2\lambda^*$). Also the saturation for extremely thin films is in line with the modelling.

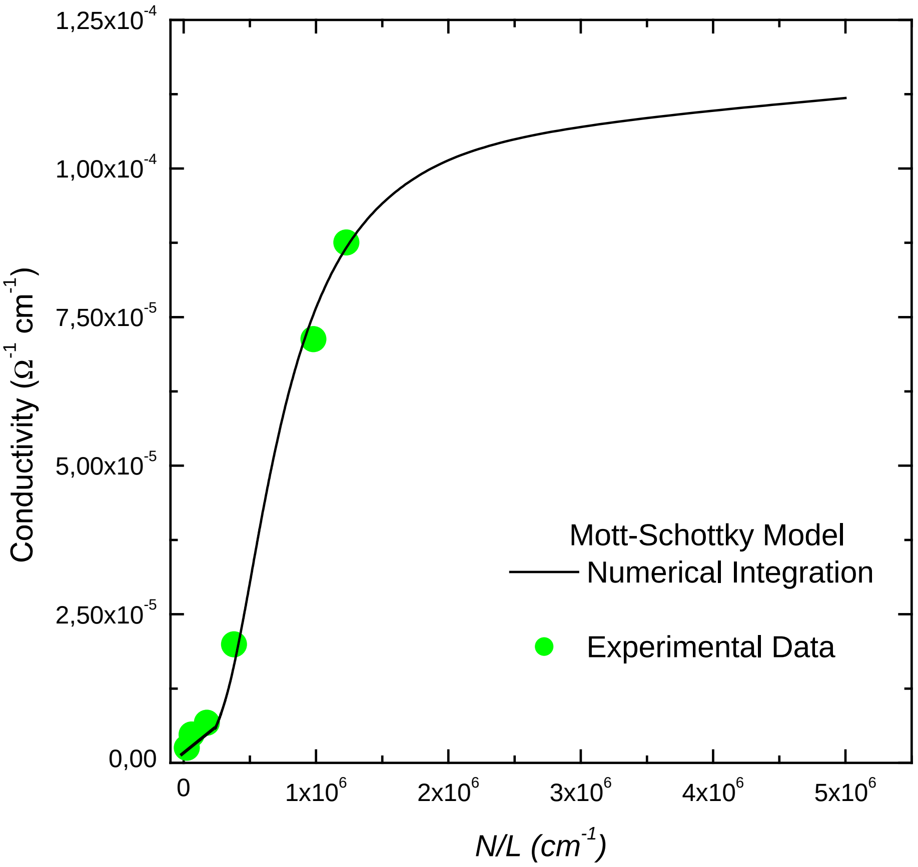

Figure 6.4. Effective conductivity in the case of Mott-Schottky space charge profile as a function of inverse spacing between the interfaces. Space charge potential used in the calculations was 0.548V.

However, the calculated concentration profile turns out to be inconsistent with the charge density of the Mott-Schottky model as the obtained concentration of the minority carrier $V_F^{\bullet}$ exceeds that of the constant impurity level by two orders of magnitude.

The situation is relieved if we assume higher vacancy mobilities. If we assume the mobility to be greater by a factor of 3, which would be well within the accuracy limit, and fit the experimental data, still the profile is inconsistent. Fitting the experimental data with parameters which lead to a concentration of minority carrier $V_F^{\bullet}$ smaller than the constant impurity level results in an increase in the mobility of the carrier at least 2 order of magnitude. This is in disagreement with all literature data and is not a realistic case.

6.3 Frozen-in Impurity Diffusion Profiles

6.3.1. Exponential Profile of the Impurity

In the following we assume more realistic that the impurity content is not constant in the layer, but decreases exponentially from a higher value at the interface until reach the bulk value.

$$c_{imp} = c_{imp,0} \exp\left(-\frac{x}{b}\right) \tag{6.3}$$

b denotes the distance from the interface when the impurity concentration is equal with the bulk value..

$$b = \lambda_D \left[\frac{z_{imp} q}{k_B T} (\Phi_\infty - \Phi_0) \frac{2}{e-2} \right]^{1/2}$$

Following the same method discussed in Mott-Schottky case we can calculate the profile of the space charge potential and the defect concentration profile.

From Poisson's equation (2.18) and with boundary conditions: $\Phi(b) = \Phi_\infty$ and $\Phi'(b) = 0$ the space charge potential is calculated as:

$$\Phi(x) = -\frac{z_{imp} q c_{imp,0} b^2}{\varepsilon} \exp\left(-\frac{x}{b}\right) - \frac{z_{imp} q c_{imp,0} b}{\varepsilon e} x + \frac{2 z_{imp} q c_{imp,0} b^2}{\varepsilon e} + \Phi_\infty \tag{6.4}$$

$c_{imp,0}$ Impurity concentration at interface (cm^{-3})	$c_{imp,\infty}$ Impurity concentration in bulk (cm^{-3})	Temperature (°C)	$\mid \Delta\phi \mid = \mid \phi_0 - \phi_\infty \mid$ Space charge potential difference (mV)	λ Debye length (nm)	b (nm)
$3 x 10^{18}$	$1.1 x 10^{18}$	320	620	3.1	17.8

Table 6.2. Parameters used for calculations in the case of exponential decrease of impurity model.

Using Eq. (6.4) and Eq. (2.7) and initial parameters form Table 6.2, the defect concentration profiles has been computed. The results are displayed in Figure 6.5.

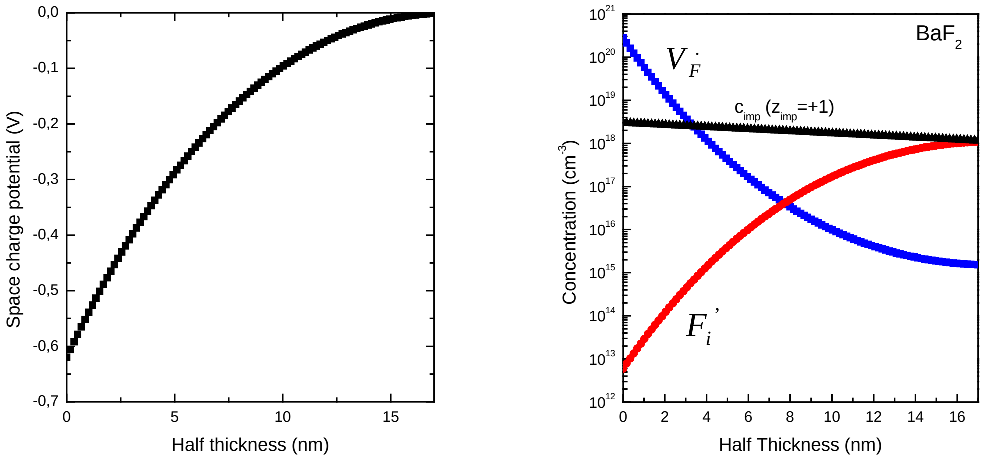

a) b)

Figure 6.5. a) The space charge potential and b) the defect concentration profiles in case of exponential form of the impurity concentration.

The computation accordind to Eq. (2.34) and (2.35) has been done numerically. Figure 6.6 shows the results calculated based on this model with increasing level of the impurity near the interface. With parameters from Table 6.2 the behaviour of the experimental data can again be perfectly fitted.

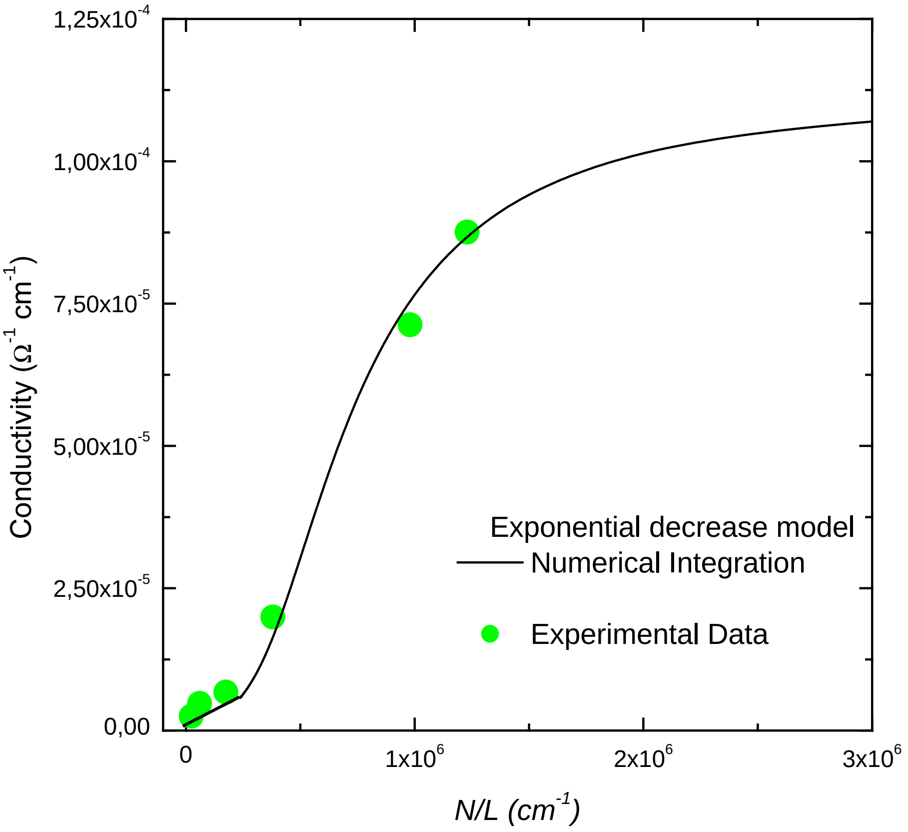

Figure 6.6. Effective conductivity in the case of exponential decrease of the impurities as a function of inverse spacing between the interfaces. Space charge potential used in the calculations was 0.62V.

However, the calculated concentration profile is again inconsistent with the charge density of impurities. The obtained concentration of the minority carrier $V_F^{\bullet}$ exceeds that of the constant impurity level with two orders of magnitude. Exponential profile leads to a very small screening length.

This disagreement is practically removed if we take into account a more real situation in the samples. To remove this discrepancy we assume that the immobile impurity may not be constant in the layers, but increased near to the interface.

6.3.2. Linear Profiles of the Impurities

As a prime trial we assume a linear decrease of the impurity concentration [2007Guo]:

$$c_{imp}(x) = -ax + c_{imp,0} \qquad \text{for } 0 \le x \le \frac{c_{imp,0} - c_{imp,\infty}}{a} \tag{6.5}$$

and:

$$c(x) = c_{imp,\infty} \qquad \text{for } x \ge \frac{c_{imp,0} - c_{imp,\infty}}{a}\,. \tag{6.6}$$

This profile is shown by the solid line in Figure 6.7b (Note that the logarithm of concentration, and also the concentration profile in case of constant impurity level is plotted in Figure 6.7a, for comparison). Starting from Eq. (2.18), the potential $\phi(x)$ is obtained, with the help of which we then numerically calculate the carrier concentrations and conductivities using the same method as discussed above.

With this composite impurity profiles, the experimental data for small spacings can also be perfectly fitted, as shown in Figure 6.8. The corresponding fitting parameters are shown in Table 6.3.

If we vary literature mobilities (from Ref. [1968Bars1] and [1968Bars2]) only by a factor of 3 far-reaching agreement is achieved and no inconsistency occurs. If we assume the mobility a factor of 5 greater, the $V_F^{\bullet}$ concentration will be completely below the impurity level (as shown in Figure 6.7b).

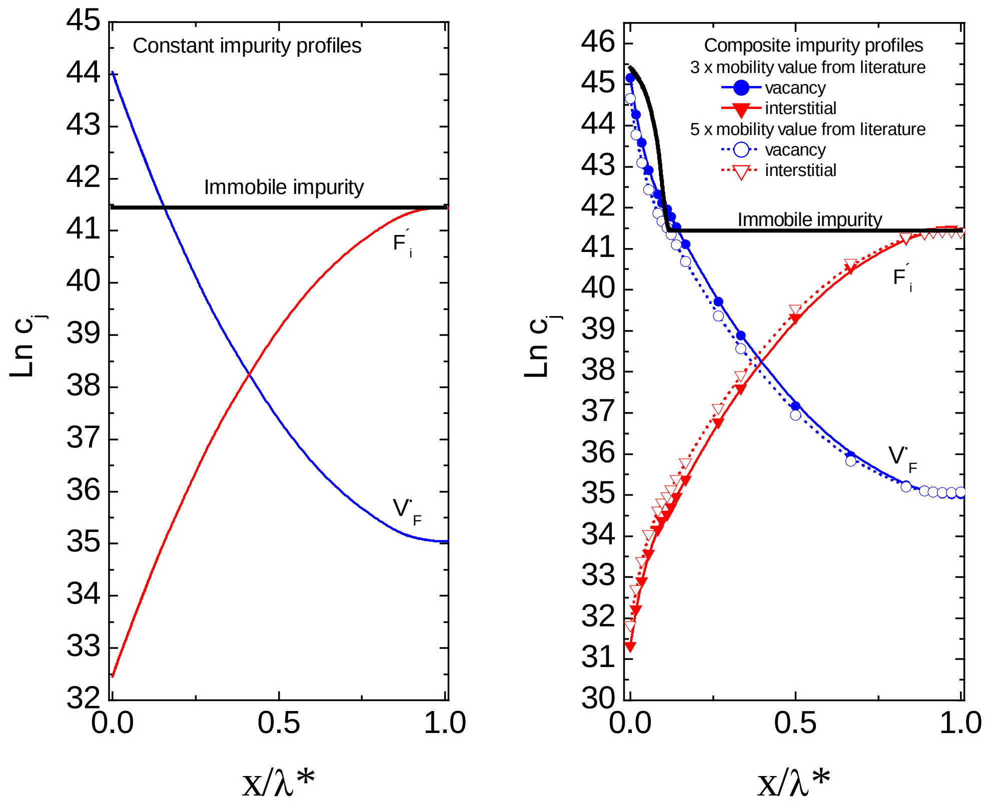

a) b)

Figure 6.7. Defect chemistry of the heterolayers yielded by fitting to the experimental data based on the Mott-Schottky model with (a) the constant impurity profiles and (b) the composite impurity profiles [2007Guo]. In (a) the vacancy mobility is assumed to be a factor of 3 greater than the value from Ref. [1968Bars1] and [1968Bars2], while (b) shows the results with the vacancy mobility increased by a factor of both 3 and 5.

Mobility of $V_F^\bullet$ in BaF_2 (cm^2/Vs)	$c_{imp,\infty}$ Impurity concentration in bulk (cm^{-3})	λ Debye length (nm)	λ^* Effective space-charge thickness (nm)	$\mid\Delta\phi\mid=\mid\phi_0-\phi_\infty\mid$ Space charge potential difference (mV)	$\frac{c_0-c_\infty}{a}$ Frozen impurity range (nm)
$3xu_{V_F^\bullet}$ 5.7×10^{-5}	10^{18}	3	18	450	1.7

Table 6.3. The parameters used for calculations in the case of frozen-in diffusion model. Mobility values of BaF_2 are taken from Ref. [1968Bars1] and [1968Bars2].

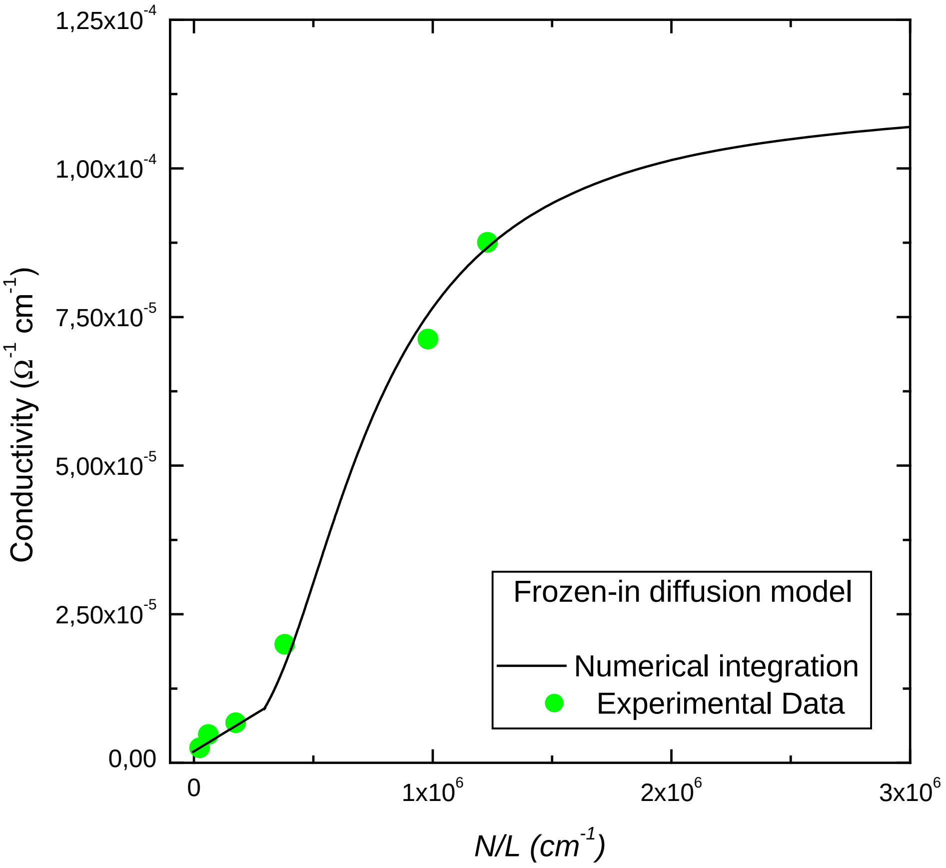

Figure 6.8. Effective conductivity in the case of frozen-in diffusion model as a function of inverse spacing between the interfaces. Space charge potential used in the calculations was 0.45V.

The average difference between the assumed and the corrected charge density is only 20 %. One should point out that the literature data for the vacancy mobility at 320°C are strongly scattered (see data from Ref. [1973Boll2] and [1968Bars1]). There is one order of magnitude difference in the data of Barsis and Taylor's [1968Bars1] compared with Bollmann's [1973Boll2]. Even though the latter values would be even more unfavourable, the assumed flexibility is well in the realistic range.

Obviously, the Mott-Schottky model allows for a realistic interpretation of the mesoscopic behaviour.

In short, the Mott-Schottky model can reproduce the quantitative features of the experimental data (from [2000Sata]) even at very small thicknesses (as long as the films are still intact). The best agreement with defect chemical data from the literature is obtained using a modified Mott-Schottky model in which an impurity profile is assumed not to be horizontal throughout but to exhibit a distinct gradient close to the interface. Such a distribution is realistically expected in view of the sample preparation as well as of the conditioning prior to the measurements (annealing at elevated temperatures).

Chapter 7

Summary

The purpose of this work was to obtain more fundamental insight into ionic processes in CaF_2/BaF_2 heterolayers: the understanding of the mesoscopic situation (i.e. for film thicknesses thinner than 50 nm, both in parallel and in perpendicular direction to the interfaces); the structural investigation of the interfacial and individual layer morphologies; to understand annealing effects, in particular, the anomalous increase in the resistance of the sample (or decrease of the parallel conductivity of the sample) as the annealing temperature increase. Also the fluorite-type crystals CaF_2 and BaF_2 were analyzed and the effective level of impurities was measured. As the later is difficult to obtain otherwise, this is a natural parameter for fitting the experimental results obtained on thin films.

The major results are the following:

1. In this work the heterostructures composed of alternate CaF_2/BaF_2 thin layers with the different individual thicknesses epitaxially grown by MBE on various substrates (Al_2O_3, Si, Nb-doped $SrTiO_3$) with different orientations were prepared and characterized. Surface characterization shows that the films grow in (111) direction. The films exhibit smooth surfaces indicating high quality heterolayers which allow us to use them as a model for studying defect chemistry and size effects.

2. It is confirmed that the parallel conductivity effects in annealed samples can be explained by fluorine ions F^- transfer from BaF_2 to CaF_2, leading to an excess of interstitials in one phase and an excess of vacancy in the another phase.

3. In addition to that, in non-annealed samples, unstable dislocations appear that are obviously charged by F^- absorption resulting in increasing vacancy concentration. These unstable dislocations exist not only at the interface, but also inside the layers. This effect disappears under thermal treatment when the dislocations can be annealed out.

4. In extremely thin films a conductivity anomaly has been observed that has not been explained so far. It is shown that indeed in Mott-Schottky a model, the abrupt increase in the measured parallel conductivity (if plotted as a function of inverse spacing) can

be explained. In order to achieve consistent defect concentrations, one has to assume that the frozen impurity profile is non-horizontal, rather it corresponds to a frozen-in profile.

5. Such profiles are also consistent with fit results of perpendicular measurements which now emphasis the more resistive parts of the heterolayers.

References

[1971Cho] A. Cho, "Film Deposition by Molecular Beam Techniques", J. Vac. Sci. Tech., **Vol. 8** (1971), S31-S38.

[1975Cho] A. Cho, J. Arthur, "*Molecular Beam Epitaxy*", *Prog. Solid-State Chem.*, **Vol. 10** (1975), 157-192.

[1982Ish] A. Ishizaka, K. Nakagawa and Y. Shiraki, *Collected Papers of MBE-CST-2*, 1982, Tokyo (Japanese Society of Applied Physics, Tokyo 1982), 183.

[1995Ma1] J. Maier, *Prog. Solid State Chem.*, **23** (1995), 171.

[2004NYJ] N.Y.Jin-Phillipp, N.Sata, J.Maier, C.Scheu, K.Hahn, M.Rühle, *Structures of* BaF_2*–*CaF_2 *heterolayers and their influences on ionic conductivity*, Journal Of Chemical Physics, **120** (2004).

[1985Hash] S.Hashimoto, J.-L.Peng,W.M.Gibson, L.J.Scholwalter, R.W.Fathauer, *Strain Measurement of Epitaxial* CaF_2 *on Si (111) by MeV Ion Channeling*, Appl. Phys. Lett., **47** (1985), 1071-1073.

[1985Scho] L.J.Schowalter, R.W.Fathauer, R.P.Goehner, L.G.Turner, R.W.DeBlois, S.Hashimoto, J.-L.Peng, W.M.Gibson, J.P.Krusius, *Epitaxial Growth and Characterization of* CaF_2 *on Si,* J.Appl.Phys, **58** (1985), 302-308.

[1986Scho] L.J.Schowalter, F.A.Ponce, G.Anderson, S.Hashimoto, *Materials Research Society Symp. Proc.*, **67**, J.C.C.Fan and J.M.Poate, Materials Research Society, Pittsburgh, (1986), 125.

[1986Pon] F.A.Ponce, G.B.Anderson, M.A.O'Keefe, L.J.Schowalter, J.Vac.Sci.Tech., **B4** (1986), 1121.

[1986Rieg] D.Rieger, F.J.Himpsel, U.O.Karlson, F.R.McFeely, J.F.Morar, J.A.Yarmoff, Phys. Rev., **B34** (1986), 7259.

[1992Blun] S.Blunier, H.Zogg, C.Maissen, A.N.Tiwari, R.M.Overney, H.Haefke, P.A.Buffat, G.Kostorz, *Lattice and Thermal Misfit Dislocations in Epitaxial* CaF_2*/Si(111) and* BaF_2*-*CaF_2*/Si(111) Structures*, Phys. Rev. Lett., **68** (1992), 3599-3602.

[1993Zogg] H.Zogg, C.Maissen, S.Blunier, S.Teodoropol, R.M.Overney, T.Richmond, H.Haefke, *Strain Relaxation Morphologies of IIa-Fluorides and Lead-Chalcogenide Layers on Si(111)*, Journal of Crystal Growth **127** (1993), 668-671.

[2000Sata] N. Sata, K. Eberman, K. Eberl, J. Maier*, Mesoscopic fast ion conduction in nanometre-scale planar heterostructures*, Nature, **408**, (946-949).

[2002Sata] N. Sata, N.Y. Jin-Phillipp, K. Eberl, J. Maier, *Enhanced ionic conductivity and mesoscopic size effects in heterostructures of* BaF_2 *and* CaF_2, Solid State Ionics **154– 155** (2002), 497– 502

[1968Bars1] E. Barsis, and A. Taylor,*F^- Vacancy Conductivity in* BaF_2 *Crystals,* J. Chem. Phys. **48** (1968), 4357.

[1968Bars2] E. Barsis, and A. Taylor, *Interstitial Conduction in* BaF_2 *Crystals*, J. Chem. Phys. **48** (1968), 4362.

[1973Boll1] W. Bollmann, R. Reimann, *Concentration and Mobility of Interstitial Fluorine Ions in* CaF_2, Phys. Stat. Sol. (a) **16** (1973), 187-196.

[1973Boll2] W. Bollmann, *Ionic conduction Of Pure and Doped* BaF_2 *Crystals*, Phys. Stat. Sol. (a) **18** (1973), 313-321.

[2006Jan] J. Jamnik, *Impact of particle size on conductivity and storage capacity as derived from the core–space charge model*, Solid State Ionics **177** (2006), 2543 – 2547.

[1985Hag] P. Haggenmuller, *Inorganic Solid Fluorides*, Academic Pres Inc., 1985

[1957Ure] R.W.Ure, *Ionic Conductivity of Calcium Fluoride Crystal*, J. Chem. Phys, **26** (1957), 1363.

[1995Saito] Y. Saito, J. Maier, *Ionic Conductivity of the Fluoride Conductor* CaF_2 *by Grain Boundary Activation using Lewis Acids*, J. Electrochem. Soc. **142** (1995), 3078.

[1999Puin] W. Puin, S. Rodewald, R. Ramlau, P. Heitjans, J. Maier, *Local and Overall Ionic Conductivity in Nanocrystalline* CaF_2, Solid State Ionics **131**, (2000), 159-164.

[2004Ma] J. Maier, *Physical Chemistry of Ionic Materials*, *Ions and Electrons in Solid*; John Wiley and Sons, Ltd., 2004.

[1973Hin] J.W.Hinze, J.W.Patterson, J. Electrochem. Soc., **120** (1973), 96

[1978Del] J.Delcet, R.J.Heus, J.J.Egan, J. Electrochem. Soc., **126**, (1978), 755.

[1956Wag] C.Wagner, Z.Electrochem, **60** (1956), 4.

[1957Wag] C.Wagner, Proc. CITCE, **7** (1957), 361.

[1979Red] S.N.S.Reddy, R.A.Rapp, J. Electrochem. Soc., **126** (1979), 2023.

[2000Tuller] H.L.Tuller, Solid State Ionics, **131** (2000), 143.

[1984Ma] J.Maier, Ber. Bunsenges Phys.Chem., **88** (1984), 1057.

[1987Ma1] J.Maier, Solis State Ionics, **23** (1987), 59.

[1987Ma2] J.Maier, L.Electrochem.Soc., **134** (1987), 1524.

[1987Ma3] J.Maier, Materials Chemistry and Physics, **17** (1987), 485

[1985Ma1] J.Maier, Ber. Bunsenges Phys.Chem., **89** (1985), 355.

[1985Ma2] J.Maier, J.Phys.Chem.Solids, **46** (1985), 309.

[1986Ma] J.Maier, Ber. Bunsenges Phys.Chem., **90** (1986), 26.

[2000Ma] J.Maier, Solid State Ionics, **131** (2000), 13-22.

[1996Wil] N.T.Wilson, M.Wilson, P.A.Madden, N.NPyper, *Interionic Interactions and Fast-ionic Conduction in* CaF_2, J.Chem.Phys, **105** (1996), 11209.

[1993Lin] P.J.D.Lindan,M.J.Gillan, J.Phys., **5** (1993), 1019.

[1982Ishi] H.Ishiwara, T.Asano, Appl.Phys.Lett., **40** (1982), 66.

[1982Asa] T.Asano, H.Ishiwara, Thin Solid Films, **93** (1982), 143.

[1999Jam] J.Jamnik, J.Maier, *Defect chemistry and chemical transport involving interfaces*, Solid State Ionics **119** (1999), 191–198.

[1981Sze] S.M.Sze, Physics os Semiconductor Devices, Wiley, Ney York (1981).

[2007Ma] J.Maier, Faraday Discuss. **134** (2007), 151.

[1993Schu] E.F.Schubert, Dopping in III-V Semiconductors, Cambridge University Press, 1993.

[1996Fle] J. Fleig and J. Maier, *Local Conductivity Measurements on AgCl Surfaces Using Microelectrodes*, Solid State Ionics, **85** (1996), 9–15.

[2007Guo] X.X.Guo, I.Matei, J.Jamnik, J-.S.Lee, J.Maier, submitted.

[1987Mac] *Impedance Spectroscopy - Emphasizing Solid Materials and Systems*, edited by J. R. Macdonald (John Wiley & Sons, Inc., New York, USA, 1987).

[1969Bau] J. E. Bauerle, *J. Phys. Chem. Solids* **30** (1969), 2657-2670

[2002Fle] J. Fleig, Habilitation Thesis, Ulm, Germany, 2002.

[1941Cole] K. S. Cole and R. H. Cole, *J. Chem. Phys.* **9** (1941), 341-351.

[1990Jam] J. Jamnik, M. Gaberscek, and S. Pejovnik, *Electrochim. Acta* **35** (1990), 423-426.

[2004Guo1] X.X. Guo, J. Maier, *Ionic conductivity of epitactic MBE-grown BaF_2 films*, Surface Science **549** (2004), 211–216.

[2004Guo2] X.X. Guo, N. Sata, J. Maier*, Effects of orientation and substrate on ion transport in fluoride heterostructures grown by molecular beam epitaxy*, Electrochimica Acta **49** (2004), 1091–1096.

Acknowledgements

At this point I would like to thank all those who - directly or indirectly - contributed to the success of this work:

Foremost I would like to express my deepest gratitude to my advisor, Prof. Dr. J. Maier, for his expert advises, continuous support, insight, understanding and valuable guidance throughout my whole PhD study. I thank him for giving me the opportunity to accomplish my PhD in a very stimulating working environment.

I am very grateful to Prof. Dr. Eric J. Mittermeijer and Prof. Dr. Fritz Aldinger for being on my examination committee.

Special thanks to the International Max Planck Research School for Advanced Materials, for providing the funding and support for this study. Dr. Hans-Georg Libuda must be acknowledged for organizing and coordinating not only the IMPRS-AM, but also for his constant assistance with day-to-day problems. Many thanks to all other members of the Research School for enjoyable scientific and non-scientific discussions.

Many thanks to Dr. Xiangxin Guo for the help with the preparation and the measurements of the samples, and the scientific discussions were of great help to my thesis. I thank him for his constant readiness to discuss problems related to this work and for his friendly cooperation.

My special thanks to Dr. Jong-Sook Lee for all her support, advice and very interesting discussions. I deeply appreciate her critical reading of an earlier version of this thesis.

Prof. Dr. Janez Jamnik was always an exceptionally competent and interested contact person for all kinds of scientific conversations. I am grateful for his continuous support.

I would like to acknowledge Dr. Rotraut Merkle and Dr. Jurgen Fleig for being interested in an experimental/theoretical discussion. Within our meetings they have provided many ideas and asked difficult questions that inspired much of the experiments and numerical calculations. It was a great pleasure to work together.

I further thank Gabi Götz for measuring an appreciable number of X-ray diffractograms, Anette Fuchs for taking SEM pictures, Uwe Traub for his friendly help with all computer related problems, Dr. Yu-

Guo Guo for his help in performing the AFM measurements, and Sofia Weiglein for her efficient administrative work. I would also like to thank to Karl Wilhelm Kussmaul for the technical help with all the devices which was vital for the successful completion of this work.

I thank all of my colleagues in the group of Prof. Maier as well as from other departments for the friendly atmosphere at the Max Planck Institute for Solid State Research and for all the inspiring discussions, their help and wonderful company they provided during the last five years.

My stay in Stuttgart would not have been half as pleasant and productive if it weren’t for the wonderful friends which I have made. They have been a constant support and a source of good time.

Last but not least, I thank my wife Dani for her loving support and understanding whenever this work absorbed a substantial amount of my time and energy, as well as my entire family. I dedicate this PhD. thesis to them.

Curriculum vitae

Name: **ION MATEI**
Nationality: Romanian
Date of Birth: January 28th, 1971
Place of Birth: Domneşti, ROMANIA
Marital Status: Married

EDUCATION

Since 2002	PhD in IMPRS-AM and Max Planck Institut for Solid State Reasearch, Stuttgart "*Electrochemical studies of MBE-grown* CaF_2/BaF_2 *heterolayers*" with Prof. Dr. Joachim Maier.
In 2001	I was promoted by competition as a 3rd Degree Principal Researcher.
1998-2001	I was promoted by competition and worked as a Scientific Researcher.
1995-1998	I worked at the National Institute of Materials Physics (NIMP) as Junior Researcher, in the field of superconductor and ferroelectric materials.
1995-1996	Master of Science in Physics at Faculty of Physics, University of Bucharest, ROMANIA.
1990-1995	Licentiate Degree Diploma in Physics at Faculty of Physics, University of Bucharest, ROMANIA.
1989-1990	Military service
1985-1989	High School: "Liceul de Matematica-Fizica Nr.1", Pitesti, Romania.
1977-1985	Elementary and Secondary School, Domnesti, Romania